



UNIVERSITÀ DEGLI STUDI DI TRIESTE

**XXXI CICLO DEL DOTTORATO DI RICERCA IN
NANOTECNOLOGIE**

**Biomedical applications of
Surface Enhanced Raman Spectroscopy:
a step forward to clinical practice**

Settore scientifico-disciplinare: chim/07

**DOTTORANDA
ELISA GURIAN**

**COORDINATORE
PROF. LUCIA PASQUATO**

**SUPERVISORE DI TESI
PROF. VALTER SERGO**

**TUTORE
PROF. ALOIS BONIFACIO**

ANNO ACCADEMICO 2017/2018

*The real voyage of discovery
consists not in seeking new landscapes,
but in having new eyes.
(M. Proust)*

Table of Contents

Abstract	IV
Riassunto	VI
1 Introduction	1
1.1 Background and rationale	1
1.2 Object of the research.....	4
2 Raman Spectroscopy and SERS	6
2.1 Raman Spectroscopy.....	6
2.1.1 Molecular vibrations	7
2.1.2 Raman scattering: background principles.....	8
2.1.3 Raman scattering.....	11
2.2 Surface Enhanced Raman Spectroscopy	14
2.2.1 The electromagnetic model of SERS	16
2.2.2 SERS: geometry and aggregation effects	17
2.2.3 SERS substrates.....	18
2.2.4 SERS and the label-free approach for biosensing.....	21
3 Multivariate Data Analysis	23
3.1 A primer on machine learning	23
3.2 Data analysis workflow.....	24
3.3 Principal Component Analysis	25
3.4 Linear Discriminant Analysis	27
4 Adsorption models	29
4.1 The adsorption process	29
5. SERS substrates	34
5.1 Background	34
5.2 Materials and Protocols.....	36
5.2.1 Citrate-reduced silver nanoparticles:.....	36
5.2.2 Protocol #1: paper-based Ag-solid substrates.....	36
5.2.3 Protocol #2: paper-based Ag-solid substrates.....	37
5.3 Substrates characterization	38
5.3.1 SERS characterization.....	40

5.3.2	The internal standard approach	42
6	SERS spectra of blood fractions	45
6.1	Background.....	45
6.2	Materials and Methods.....	47
6.2.1	SERS substrate fabrication.....	47
6.2.2	SERS instrumentation.....	47
6.2.3	Sample collection.....	48
6.2.4	Sample preparation.....	48
6.2.5	Spectra collection.....	48
6.2.6	Data analysis.....	50
6.3	Results and Discussion.....	50
6.3.1	SERS and Raman of whole blood and blood constituents.....	50
6.3.2	SERS of biofluids: effect of the colloid/biofluid volumetric ratio	55
6.3.3	Effect of filtration and lysis on SERS of biofluids.....	57
6.4	Highlights:	60
7	The Nanostructure-Biofluid interface: a model.....	61
7.1	Background.....	61
7.2	Materials and Methods.....	63
7.2.1	SERS substrate fabrication.....	63
7.2.2	SERS instrumentation.....	63
7.2.3	Sample preparation and spectra collection.....	63
7.2.4	Data analysis.....	65
7.3	Results and Discussion.....	65
7.3.1	Adsorption curves	65
7.3.2	The role of protein filtration.....	75
7.3.3	The metabolites permeation through the protein corona	76
7.4	Highlights:	78
8	SERS and Diagnosis.....	79
8.1	Background.....	79
8.1.1	Role of the preanalytical steps.....	80
8.1.2	Breast Cancer.....	81
8.1.3	Liver disorders.....	82
8.2	Materials and Methods.....	84

8.2.1	SERS substrate fabrication	85
8.2.2	SERS instrumentation.....	85
8.2.3	Data analysis.....	85
8.3	Detailed methods, Results and Discussion.....	86
8.3.1	Breast Cancer diagnosis.....	86
8.3.2	NAFLD progression and diagnosis.....	91
8.3.3	From cirrhosis to Hepatocellular Carcinoma	95
8.4	Highlights:.....	100
9	Conclusions.....	101
	Acknowledgements.....	103
	Appendix 1	104
	Appendix 2	105
	Appendix 3	107
	Appendix 4	109
	Appendix 5	110
	References.....	111

Abstract

This PhD project aims to apply nanostructured metal surfaces as substrates for Surface Enhanced Raman Spectroscopy for the study of biofluids. This analytical technique provides the vibrational fingerprint of a sample assisted by nanostructured metal surfaces, which can enhance the scattering signal of analytes adsorbed on them: this allows detection of analytes in very low concentrations. These features tell a lot about the potential of SERS in the bioanalytics, and indeed, in this field, the use of SERS has increased over the past decade taking advantage of both sensitive detection and fingerprinting features.

Above all, SERS requires the manufacturing of metal nanostructured substrates as sensors. In particular, this project is based on the development of a label-free approach: no functionalization is present on the nanoparticles surface, and, hence, no preferential affinity for a given analyte in the biological matrix is sought. Briefly, once nanoparticles are in contact with the specimen, the analytes may adsorb on them without any specific interaction other than their affinity for the metal. The outgoing SERS signal will be a snapshot of what actually reached the metal surface, namely a fingerprint of the sample. For instance, the label-free analysis of biofluids reflects the metabolic content of the fluid itself. In the “omic” era, SERS can integrate with untargeted metabolomics, provides the metabolic profile of a specimen and distinguishes different samples accordingly, based on differences in such profiles. Electrostatically stabilized silver colloids have been chosen, given that their performances with biofluids are known. They have been used both as colloidal suspension in water, and fixed on a paper support, according to an in-house developed protocol for the fabrication of solid substrates. The coupling of metal nanostructured substrates with SERS acts as actual sensors, able to interact with aqueous environment and detect dissolved analytes. The real advantage of the paper supports lies in the stability of the spectroscopic response: they are long lasting, easy to fabricate and to handle, cost and time-effective, prone to scale up. These reasons make them potential Point of Care tools in the frame of SERS applications.

Building on the expertise our research group has been developing in recent years, the aim of this PhD thesis is twofold: to push forward our fundamental knowledge of the nanostructure-biofluid interaction and to test the feasibility of the application of SERS for specific clinical problems. These goals were pursued in three steps:

1. to develop protocols for the *label-free* analysis of blood fractions (serum, plasma, erythrocytes, peripheral blood mononuclear cells, and whole blood) with SERS, exploiting their features according to several treatments and SERS substrates;
2. to characterize the behavior of biomolecules at the interface with metal nanoparticles on model systems, namely to understand the role of the protein and non-protein corona in the metabolites-nanoparticle interaction. The model system is based on mixture of human serum albumin (i.e. the most abundant serum protein)

and molecules which are commonly detected in SERS of biofluids: adenine, hypoxanthine and uric acid;

3. to apply the aforementioned knowledge to the early diagnosis of several diseases (breast cancer, non-alcoholic fatty liver diseases, cirrhosis and hepatocellular carcinoma) through serum and plasma samples by means of multivariate data analysis of SERS spectra.

Considering the latter application of SERS in the field of disease diagnosis, the aim is to provide new diagnostic methods complementary to the accepted gold standards such as immunochemistry and histopathology methods. The advantages of SERS lie in the rapid response and on the non-invasiveness of the liquid biopsy approach. As a future goal, the development of SERS platforms as label-free point of care tools integrated to portable Raman instruments could bring the diagnosis procedures from the bench to the bedside.

SERS revealed to be a powerful tool in the biomedical field for the liquid biopsy analysis, and many issues still need to be tackled. In conclusion, SERS and the label-free approach can potentially support the routine diagnostic pathway and, hence, fulfill unmet clinical needs.

Riassunto

Lo scopo di questo progetto di dottorato è quello di utilizzare delle superfici metalliche nanostrutturate come substrati per la spettroscopia Raman amplificata da superfici (SERS) per l'analisi di biofluidi. Questa tecnica analitica restituisce l'impronta digitale vibrazionale del campione grazie alla presenza della nanostruttura metallica in grado di amplificare il segnale diffuso inelasticamente dall'analita adsorbito su di essa, anche in concentrazioni molto basse. Queste caratteristiche anticipano le potenzialità della spettroscopia SERS in campo bioanalitico che ha visto un aumento esponenziale delle sue applicazioni nell'ultimo decennio. In particolare, la SERS richiede la fabbricazione di substrati metallici nanostrutturati che possano funzionare da sensori. Questo progetto si basa sullo sviluppo di un approccio privo di marcatura (label-free): nessuna funzionalizzazione è presente sulla superficie metallica al fine di rilevare in modo aspecifico gli analiti presenti della matrice di interesse biologico. Il risultato del segnale SERS sarà un'istantanea della soluzione in analisi depositata sulla superficie metallica, cioè l'impronta specifica del campione. Per esempio, l'analisi label-free dei biofluidi riflette il suo contenuto metabolico. Nell'era "omica", il SERS può essere integrato nella metabolomica non funzionalizzata in quanto fornisce il profilo metabolico del soggetto in esame e di conseguenza distinguere campioni diversi basandosi sulle differenze di ogni profilo analizzato. I colloidi stabilizzati elettrostaticamente sono stati scelti per la loro nota compatibilità con i biofluidi. Verranno usati sia in forma colloidale in sospensione acquosa, sia fissati su un supporto di carta, definiti supporti solidi e sviluppati grazie a un protocollo validato nel nostro laboratorio. L'insieme dei substrati nanostrutturati e il SERS possono essere definiti dei sensori veri e propri, capaci di interagire con l'ambiente acquoso e rilevare gli analiti disciolti in esso. Il vantaggio portato dai supporti in carta risiede nella stabilità della risposta spettroscopica: sono di lunga durata, facili da fabbricare e da maneggiare, economici e veloci, potenzialmente fabbricabili su ampia scala. Queste sono le caratteristiche che nell'ambito delle applicazioni del SERS possono promuovere la costruzione di un dispositivo Point of Care. Basandosi sulle competenze acquisite dal nostro gruppo di ricerca, lo scopo di questa tesi di dottorato è duplice: aumentare le nostre conoscenze sull'interazione biofluidi-nanostrutture e utilizzare il metodo SERS per lo studio di specifici problemi clinici. Al fine di soddisfare tali richieste questo lavoro è diviso in tre parti:

1. Sviluppare protocolli per l'analisi label-free delle frazioni di sangue (siero, plasma, eritrociti, cellule mononucleate del sangue periferico, e sangue intero) con il SERS, sfruttando le loro caratteristiche in base alla diversa preparazione dei campioni e ai substrati SERS utilizzati;
2. Caratterizzare il comportamento delle biomolecole sulla superficie di nanoparticelle metalliche su sistemi modello, cioè capire il ruolo delle corone di

proteine e non proteine nell'interazione metabolita-nanoparticelle. Il sistema modello usato si basa su un insieme di albumina di siero umano (la più abbondante proteina del siero) e molecole che sono comunemente osservate nei biofluidi: adenina, ipoxantina e acido urico;

3. Applicare le nozioni di cui sopra per la diagnosi precoce di diverse malattie (tumore al seno, fegato grasso non alcolico, cirrosi e carcinoma epatocellulare) tramite campioni di sangue e plasma e l'uso di analisi dati multivariata per spettri SERS.

Lo scopo dell'utilizzo del SERS in ambito medico è di proporre nuovi approcci diagnostici complementari alle tecniche già in uso in clinica come ad esempio i metodi di immunochimica e istopatologia. Il vantaggio del SERS risiede nella rapida risposta e in un approccio non invasivo tramite l'utilizzo di biopsia liquida. Lo scopo futuro è lo sviluppo di una piattaforma SERS label-free come dispositivo point of care integrato allo strumento Raman che renderebbe le procedure di diagnosi molto più veloce dal laboratorio al letto del paziente.

Seppure il SERS abbia già dimostrato di essere un metodo valido in campo biomedico per l'analisi di biopsie liquide, molto deve esser ancora scoperto. In conclusione, il SERS e l'approccio label-free possono potenzialmente essere un grande supporto per la diagnostica ad oggi in uso andando ad ottemperare quelle richieste cliniche non ancora soddisfatte.

1 Introduction

1.1 Background and rationale

In healthcare, the actual issue that the scientific community is called to implement is personalized medicine and to cope with the need of improved diagnostic and prognostic tools.

The first step is to understand which are the clinical needs and how to meet them and to fulfill their criteria, such as to improve the diagnostic accuracy, to reduce invasiveness, to go for cost-effective devices that are of simple fabrication, use and response rate [1,2]. Obviously, the dialogue between researchers and end-users (medical staffs, but also the patients, stakeholders, and so on) is tremendously important to identify these targets. Nowadays, the research pushes towards the discovery of cutting-edge technologies and protocols that may address these issues in clinical settings. At the same time, the development of lab-on-a-chip systems may help in the miniaturization of companion diagnostics as point-of-care tools (POC), going from the bench to the patient bedside [3–7].

The identification of practical solutions is a true challenge, since it is the very first step for a real application: indeed, the number of commercialized successful devices is really low compared to the scientific efforts [8,9].

To date, several analytical techniques have been applied in clinics and developed for structural and chemical characterization, analytes quantification, biosensing, medical imaging and diagnosis. These benefit from different physical, biological, chemical tools, i.e., solid or liquid state magnetic resonance, chromatography hyphenated to mass spectrometry, a number of fluorescence, infrared, Raman spectroscopy tools, immunoassay tests, and so on [10]. Nevertheless, their practical implementation has been often hampered by several issues: the incompatibility with the biological fluids or tissues, high costs and poor accuracy.

In the recent years, the improvement in electronics, optics and photonics, as well as in the nanofabrication technology, allowed the Surface Enhanced Raman Spectroscopy (SERS) to gain a chance to be used in clinical devices [10–12]. SERS is a spectroscopic technique that provides the molecular (vibrational) fingerprint of a sample with high sensitivity and specificity, able to work with aqueous specimens in low volumes and with reduced or no sample pretreatment. SERS preserves the features of the normal Raman scattering with an enhancement factor up to 10^{10} of the signal, basically down to the single molecule detection. Being versatile, its application ranges from chemistry to biology, environmental science, medicine, pharmacology, and others [13,14].

The SERS response requires the use of nanostructured supports as sensors: the sample constituents need to be in close proximity to the metal surface to experience an amplification of the outgoing signal. To improve sensitivity or to make their use compatible with a broad variety of biological samples, customization of the substrates is possible, like the chemical functionalization for targeted detection of markers or their implementation on microfluidic devices and solid supports [13]. For further details, the reader is addressed to the next chapter or to the dedicated literature and text books [14,15].

The number of publications related to the clinical application of SERS increased exponentially over the last 10 years. Great attention has been given to cancer diagnosis, where the early detection is an urgent task.

Pathological information is currently extracted from imaging of cells and tissues, analysis of biofluids and liquid biopsies where contrast is achieved by adding tailored NPs to trigger the SERS effect. Both qualitative and quantitative detection are pursued.

In general, labeled SERS is commonly the most popular trend, following the old but gold paradigm of specific biomarker detection, thanks to the addition of Raman active moieties and antibodies to the metal NPs that act as a key-lock mechanism with the proper ligands. The outgoing SERS signal usually belongs to the activated linker. In this frame, immunohistochemistry-like tests have been proven to work with several known cancer biomarkers and viruses, with limits of detection lower or equal to the common immunoassays adopted for multimodal analysis [16–22]. Similarly, nucleic acid-based multiplexed tests are pursued to detect specific sequences of DNA and RNA that might have a role in oncogenesis and other diseases [23–29]. In this case, the NPs usually reports ssDNA or small RNA probes complementary to the known wanted oligomeric strand, connected to the metal surface through a SERS-active linker.

Conversely, the *label-free* approach does not include any functionalization of the metal surfaces and admits the free adsorption of analytes on them Figure 1.1. In principle, all the constituents of the sample can be seen through SERS, but actually the metal-molecule affinity and the molecular features are the driving force for the SERS signal to occur. This issue is commonly faced when dealing with chemically complex specimens, like biofluids, as the spectral signature reveals only a fraction of the present species, namely metabolites and catabolites [30–33]. The biomolecules present in the adsorbed fraction depend on the sample characteristics, but for sure this approach is markedly different from the aforementioned labeled systems, as the whole spectrum can be seen as a multimarker detector. In the frame of diagnosis, the hypothesis is to consider the biological sample representative of the metabolic state of the subject, thus a reflection of the health status. Therefore, a correlation is assumed between the collected metabolites and the pathological condition [30,34,35]. Machine learning algorithms are part of this study too, as they are involved in the

construction of predictive models for diagnostic purposes, provided the large number of variables each measurement involves, unmanageable without informatic support.

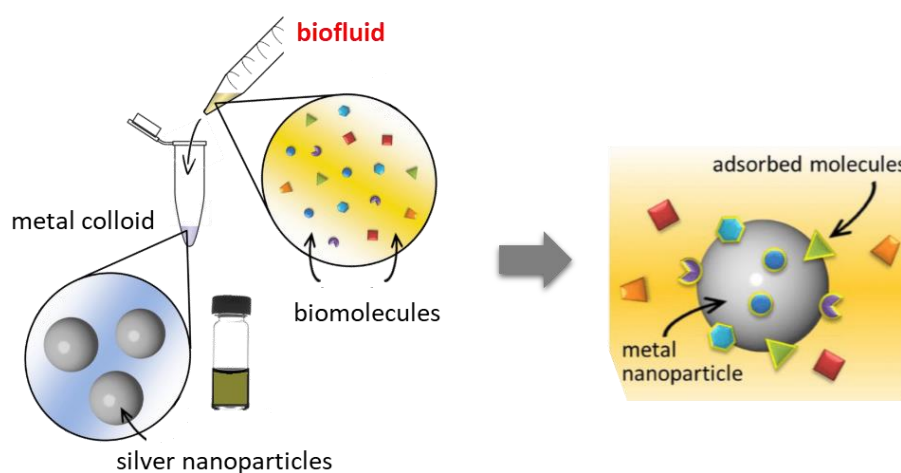


Figure 1.1 Label-free SERS analysis: analytes freely adsorb on the metal nanoparticle, driven by the affinity for the surface [36].

A further step in the direction of the POC devices is the introduction of solid supports decorated with SERS nanoparticles. After the first observation of SERS in 1977 by Martin Fleischmann with pyridine on an electrochemically roughened silver electrode, the first attempt for an application of solid SERS substrates dates back to 1984 with Tran and co-workers. These researchers exploited the use of paper as flexible substrate decorated with metal nanoparticles [37]. Silica slides [38,39], roughened electrodes, graphene sheets [40–43], carbon nanotubes [44,45], natural [46–48] and synthetic [39,49,50] polymers have been decorated with both labeled and unlabeled nanoparticles. Among all, the superficial roughness, flexibility, stability, tunable hydrophilicity, low SERS background, and low cost make paper an ideal substrate for SERS NPs deposition. For this reason, in this project paper has largely been used as substrate to build nanostructured SERS-active surfaces.

However, it must be observed that most of the studies available in literature about paper-based substrates report, at best, only partial aspects of their implementation. An inappropriate characterization of SERS substrates features a poor reliability of the results, and the improper design of the experiments and validation of the diagnostic performance are all issues which burden these reports, limiting the applicability of these substrates. Considering the SERS substrates preparation, the list of existent recipes and protocols is huge, but often their performance (in terms of robustness, accuracy, assay stability, cost, fabrication complexity, etc.) is inadequate, and the technology seems to remain far behind from the requirements needed to reach the market. Indeed, SERS substrate fabrication implies a complex coordination of extremely interdisciplinary fields that need to contribute to the realization of reliable

systems. To date, the few commercially available SERS devices are expensive because of the complex and time-consuming fabrication process and of the lack of competitors in the market.

1.2 Object of the research

The main focus of this PhD project was to assess the feasibility of the application of the SERS to bioanalysis and clinics, and in particular for the analysis of biofluids. Building on the expertise our research group has been developing in recent years [30,31,36,51], the conduct of this PhD thesis has a twofold nature, which aim to push the fundamental knowledge on the field and to discuss the feasibility of the application of SERS to biomedicine.

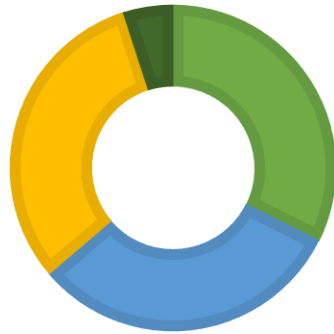
The core of the project reported in this dissertation is to present *label-free* metallic substrates as sensors for biomolecules present in biofluids based on citrate-reduced silver nanoparticles (cAgNPs), used both in their colloidal form and deposited on paper substrates, according to two protocols. The nanoparticles were not functionalized: the *label-free* approach has been used with the specific intent of developing versatile substrates, irrespective of the final application.

This PhD project has different aims:

- 1) to contribute to the building of *label-free* protocols towards the analysis of blood fractions (serum, plasma, erythrocytes, peripheral blood mononuclear cells, and whole blood itself) with SERS;
- 2) to understand the role of the protein corona in the modulation of the metabolites-nanoparticle interaction with model systems based on mixture of human serum albumin, human serum albumin (HSA), adenine, hypoxanthine, uric acid in the physiological range of concentrations;
- 3) to apply the aforementioned knowledge to the early diagnosis of several diseases (breast cancer, non-alcoholic fatty liver disease and hepatocellular carcinoma) through serum and plasma samples by means of multivariate data analysis (supervised and unsupervised) of SERS spectra.

Overall, the challenge is, on one hand, to obtain competitive substrates in terms of reliability, cost efficiency, ease of preparation, stability and versatility. On the other hand, another aim is to see how these substrates can be applied to biological samples, ranging from model systems to real clinical biofluids for diagnostic purposes, paving the way for POC devices.

RECIPE FOR SUCCESS?



- Good nanofabrication
- Proper ML algorithms
- Good protocols
- Luck

2 Raman Spectroscopy and SERS

In the last decades, the role of the vibrational spectroscopy in analytical chemistry has been widely explored, providing the possibility to get chemical and structural information on a whole range of physical states of matter. In the frame of Raman scattering, the chance of rapidly obtaining the vibrational fingerprint of a sample, the lack of interferences due to water – a common issue in other spectroscopic techniques - and the recent advances in the photonic technology, spread the application of the Raman technique and all its variants through the bioanalytical and medical area, going from the bench toward the patient's bedside.

In this chapter, an overview on the Raman effect and on the Surface Enhanced Raman Spectroscopy is presented, with a focus on the label-free approach, which has been widely used in this PhD project.

2.1 Raman Spectroscopy

When light interacts with matter, several phenomena may occur: it can be adsorbed, scattered or simply transmitted through it. Spectroscopy is the study of how these interactions, which involve transitions between electronic, vibrational and rotational energy levels, can yield information about matter. Raman spectroscopy is mostly concerned about vibrational and vibronic (i.e. vibrational + electronic) transitions. In the following paragraphs, a brief review on the most relevant aspects of vibrational spectroscopy is presented.

Raman spectroscopy is based on the inelastic scattering of light, a phenomenon of the matter-electromagnetic radiation interaction. The origin of the scattering can be in part simply explained with classical physics: as the incident wave interacts with matter, the charges constituting the object start to oscillate and emit electromagnetic radiation, in accordance with the classic electromagnetism theory. Raman spectroscopy detects the energy differences between the incident radiation and the radiation scattered from the sample, which ranges approximatively from the ultraviolet to the near infrared wavelengths. Information about the molecular structure and the chemical composition of the sample can be obtained from Raman spectra. In particular, vibrational spectra can be seen as typical, characteristic patterns (“fingerprints”) of the analytes and allow to qualitatively and quantitatively detect them [52].

The technique was named after Sir C. V. Raman, who first observed the phenomenon in 1928, together with K. S. Krishnan [53], but it has been postulated earlier in 1923 by Smekal [54]. Raman was awarded the 1930 physics Nobel Prize for this breakthrough.

2.1.1 Molecular vibrations

A molecule exists in a state of constant vibrational motion (even at 0 K). The nuclei oscillate around their equilibrium positions and the frequency of these periodic motions spans typically from 300 to 3000 cm^{-1} (wavenumbers, the typical unit used in Raman spectroscopy). Such nuclear motions within a molecule are called vibrational modes, and they can be always described as a linear combination of finite set of so-called “normal” vibrational modes. In general, the “degrees of freedom” describe the number of movements of a particle in the 3D space. One atom can translate in the three directions in the space (x, y, z), for an amount of three degrees of freedom. Three atoms alone would have $3N$ degrees of freedom, but when linked by a bond the translational motion is blocked and the trio can just rotate or vibrate normal modes of vibration. A non-linear molecule with N atoms has $3N-6$ degrees of freedom, whereas in a linear molecule only 2 vibrational modes are possible, thus $3N-5$ degrees of freedom because rotation around the bond axis cannot be observed. As a result, a diatomic molecule can have only one vibrational mode, a symmetrical stretching, and a triatomic one will have three modes: the symmetrical stretch, the bending and the asymmetrical stretch. The polyatomic molecules have mutually independent normal modes of vibration, but they involve simultaneous vibrations of different parts of the molecule. Figure 2.1 shows a schematic representation of the vibrational modes and their features. Overall, the symmetry of the molecule and the possible symmetry operations plays a crucial role in the assignment of the normal vibrational modes. However, a digression on this topic goes far beyond the purpose of this introductory paragraph, and the reader may want to refer to literature or textbooks for a detailed description [52,55,56].

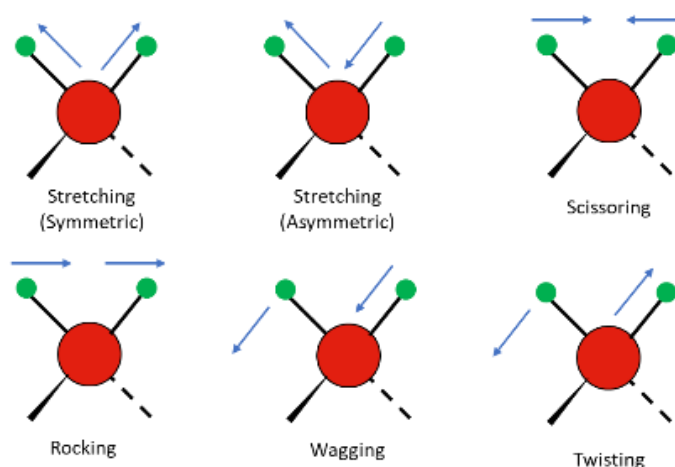


Figure 2.1 The vibrational modes

2.1.2 Raman scattering: background principles

Briefly, vibrational spectroscopy detects the energy exchange required to cause the nuclear motion that takes place during the light-matter interaction and the effect on the population of the vibrational levels. The Raman scattering mainly involves the ground state and the first excited energy level (overtone are very weak or not present). In these conditions, the harmonic approximation can be used to describe the system. Accordingly, atoms and bonds can be thought as balls and springs in a harmonic oscillatory motion. The Hooke's law is hence easily applied to the molecular system:

$$\tilde{\nu} = \frac{1}{2\pi} \sqrt{\frac{k}{\mu}} \quad (2.1)$$

$$\mu = \frac{m_1 \cdot m_2}{m_1 + m_2} \quad (2.2)$$

where $\tilde{\nu}$ is the oscillation frequency of the vibrational mode, k is the force constant that addresses for the spring (bond) strength, μ is the reduced mass for the system and m_1, m_2 are the masses of the atoms involved in the bond. It derives that the vibration frequency changes as the properties of the system changes, i. e., the stronger the bond, the lighter the atoms, the higher the frequency [55].

As far as scattering is concerned, when the incident light hits the molecule, this is excited to a not stable and non-quantized so-called "virtual" energy state, far above the vibrational energy levels. This means that scattering does not requires an incident frequency that matches the energy gap between the excited level and the ground state, since no absorption takes place (unless special cases are considered, see Resonant Raman). When the molecule goes back to its original energy states, the emitted radiation can be scattered in both elastic and inelastic modes, as depicted in Figure 2.2.

The overall energy balance must be respected, as:

$$h\nu_0 + E_i = h\nu' + E_f \quad (2.3)$$

with h Planck's constant ($6.626 \times 10^{-34} \text{ m}^2 \text{ kg s}^{-1}$), ν_0 the incident frequency, E_i the energy of the initial vibrational level, ν' the frequency of the scattered photon and E_f the energy of the final vibrational level.

In the elastic scattering, the incident radiation frequency equals the emitted one, so that no neat energy transfer occurs between the incident radiation and the molecule: this is called Rayleigh or coherent scattering and does not contain information about molecular vibrations.

The inelastic scattering, the nuclear motion involved during the vibration, is the actual Raman effect, which can be of two types: Stokes-type, with net transfer of energy from

the radiation to the molecule, and Anti-Stokes effect, with a net decrease of molecular energy and a concomitant increase in energy of the scattered radiation (Figure 2.2).

In the Stokes scattering, the molecule is in a low energy vibrational level (E_i) and, after the interaction with the light, it is promoted to a higher excited vibrational level (E_f). A photon is scattered with energy and frequency lower than the incident beam: $E_i < E_f$ and $\nu_0 < \nu'$.

On the contrary, in the Anti-Stokes scattering the molecule is in a high energy vibrational level (E_f) before the excitation and decays to a lower vibrational level (its electronic ground state, E_i). A photon is scattered with energy and frequency higher than the incident beam: $E_i > E_f$ and $\nu_0 > \nu'$.

As result, both Stokes and Anti-Stokes bands report information about the vibrational levels involved in scattering.

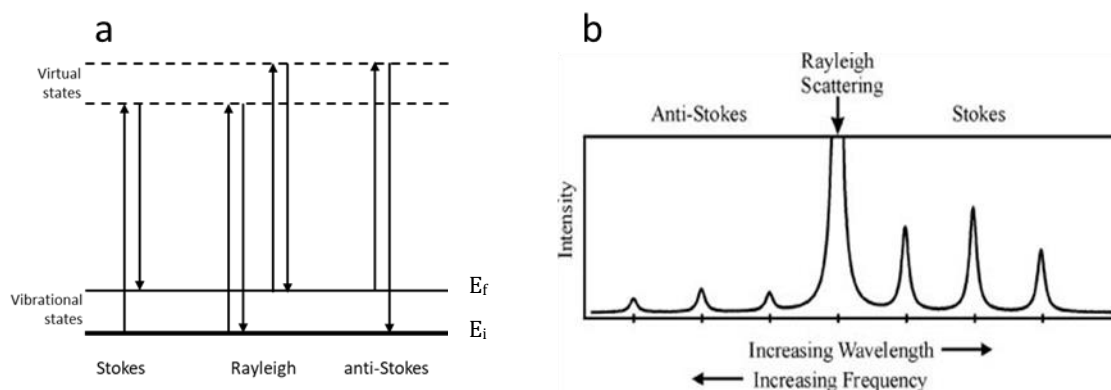


Figure 2.2 (a) Schematic representation of the three scattering modes. The Raman effect regards the inelastic diffusion, with changes in the frequency (and energy) of the emitted photon. (b) In the Raman spectrum, the Stokes and Anti-Stokes bands are symmetric with respect to the Rayleigh line, but with different intensities. Adapted from [56].

The spectra x-axes are reported in Raman shift units (cm^{-1}) as difference between the incident frequency (Rayleigh line) and the scattered photon frequency, both expressed in wavenumbers ($\tilde{\nu}$, in units of cm^{-1}):

$$\tilde{\nu} = \frac{\nu}{c} = \frac{1}{\lambda} \quad (2.4)$$

where c is the speed of light and λ is the corresponding wavelength. Anti-Stokes bands have negative Raman shift and the Stokes have positive ones. The Raman signal depends only upon the energetic gap between two vibrational states and is independent on the frequency of the incident laser, so that spectra of the same sample obtained from different instrumental set-up (namely, different lasers) can be compared.

One of the limits in the use of this spectroscopic technique is the overall signal intensity, that is several orders of magnitude lower than the source [14]:

$$I_{Raman} \approx 10^{-4} I_{Rayleigh} \approx 10^{-7} I_{source}$$

The Rayleigh signal is intense, whereas the probability for inelastic scattering to occur is very low (1 photon emitted on 10^6 - 10^8 incidents), resulting in weaker signals.

The Stokes and Anti-Stokes bands are symmetric with respect to the Rayleigh line, but their intensity depends on the difference in population of the vibrational levels, according to the Boltzmann's law:

$$\frac{N_f}{N_i} = \frac{g_f}{g_i} \exp \left[\frac{-(E_f - E_i)}{kT} \right] \quad (2.5)$$

Where N_f is the number of the molecules in the excited vibrational level (f), N_i is the number of molecules in the ground vibrational level (i), g is the degeneracy of the levels i and f , $E_f - E_i$ is the energy gap between the i and f levels, k is the Boltzmann's constant (1.381×10^{-23} J K⁻¹) and T is the absolute temperature [56].

As far as the temperature is concerned, the ground vibrational levels are highly populated with respect to the excited ones at ambient temperature. It derives that the Stokes bands results more intense than the Anti-Stokes ones. Accordingly, the working temperature could be derived from the Anti-Stokes/Stokes intensity ratio:

$$\frac{Intensity_{Anti-Stokes}}{Intensity_{Stokes}} \propto \frac{N_f}{N_i} \propto \exp \left[\frac{-(E_f - E_i)}{kT} \right] \quad (2.6)$$

To overcome the low intensity issue, the sample is irradiated with an intense monochromatic light, namely LASERs (Light Amplification by Stimulated Emission of Radiation), whose frequency ranges from the ultraviolet to the near infrared. Lasers are used for a few reasons:

- the Raman signal is very weak, as said, and requires many photons (i.e. an intense laser beam) to increase the signal to noise ratio;
- the frequency is far from the vibrational one and does not induce absorption phenomena;
- Lasers are extremely monochromatic, a prominent feature to improve signal resolution: the observed bands are only slightly shifted from the incident frequency and a broad incident frequency would hidden them or cause signal convolution.

As a note, if the laser energy closely matches the electronic transition energy gap in a molecule, resonant Raman scattering may occur. It results in a very intense scattering signal that may be confused with the absorption phenomenon: they actually differ in terms of the lifetime of the vibration, shorter in the resonance Raman scattering with respect to the adsorption. Another common interference is the fluorescence,

especially when dealing with biological samples, in the 275-975 nm region [57]. Excitation lasers with wavelength within this range can induce fluorescence that usually overlaps and hides the Raman signal. There are several ways to overcome fluorescence: the simplest is to use an excitation source outside the fluorescence region (i.e., 785 nm, 1064 nm) to consistently reduce the background. Otherwise, a physical separation of the two effects can be obtained by a Kerr gate system, that can clean the Raman signal from the fluorescence working on the different lifetime and optical properties of the two phenomena [58].

2.1.3 Raman scattering

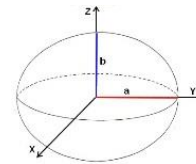
A brief mathematic demonstration of the Raman effect is reported hereafter.

As introduced in § 2.1.2, light propagates as oscillating electromagnetic wave and may induce an alteration of the electrons cloud that results in separation of charge within the molecules, called induced dipole moment ($\vec{\mu}_{ind}$). The induced dipole moment is proportional to the external electric field (\vec{E}), and the polarizability is the proportionality coefficient:

$$\vec{\mu}_{ind} = \vec{\alpha}\vec{E}. \quad (2.7)$$

The electric polarizability, $\vec{\alpha}$, is the optical property of a molecule that determines its scattering capability, namely how easily electrons can be moved in response to external field. The polarizability is defined as the tendency for the dipole moment of a molecule to be altered during an excitation and is a characteristic of the molecule. It is an anisotropic quantity and is described by a tensor (symmetric 3x3 matrix) and it can be depicted as an ellipsoid.

$$\alpha = \begin{pmatrix} \alpha_{xx} & \alpha_{xy} & \alpha_{xz} \\ \alpha_{yx} & \alpha_{yy} & \alpha_{yz} \\ \alpha_{zx} & \alpha_{zy} & \alpha_{zz} \end{pmatrix}$$



For the dipole moment alteration, the complete equation as matrices products is:

$$\begin{cases} \mu_{x,ind} = \alpha_{xx}E_x + \alpha_{xy}E_y + \alpha_{xz}E_z \\ \mu_{y,ind} = \alpha_{yx}E_x + \alpha_{yy}E_y + \alpha_{yz}E_z \\ \mu_{z,ind} = \alpha_{zx}E_x + \alpha_{zy}E_y + \alpha_{zz}E_z \end{cases} \quad \begin{pmatrix} \mu_{x,ind} \\ \mu_{y,ind} \\ \mu_{z,ind} \end{pmatrix} = \begin{pmatrix} \alpha_{xx} & \alpha_{xy} & \alpha_{xz} \\ \alpha_{yx} & \alpha_{yy} & \alpha_{yz} \\ \alpha_{zx} & \alpha_{zy} & \alpha_{zz} \end{pmatrix} \begin{pmatrix} E_x \\ E_y \\ E_z \end{pmatrix}$$

The external electric field \vec{E} has frequency ν_0 and oscillates with time as:

$$\vec{E} = \vec{E}_0 \cos(2\pi\nu_0 t) \quad (2.8)$$

For the sake of simplicity, the polarizability will be considered scalar and according to Eq. (2.7) the dipole moment can be rewritten as:

$$\vec{\mu}_{ind} = \alpha \vec{E}_0 \cos(2\pi\nu_0 t) \quad (2.9)$$

This means that the induced electric field oscillates at the same frequency ν_0 of the external field and corresponds to the Rayleigh frequency, when no Raman scattering occurs.

The polarizability matrix of a molecule is not a constant: it changes also due to the molecular motions and to the mutual orientation with respect to the external electric field. It depends upon the vibrational and rotational motions, but here only the vibrational part will be considered. Hence, variations in α are associated to the vibrational normal modes of the molecule (Q_k): α is a symmetric matrix and can be approximated as a Taylor series (terms beyond the first derivative are here neglected):

$$\alpha = \alpha_0 + \left(\frac{\partial \alpha}{\partial Q_k} \right)_0 Q_k \quad (2.10)$$

with α_0 the polarizability at the equilibrium position, $Q_k = Q_k^0 \cos(2\pi\nu_k t)$ in the harmonic approximation and $(\partial\alpha/\partial Q_k)_0$ as the change in α during the vibration normal mode. If $\Delta\alpha = (\partial\alpha/\partial Q_k)_0 Q_k$, and substituting Eq. (2.10) in Eq. (2.9):

$$\begin{aligned} \vec{\mu}_{ind} = \alpha_0 E_0 \cos(2\pi\nu_0 t) + \frac{1}{2} \Delta\alpha \cos(2\pi(\nu_0 + \nu_k)t) \\ + \frac{1}{2} \Delta\alpha \cos(2\pi(\nu_0 - \nu_k)t) \end{aligned} \quad (2.11)$$

Hence, vibrations can alter the dipole moment and induce the diffusion of photons with frequency:

- ν_0 , Rayleigh diffusion, typical of the molecule and equal to the incident radiation frequency;
- $(\nu_0 + \nu_k)$, Anti-Stokes diffusion and
- $(\nu_0 - \nu_k)$, Stokes Raman diffusion.

The gap, $\Delta\nu = \nu_0 \pm \nu_k$, is the so-called Raman shift.

A Raman scattering process occurs if the two frequencies, which are different from the incident one, are diffused. This condition derives from the induced dipole transition moment (\vec{M}_{if}) for the vibration normal mode Q_k that must be different from zero. In Dirac notation, this can be expressed as:

$$\vec{M}_{if} = \langle \nu_k | \vec{\mu}_{ind} | \nu_0 \rangle \neq 0 \quad (2.12)$$

It is demonstrated that this equation is true if:

- the polarizability varies during the vibration normal mode:

$$\left(\frac{\partial \alpha}{\partial Q_k}\right)_0 \neq 0 \quad (2.13)$$

- the vibrational levels interested in the transition are nearest neighbors: $\nu_k = \nu_0 \pm 1$.

These are the selection rules for the Raman effect to occur.

In other words, the polarizability is a measure of how easy it is to distort the present dipole moment or to induce a dipole moment in the molecule: apolar molecules would exhibit a larger $\Delta\alpha$ during the vibration with respect to the polar ones, as the electronic cloud in the latter case is already distorted. Moreover, vibration symmetry matters. For instance, an incident radiation can alter the molecular polarizability with respect to its symmetry. In general, a vibration is Raman-active if it has the same symmetry as the polarizability tensor of the molecule, reported in the respective table of characters. For all the other cases, on the basis of the symmetry of the molecule and of the vibration, it is possible to determine if a vibrational mode is Raman-active or Raman-inactive. As a note, for small and highly symmetric molecules the exclusion rule must be cited: vibrational modes that display Raman signal are Infrared inactive, and vice versa (Figure 2.3).

	In-phase stretch	Out-of-phase stretch	Bending
Mode of vibration			
Variation of dipole moment	 $\partial\mu/(\partial Q_k) = 0$	 $\partial\mu/\partial Q_k \neq 0$	 $\partial\mu/\partial Q_k \neq 0$
Variation of polarizability	 $\partial\alpha/\partial Q_k \neq 0$	 $\partial\alpha/(\partial Q_k) = 0$	 $\partial\alpha/(\partial Q_k) = 0$
Infrared active	No	Yes	Yes
Raman active	Yes	No	No

Figure 2.3 Effect of the vibrational modes on polarizability and on the Raman spectrum [52].

2.2 Surface Enhanced Raman Spectroscopy

A variant of Raman spectroscopy is SERS. This technique takes advantage of nanostructured metal surfaces that boosts the sample's Raman intensity up to 10^{10} times.

This enhancement, obtained by using a plethora of different nanostructured surfaces, instrumental set-ups and physical states of the samples, has widely spread the use of the SERS technique in several fields, from chemical physics, to analytical chemistry, electrochemistry, solid state physics, biophysics and medicine [59,60].

This effect was first observed in 1973 by Fleischmann and co-workers studying pyridine adsorbed on a rough silver surface [61], which displayed an enhanced Raman signal when adsorbed on a silver roughened surface. At first, they attributed the intense signal to a high degree of absorption of the analyte on the surface due to the roughness, but no enhancement effect was hypothesized.

It took few years to eventually get a convincing demonstration of fact that there was a huge signal enhancement and of the mechanisms involved in this process, which, to some extent, are still debated. Two main approaches are commonly accepted to explain the large SERS cross section and they were independently derived by two groups in 1977.

The first is a physical/electromagnetic explanation (called "electromagnetic mechanism"); it was provided by Jeanmaire and Van Duyne: the signal enhancement is due to an increase in the local electromagnetic field on the (roughened) metal surface, in the direction normal to the surface [62,63]. The molecules adsorbed on the metal surface experience a stronger electric field than the one due to the incident radiation, resulting in an increase of the Raman intensity, which is known to be proportional to the magnitude of the electromagnetic field.

The second mechanism, proposed by Albrecht and Creighton [64], is a "chemical" one: it is based on the occurrence of charge-transfer complexes between the metal and the molecules; this effect is strong for electron rich molecules with π electrons or lone pairs (such as aromatic compounds, carboxylic acids, etc.). The analyte is chemisorbed on the metallic surface, and, for all practical purposes it becomes a new chemical species with different geometry and electronic structure of the starting analyte: accordingly, the signal position and intensity may change. As far as the chemical mechanism is concerned, the reader is addressed to literature for further descriptions [14,52].

Moreover, according to Smith [56], it must be stressed that the two mechanisms are not strictly independent, since the molecule-metal interaction always implies the alteration of the electronic cloud, regardless its physical or chemical nature, which propagates at least within the first few molecular layers. This distortion may change the symmetry of a molecule and of the polarizability as well, so that SERS active modes may differ from the Raman active ones. The SERS "surface selection rules" relates to

the normal modes which alter the z component of the polarizability tensor, depending on the distance between the moiety and the nanostructured surface.

In general, the dominant condition for the enhancement of scattering in SERS is the generation of *plasmons* on the metal surface that allows the analyte adsorbed on the metal surface to experience a resulting enhanced local electromagnetic field with respect to the incident laser alone. The plasmons are the collective oscillation of the free electrons in the metal induced by the interaction with an external electromagnetic field oscillating at a frequency able to cause the displacement of the electrons from their shells. They are called *bulk plasmons* when the material is larger than the incident wavelength and, more specifically, *surface plasmons* when the oscillation occurs in a confined space near the interface between the material and an adjacent dielectric. Their existence was actually predicted by Rufus Ritchie in 1957 [65]. When the incident wavelength is larger than the material size, the collective electrons motion is called *localized surface plasmon* (LSP, Figure 2.4). If the incident frequency matches the LSP frequency, plasmonic absorption occurs, also known as *localized surface plasmon resonance* (LSPR) [66,67]. However, plasmons are “lossy”, that is they are not sustainable in the absence of an external energy source. The surface plasmons strictly relate to the optical and structural (size, geometry, roughness) properties of the dielectric surrounding the metal, and the advances in plasmonic science allows to correctly calculate the structure-SPR relation also for complex metallic nanostructures [67,68]. Moreover, LSPR can be finely tuned according to these optical and structural parameters and these features allow the customization of metal nanostructures for sensing and spectroscopic purposes.

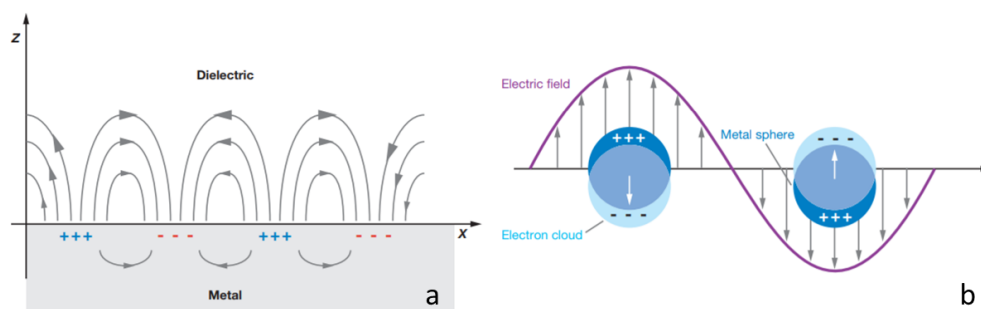


Figure 2.4 Schematic illustration of the surface plasmon (a) and of the localized surface plasmon (b) phenomena. Adapted from [67].

Since metal nanoparticles are not transparent in the UV-MIR range, where their plasmonic resonance occurs, they are useful for IR and Raman analysis. Only few metals are able to support surface plasmons and have the desired characteristics for SERS, the so-called coinage metals: silver, gold and copper. Other metals can also be used, such as aluminum, lithium, palladium, platinum, nickel, cobalt and iron. They are rarely used since they yield far more modest intensity enhancement and are less stable in biological medium and prone to oxidation, which, in turn, broadens the resonance linewidth. Practically, silver and gold are commonly used for their

properties, compatibility with the organic/biological samples, ageing and oxidation stability and with intense plasmon resonance frequencies in the NIR region [56]

2.2.1 The electromagnetic model of SERS

A complete theoretical treatment of the LSPR and SERS goes beyond the introductory purpose of this Chapter, and the reader is addressed to the dedicated literature for further details [30,69–74]. However, the bases of the SERS enhancement are reported hereafter considering a spherical nanoparticle (radius a) invested by an incident radiation ($\lambda \gg a$), according to the boundary conditions of the Mie scattering theory [75]. In this approximation, the electromagnetic field (E_{out}) around the nanoparticle is static and its magnitude can be easily derived from the Maxwell's classical electromagnetism equations (for more complicated cases, numeric solutions are to be calculated):

$$E_{out}(x, y, z) = E_0 \hat{z} - \left(\frac{\varepsilon(\lambda) - \varepsilon_m}{\varepsilon(\lambda) + 2\varepsilon_m} \right) a^3 E_0 \left(\frac{\hat{z}}{r^3} - \frac{3}{r^5} (x\hat{x} + y\hat{y} + z\hat{z}) \right) \quad (2.14)$$

The intensity of E_{out} falls off with distance from the particle's surface and depends on the incident wavelength, on the size of the particle, on its optical properties and on those of the surrounding medium.

The optical properties of bulk material are described by the permittivity or dielectric function $\varepsilon(\omega)$, while the medium is characterized by a dielectric constant ε_m . The dielectric function describes the behavior of a material in presence of an electric field. It is a complex number which accounts for the phases of the polarization of the material with respect to the external electric field. It depends on the wavelength (λ , or frequency, ν) of the incident light and on the electronic structure of the material itself:

$$\varepsilon(\lambda) = \varepsilon'(\lambda) + i\varepsilon''(\lambda) \quad (2.15)$$

Briefly, the real component of the dielectric function describes the phase offset between the incident and the response frequency, whereas the imaginary part accounts for the absorption of the radiation and the loss of energy.

The link between the optical properties of a material and its macroscopic behavior, is defined by Eq. 2.16, indicating that the metal polarizability could be derived directly from the dielectric function of the metal. For a metal sphere immersed in a medium with dielectric constant ε_m :

$$\alpha = a^3 \left(\frac{\varepsilon(\lambda) - \varepsilon_m}{\varepsilon(\lambda) + 2\varepsilon_m} \right) \quad (2.16)$$

where α is the metal polarizability, N is the particles density and $\varepsilon(\lambda)$ is the dielectric function for the metal nanoparticle. The term between brackets appears in Eq. 2.14 and defines the Enhancement Factor for the external electromagnetic field E_{out} , strictly related to the incident λ and to the radius a .

According to Eq. 2.16, the enhancement of the SERS signal is effective only when the resonance condition is satisfied, that is when the denominator is equal to zero:

$$\varepsilon(\lambda) = -2\varepsilon_m \quad (2.17)$$

The factor 2 accounts for the spherical nanoparticle but can take on different values for other geometries. According to this condition, only materials with proper dielectric functions are active in the excitation spectral range and the dielectric constant of the surrounding medium directly affect the intensity and the frequency of the plasmonic adsorption. Among all, the so-called coinage metals present this feature for a large range of wavelength (see Par. 2.2). For noble nanoparticles (Au, Ag) the condition in Eq. 2.17 is met in the visible range, namely at the plasmonic resonance frequency [67,74].

As far as the SERS application is concerned, part of the energy of the plasmon is transferred to the adsorbed molecule to induce a change in polarization. This process is near-field and decreases with the 10th power of the distance from the metal surface ($I_{SERS} \propto d^{-10}$) [67]. Data from literature report that almost the 90% of the SERS signal derives from the very first layer of molecules adsorbed on the metallic support [56]. The signal intensity ratio between the SERS and the classic Raman peaks is described by the Enhancement Factor (EF) at the surface, namely how much the presence of a metallic substrate can boost the electromagnetic field and the scattering signal. To a first approximation it can be described as:

$$EF(r, \lambda) = \left| \frac{E_{out}(r, \lambda)}{E_0(r, \lambda)} \right|^4 = \frac{I_{SERS}/N_{surf}}{I_{Raman}/N_{vol}} \quad (2.18)$$

With r the distance from the nanoparticle surface and λ the incident wavelength. The right part of the equation regards how the EF can be experimentally measured, with I_{SERS} the intensity of the SERS signal normalized by the number of molecules adsorbed on the enhancing substrate N_{surf} , and I_{Raman} the correspondent normal Raman intensity for the same molecule, normalized by the number of molecule in the excited volume, N_{vol} .

2.2.2 SERS: geometry and aggregation effects

As the LSPR condition on the metal surface can be tuned working with proper systems geometry (both size and shape), also the intensity of the SERS response can be boosted by several orders of magnitude.

To simplify the mathematical derivation, the conditions for the locally enhanced resonant electric field are true for particles ranging in diameter size from 10 to 100

nm. A diameter lower than the incident radiation wavelength allows to consider the external electric field homogeneous across the particle. Sizes larger than 100 nm induce a dramatic drop of the EF, due to the simultaneous excitation of multiple interfering surface plasmons, while few nm sizes do not exhibit effective resonance with the incident light and do not contribute to the SERS effect.

The size-related issue is still open, considering different shapes, since the EF conditions relates differently with each of them: nano- cylinders, spheres, stars, rods, etc., present several resonance conditions depending upon the wavelength of the incident radiation, the orientation with respect to the electric field and the position on the particle. For each system a proper electromagnetic description is available. Even fractals are an important class of clusters where single particles self-assembly with symmetric branches to form aggregates [13,69].

Indeed, aggregation matters. In particular, the dimeric system of coupled nanoparticles is, so far, the highest SERS enhancer, and aggregation is the key to get a SERS signal up to 10^6 times the one obtained with the single particle approach and $\sim 10^{11}$ times the classic Raman signal, thus making single-molecule detection feasible [23,76]. Moreover, the orientation is crucial for the scattering to occur: the external electric field must oscillate parallel to the interparticle axes to generate the strongest plasmonic coupling, and the vibrational modes involving changes in the polarizability perpendicular to the surface are preferentially enhanced. Conversely, when the exciting electric field is orthogonal to the interparticles axes, the enhancement is significantly lower and similar to the one provided by the single isolated particle (Figure 2.3).

The interparticle locations are the so called *hot-spots*: they are generated both between aggregated colloidal particles and on rippled surfaces due to the coupled plasmon resonance[69,77,78] . For effective performances, every SERS platform design requires homogeneously distributed hot-spots with optimized enhancement intensity, not always an easy task.

To sum up, the nanoparticles can be geometrically tailored to produce the desired LSPR. Besides, the number of parameters that can be tuned to optimize the EF demonstrates how rich and complex the phenomenon is and, therefore, the variety of the possible applications of the LSPR effect.

2.2.3 SERS substrates

In the last 15 years the surface enhanced Raman spectroscopy has been given a new input in terms of application for both quantitative and qualitative determinations, because of the advances in nanotechnology and photonics. To date, the potentiality of the LSPR in terms of signal enhancing, molecules detection and quantification is clear. However, to transfer the theory into robust, sensitive and reliable practical platform is still a very challenging task [66].

Nanofabrication follows two approaches: the top-down, and the bottom-up procedures (Figure 2.5). The first consists in a physical etching of surface by removing part of the substrate to shape a nanostructured pattern. The second concerns the (usually) wet chemical synthesis of nanoparticles that act as building blocks, then added one to another to form a nanostructure. Both may have advantages and drawbacks in their fabrication and applications. Overall the bottom-up approach allows a great differentiation of the final product in terms of chemical composition and shape. In this PhD project, only the bottom-up approach has been used.

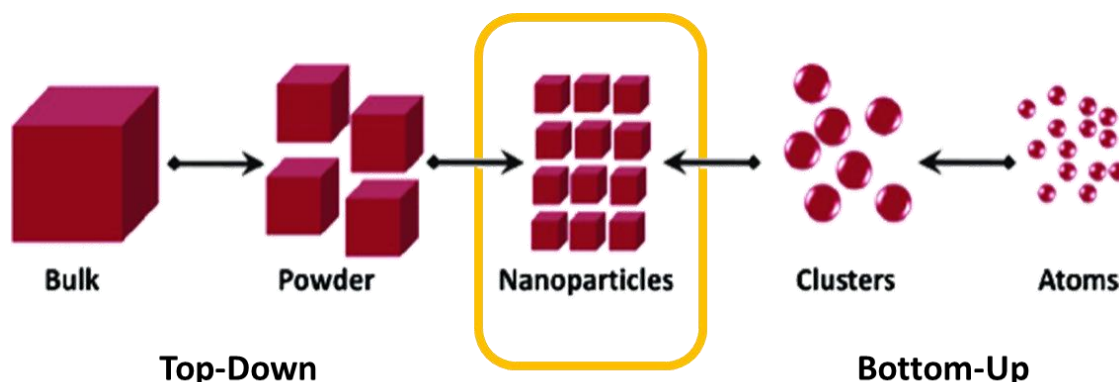


Figure 2.5 Actual concept for the top-down and bottom-up strategies.

Focusing on the bottom-up NPs fabrication, the SERS substrates can be classified in two types: the colloidal and the non-colloidal substrates.

Colloidal nanoparticles are commonly prepared by chemical synthesis [23,79] or by laser ablation [80–82]. They may require stabilizing agents, namely ions to stabilize charge repulsion [83] (i.e., sodium citrate, hydroxylamine, etc.) or short polymeric sequences (i. e., PEG, PVP) to sterically stabilize the NPs [84]. These elements alter the surface chemistry of the NPs and the way they can interact with analytes. Customization is possible and a plenty of protocols can be found in literature.

A solid substrate is a device that must be stable in time, especially toward oxidation, compatible with the specimen physical form, providing good signal-to-noise ratio, with the additional benefits of being manageable and ready-to-use. One of the foremost aspects to look for is the homogeneous distribution of the hot-spots to guarantee the measurement repeatability for quantification purposes. In particular, the ideal device should be reproducible, sensitive, not invasive, with a simplified sample processing, relatively inexpensive, possibly able to work in liquid environment and with small volumes. However, the lack of signal repeatability has been demonstrated to be always the main issue, hampering the application of the SERS technique for quantitative determinations. Considering the biomedical area, the aim is to obtain a device that may be used as point of care use for diagnostic applications [11,31,85] or for target drug monitoring [86].

Actually, the very first solid substrate belongs to Fleischmann et al. (1974) who first observed the SERS effect on a roughened silver electrode [61]. Ever since, several supports have been tested. Silica and glass have been used for both top-down (metal wires growth) and bottom-up approaches (physical or chemical deposition of metal nanoparticles on the planar surface) [69]. The resulting substrates may present inhomogeneity of the hot-spots distribution, leading to a poor intra-substrate reproducibility of spectra. Moreover, the neat and non-porous surface may imply long and controlled sample preparation procedures. Galvanic displacement can produce highly enhancing substrates for the spontaneous electrochemical reaction occurring in solution when a metallic ion displaces bulky metallic atom on a semiconductor surface. Several protocols exist to this aim, but still the reaction is random and poorly controllable [87,88].

Recently, Polavarapu and Lis-Marzan [89] introduced the advantages that flexible plasmonic substrates may lead in the field, compared to the conventional glass-based substrates, being more efficient in terms of cost, fabrication and use. Hence, paper revealed to be the substrate that may match all the featured described above. Paper is an extremely cheap, customizable and versatile support that is commonly used for strip test-like applications. Being porous, substantially inert, absorbent and with customized polarity, it is suitable for liquid samples and for biosensing.

Porosity and capillarity make paper suitable for several sample deposition technique, i.e., dropping or imbibition. In the first case, few microliters of the sample are deposited and dried as a spot-on assay: studies demonstrated how the dehydration procedure allows a homogeneous distribution of the analytes across the cellulose 3D structure [90], hence across the embedded NPs. In the second case, a separation and concentration of analytes can be seen according to polarity or size [91], as in a dipstick assay.

Nevertheless, the reader should be aware that the paper interconnected structure is far from being perfectly balanced and homogenous, irrespective of its degree of crystallinity or chemical purity. The roughness and the pore size distribution of the paper are like a double-edged sword: from one hand, they are the key for a higher enhancement factor since they allow the NPs to be better retained and to get a closer three-dimensional proximity with respect to the non-porous silica or glass substrates. On the other hand, the irregularity of the surface may induce local and irregular aggregation itself, undermining the reliability of the substrate in terms of repeatability of the SERS signal [8,10].

Literature reports how some kind of pre-treatment of cellulose prior to the NPs deposition can prepare the support for a more randomized distribution of the hot spots, in terms of regularization of the surficial roughness and porosity after specific pH-washings [8] and in terms of aggregation of NPs on the surface [92].

Moreover, the instrumental set-up may allow to collect scattering from a large volume (in terms of penetration of the laser in the network of cellulose fibers and of the

overall focal volume), thus averaging the possible inhomogeneity of the signal originating from different location, which, in turn, partially overcome the reproducibility issue. Within these limits, the paper-based SERS substrates could be considered homogeneous systems.

Some examples of the NPs deposition on paper includes the ink-jet based strips[91], the electrospinning [93] and the dip coating [51] (Figure 2.6). In the case of ink-jet printing, the ink is constituted by the metal colloid itself, which can be micro-sprayed directly onto the paper. The optimization of the process (paper porosity, ink viscosity and surface tension, etc.) can be potentially extended towards a portable analytical apparatus. The electrospun technique provides homogeneous stratification of the polymeric matrix and the NPs [94,95] but requires a complex set-up and a specific device to be prepared, thus the quality-cost ratio is not favorable. The dip coating is by far the most popular technique, as it is the simplest and does not require any kind of instruments. Paying attention on the NPs chemistry, they just need to precipitate on the support

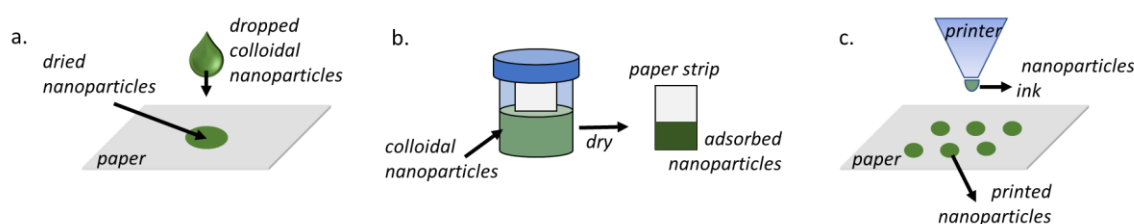


Figure 2.6 Some example of NPs deposition on paper (adapted from [96]). (a) Drop casting, (b) dip coating, (c) ink-jet printing.

2.2.4 SERS and the label-free approach for biosensing

In the frame of a bioassay, whether to go for a labeled or unlabeled substrate depends on the specific application.

In the “omic” era, the amount of information that can be retrieved from a biological sample is overwhelming, but still the challenge is to identify which are the most relevant information in the bunch and multivariate data analysis can give some keys to this end.

Genomics, proteomics, microbiomics, lipidomics, transcriptomics, metabolomics are some of the branches that have grown in the last two decades since they led to the rapid discovery of several possible biomarkers for diagnostic and theranostic purposes. To date, all the techniques belonging to these fields are basically devoted to find and characterize biomolecules that are involved in disease-related biochemical pathways, like chromatography-coupled mass spectroscopy, fluorescence spectroscopy, immunoassays tests, but only few of these have turned into realistic applications [97].

The new challenge is to change point of view and to move from the classic “single to few biomarkers” detection to reach the multiscale data, namely from a targeted approach to an untargeted one. The purpose is to consider the whole signal as a fingerprint of the actual situation, as a multi-marker, irrespective to the used technique.

SERS substrates fabrication may include, or not, the chemical functionalization of the nanostructure. The labels on the NPs are the key for the detection of specific molecules: the substrate is chemically tailored *a priori* in order to identify a specific target [36,98,99]. Functionalized multiple arrays are a step forward in the SERS detection of metabolites, but it is still complex to build.

The label-free method, on the contrary, employs NPs without any tag, naked, apart from the shield that works as capping and stabilizing agent: all the molecules present in the specimen can virtually reach the SERS surface, irrespective for their nature, though with different kinetics [13,36,100]; the final spectra would reflect the affinity of the analytes for the metal surface.

Indeed, in the present work the label-free approach has been used, with the specific intent to propose highly versatile SERS substrates, simple in nature and simple to use.

The reader is addressed to the next chapters for further comments on the NPs synthesis.

3 Multivariate Data Analysis

Nowadays, multivariate data analysis is a fundamental tool to dig into the huge number of variables loaded in a spectral dataset. The possibility to correlate the SERS spectra of a biofluid to the correspondent metabolic profile has been established. May the state of health of an individual be predicted too? When spectroscopy meets the possibility to perform clinical diagnosis, the issue inevitably becomes multivariate. In this Chapter some basics of the used algorithms are reported.

3.1 A primer on machine learning

Data analysis is an integral aspect of the measurement procedure. When dealing with large number of variables, typically from dozens to thousands, traditional methods of univariate analysis fail in the illustration of the relation among variables, hence we tend to miss it. Multivariate Data Analysis (MDA) provides a series of tool meant to reduce the complexity of the system down to its fundamental structure. This allows the pattern behind data to emerge. Simply, the human eye is not able to figure out how systems described by more than 3 variables, 3 dimensions, work. We need to be able to classify the elements of a dataset according to a reduced number of significative features to have a better and complete understanding of what we are looking at. In the measurement process, we try to categorize samples according to their properties: if some samples are similar, they may cluster and be separated from others. Often, the instrumental output is very complex and difficult to interpret. This is the case of the vibrational technique, where every wavenumber in the considered spectral range is a variable. The same can be said for other kinds of analytical set-up (i.e., gas chromatography, mass spectrometers, magnetic resonance, hyphenation between them, and so on). Chemometrics is the name given to the branch of science that offers a set of mathematical and statistical tools for the characterization of the chemical measurement process. Chemometrics found its renaissance in the 21th century with the development and diffusion of software that improved this analytical method. To date, MDA plays a major role in analytical chemistry, boosted by the prominent role that machine learning and artificial intelligence are assuming nowadays in several aspects of everyday life, industry and research [101].

MDA can be applied to both qualitative and quantitative determinations. that can be done through two kind of “learning” methods: the supervised and the unsupervised learning. These are roughly divided into three branches: classification, regression and

clustering. There are some similarities between classification and regression, as they try to find a function or model, which describe a known system (training set), able to predict the class or the value of one or more unseen observations (test set). The observations used to train the model have to be labeled, namely that we must know to which class or value they belong to and the label itself is one of the inputs of the function of model: this is what the term “supervised” learning is for. In particular, regression works on continuous quantities (i.e., concentration ranges), whereas classification on discrete class label (i.e., control/treatment, healthy/unhealthy).

On the other hand, other techniques do not require a full characterization of the training set, like in the unsupervised learning methods. Accordingly, the learning process is not oriented by class membership. Clustering is one of those: it finds a pattern among data based on the similarity between observations. Semi-supervised learning is a third option, useful when not all the observations are labeled but we need to visualize a similarity pattern according to the known elements. Learning methods can also be hyphenated. For instance, in presence of large dataset with a large number of variables, the classification process often needs to deal with a simplified description of the original dataset. To this aim, dimensionality reduction algorithms allow to turn the space of the original variables into a new space of the so-called latent variable. The transformation depends on the chosen algorithm, which can be both supervised or unsupervised. In any case, it allows to exalt the features that better characterize the system, avoiding noise, collinearity, redundancy, uncorrelated variables.

In this Chapter, we are going to briefly introduce some algorithms of both supervised and unsupervised learning and a combination of those, for the sake of classification. The focus regards the models built as integral part of the diagnostic procedure regarded the qualitative classification of spectra belonging to samples of known clinical outcome, which will be addressed in § 7.

3.2 Data analysis workflow

A proper classification method cannot ignore a proper data analysis workflow. The scheme in Figure 3.1 illustrates the pathway followed to build the classifier. One of the most relevant aspect to visualize the performance of a model passes through the proper validation of a predictive model. This is relevant especially when the sample size is not big enough to admit an external independent set of data on which test the model and predict the classification. Usually, the minimum size of a dataset for a robust prediction contains at least 80 samples for each class [102]. Resampling from the same dataset is the way and cross validation (CV) is an option: the dataset is divided into k segments (“ k -fold CV”), one of which is kept as independent test set outside the predictor building, while the other elements undergo preprocessing, feature reduction, prediction (Figure 3.1). At this point, the left-out segment is

recalled, and the classification model is applied to it. In supervised learning, a model shows a good performance when it is able to assign class membership correctly. When the segment k is made of one element, the CV is called “leave-one-out” (LOO). Although at each implementation the system is underrepresented (i.e, outlier classification results always wrong and affects the performance of the predictor) and the estimation can suffer of high variance, accordingly, the LOO-CV is the simplest CV method that we considered suitable for a preliminary classification routine on the reported case of study. Different and more articulated solution will be soon addressed in more tailored classification algorithms.

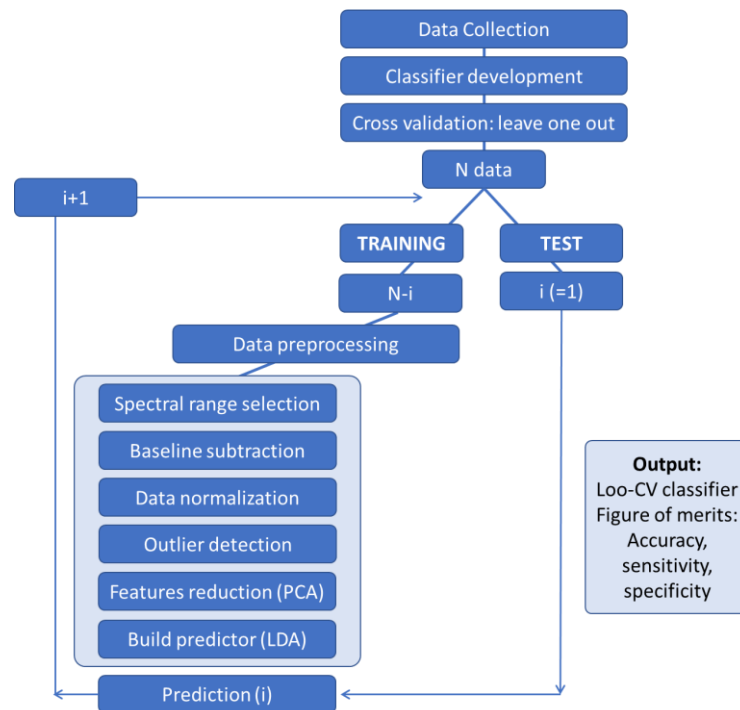


Figure 3.1 Data analysis workflow with leave-one-out cross-validation.

3.3 Principal Component Analysis

Principal Component Analysis (PCA) is an unsupervised learning method that is used primarily for dimensionality reduction. This means that the system can be efficiently described in terms of few features that main characterize it, without suffering of information loss. The algorithm allows to rotate the original variables into a space of uncorrelated latent variables, or Principal Components (PCs), and to rank them according to the proportion of variance they retain. In other words, the first PC spans the direction of the variable with the largest variation throughout the system, the second PC spans the second direction, and so on. The total number of PC corresponds

to the total number of variables. There will be a threshold beyond which the PCs would account for collinearity (i.e., variables that changes together, like the points that form a vibrational band), redundancy, and noise. The aim of the dimensionality reduction is to identify this threshold and to discard that slice of unnecessary information, flattening the dataset down to a reduced-variables system.

In practice, all the n observations (samples) and the m observed variables (spectra) can be described in a $n \times m$ matrix, here called X . PCA consists in the orthogonal projection of the original coordinates into the new space of the so-called principal components (PCs). This method is based on the properties of the covariance matrix: PCA assumes a normal distribution of the variables that describe the dataset, hence data can be scaled according to the mean in order to emphasize the difference among observables, since the covariance matrix includes all the statistical information associated to the original dataset. In some cases, data can be also centered to normalize the variance. In our specific case, centering is not suggested to avoid noise amplification. Briefly, data matrix X can be described as the sum of the information loaded in the PCs which are ranked according to the variance explained by each PC. In this way, it is possible to reject part of the unnecessary data (noise, uncorrelated variables, ...) taking into account only the first “ n ” PCs, namely filtering the relevant information loaded in the dataset looking at the cumulative variance. Data reduction through PCA accounts for this kind of transformations. Each PC originates from the product of the “scores” vector (U , $n \times k$) and the transpose of the “loadings” (V , $k \times m$) vector: the scores are the new coordinates of the observables (the spectra) on the PCs space. The product UV^T is an approximation of the original dataset X , plus the error included in the residual matrix E .

$$X = UV^T + E$$

They contain the information of the original data in the new rotate space of the PCs. The first element of the scores matrix and the first element of the loading matrix are also called eigenvalues and eigenvectors, respectively, for the first principal components (Figure 3.2). Each subsequent pair of eigenvectors and eigenvalues belongs to the following PCs, all ranked according to the variance. The loadings are the coefficients of the linear combinations that define the PCs and account for the weight each observable has in the PCs. Scores and loadings should be read together, since the distribution of the scores reflects the trend of the loadings and allow to define the variables that mostly vary within the dataset samples. In other words, this transformation allows to find for which variables the system changes the most, namely which variable better characterize the dataset [103,104].

3.4 Linear Discriminant Analysis

Linear Discriminant Analysis (LDA) is a supervised classification method, hence it requires knowing *a priori* the class membership of each observable, the labels. It is similar to PCA, but it focuses on maximizing the separability among known categories or classes. Given two categories to be separate, the new axis is created considering two criteria simultaneously: (i) maximization of the distance between the means of the categories once projected on the new axes, (ii) minimize the variation within each projected category. LDA uses the information provided by the observation (variables) to create new axes and to project the original variable on it in order to maximize the separation of the categories. Just like for the PCA, LDA ranks the new coordinates in order of importance, namely the first linear discriminant component would account for the most variation between the categories. Instead of PCA, in LDA the new system of coordinates rises from the calculation of two covariance matrices, accounting for the between-class and within-class covariance.

The rationale in the hyphenation of PCA and LDA is simple: PCA is used as a tool for dimensionality reduction by maximizing the variance, and its scores (a certain number of principal components, usually less than 10) are used to build the LDA predictor which tries to find the axes to amplify the interclass separation (Figure 3.3). The parameters used for such classification are then applied to the test set, in our case the one element left out. The procedure continues until all the elements have been used as test and their membership predicted.

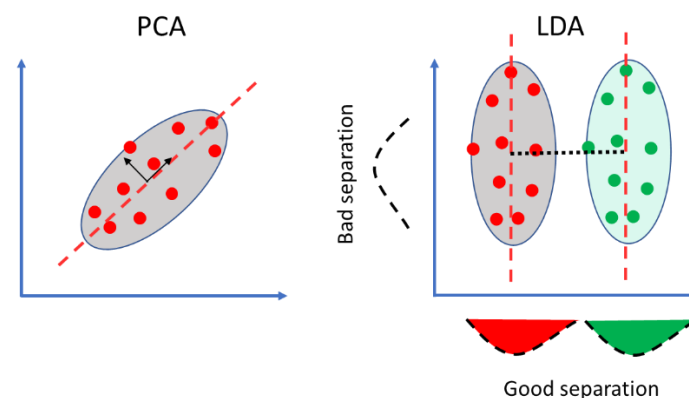


Figure 3.3 PCA identify the direction along which variance is maximized (black arrows), LDA uses this information to find the axes that increase the group separation.

The performance of a classification, then, can be calculated through the confusion matrix, a table in which the actual label of the element of the dataset are reported row-wise and the predicted value column-wise. The larger the correct classification, the better the performance. The principal diagonal accounts for the true positive (TP) and true negative (TN) classification (assuming a two-class classifier), while the other diagonal reports the false positive (FP) and the false negative (FN) outcomes. The

figures of merit (accuracy, specificity, sensitivity, positive predicted values – PPV, negative predicted value - NPV) are calculated from this platform.

		Actual		
		+	-	
Predicted	+	TP	FP	Sensitivity = (TP / (TP + FN))
	-	FN	TN	Specificity = (TN / (TN + FP))
				PPV = (TP / (TP + FP))
				NPV = (TN / (TN + FN))
Diagnostic Accuracy = ((TP + TN) / (TN + FP + FN + TN))				

Another performance evaluator is the ROC (Receiver Operating Characteristic) curve and the AUC (area under the - ROC - curve). They represent the trend of the predictor performance and accounts for how many TP are classified for every TN. The AUC can range from 0 to 1, where 0.5 represent a classification accuracy not better than simply guessing the outcome. The perfect classifier would have an AUC equal to 1. For some examples of the curve, refer to § 6.

For more exhaustive insights on chemometrics tools and methods, the reader is referred to dedicated literature [101,103,104].

4 Adsorption models

This chapter means to be a roadmap for the overall practical aspects unraveled throughout the PhD project. Some foundations are introduced, from the basic aspects of the adsorption process required for the SERS effect to occur.

4.1 The adsorption process

The SERS effect in the label-free case is possible if the proximity condition between the metal nanoparticle and the analyte occurs. The theory of the adsorption process is widely described in literature, as it belongs transversely to all the scientific fields. Skipping for a while the SERS selection rules behind the spectroscopic signal, let's consider the basic adsorption of the molecule approaching the metal NP. Once the analyte is adsorbed on the metal surface, the intensity of the scattering signal depends on the orientation of the molecule and its moieties, on its concentration, and, of course, on the chemical affinity between the two. Accordingly, spectra can help us in the identification of an adsorption process only looking at the evolution of the intensities of specific bands versus time, concentration or sample preparation in general. It derives that every analyte-NPs match opens the way to a new adsorption mechanism. This is why a unique adsorption process has not been yet fully described. To understand the process, here few theoretical bases.

The adsorption is a phenomenon characterized by the transfer of a molecule (X) from a vapor or liquid state to active sites on a surface (M).



Virtually, the process can proceed up to the saturation of the surface's sites. When a molecule interacts with the surface by weak electrostatic forces (London, van der Waals) a physisorption occurs; when a molecule forms a covalent bond or a charge transfer with the surface, we are dealing with chemisorption. The physisorption process is aspecific, reversible, activation-energy-free and can lead to multilayer association, whereas the chemisorption process involves high heat of adsorption, is irreversible, specific, and forms monomolecular layers. In general, the phenomenon occurs when the adhesive force between the floating molecules and the unlike solid surface are greater than the molecule-molecule cohesive forces (and the solvent-molecule interaction, in liquid phase).

The process can be both thermodynamically and kinetically driven, according to the chemical and physical features of the involved species. From a thermodynamic point of view, the adsorption of a molecule implies a reduction of its concentration in the

surrounding medium at equilibrium, thus a loss in mobility and in system entropy. Thereby, the process should be exothermic, since a negative enthalpy difference must be observed to keep a favorable free-energy change, namely $\Delta G < 0$ in $\Delta G = \Delta H - T\Delta S$. In other words, the chemical potential in the surrounding medium is higher than the chemical potential at the surface [105]. From a kinetic point of view, in presence of a mixture species, the adsorbate composition can change over time: crossing the steric effects due to macromolecules, alteration of the preferential orientation of the molecules with respect of the surface, evolution of the mono/multilayer structure and diffusion gradient are some examples.

Adsorption isotherms are the experimental (or simulated) way to describe the phenomenon and reflect the specific number of molecules that go from the surrounding medium to the solid surface (or the fractional coverage, θ) with respect to the external pressure applied to the system (in gas phase), namely to their concentration (in solution), at the equilibrium state and in isothermal conditions. Notably, for porous surfaces, the walls of the pores are accounted: the larger the total surface, the larger the number of attracted molecules. The shape of the isotherm is related to the nature of the adsorption and mathematically described within *ad hoc* boundary conditions. Five principal adsorption mechanisms in their boundary conditions have been described by Brunauer (1945) [106], later extended to empiric models, here summarized in Table NN. These theories are connected to how and why the adsorption process is measured, commonly via gas or water sorption to estimate the surficial area and cumulative porosity of a solid. Actually, the interpretation of the physical-chemical and mathematical data *in se* is independent of the detection method, hence the theories are extendible to different experimental set-up to retrieve the binding coefficients (K).

In the frame of the adsorption on label-free SERS surface, the adsorption kinetic curve can be obtained through a univariate analysis of the area or intensity of concentration sensitive peaks. Accordingly, the ordinate value can be considered as an approximation of the fractional coverage, θ . Moreover, it is necessary to assume the monolayer approximation as a boundary condition as the SERS effect derives only from molecules that lie within few nanometers far from the metal surface, namely from the first coverage shell. Two main trends are observed: the Langmuir-like and the sigmoidal one. In the first case, the metal-molecule affinity is so tight that a fast adsorption occurs: the signal increases almost linearly with the concentration (A) up to the saturation plateau (B), that is the concentration at which all the possible sites are bounded, in the monolayer approximation. The slope of the initial linear trend and the saturation point depend closely on the analyte-metal peculiar interaction. The hyperbolic trend follows a Langmuir-like curve that can be easily extended to this case as well as the interpretation of the coefficients (refer to Table 4.1 for further descriptions). In the second case the adsorbates are not likely to be independent one to another: a cooperative behavior is referred to a typical sigmoidal adsorption trend (Figure 4.1). In this frame, the term cooperativity means that the ligand-surface

interaction on a site is influenced by the presence of a ligand on a close site: it can be positive, if a molecule is more likely to bind the surface, negative in the opposite case and non-cooperative if the mutual interaction does not affect the adsorption rate. Positive, negative and non-cooperativity are due to the peculiar chemical affinity between the species. Several kinetic adsorption models have been developed to describe a Type V isotherm [107], although often addressing to multilayer adsorption. In the monolayer approximation, the Hill equation can be borrowed from the biochemistry and describes the cooperative interactions between one or more ligands and the binding site in a macromolecule [108].

It is worth noting that the Langmuir-like curve can be included as a non-cooperative trend (Figure 4.1), as the Hill equation is formally the same [109]. The n parameter is the cooperativity coefficient, where:

$$\begin{cases} n > 1 & \text{positively cooperate binding} \\ n = 1 & \text{noncooperatively binding (Langmuir)} \\ n < 1 & \text{negatively cooperative binding} \end{cases}$$

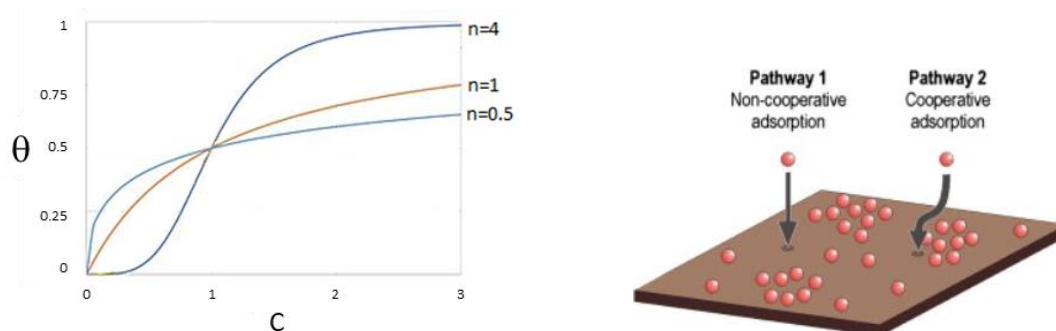
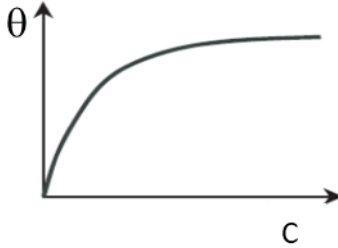
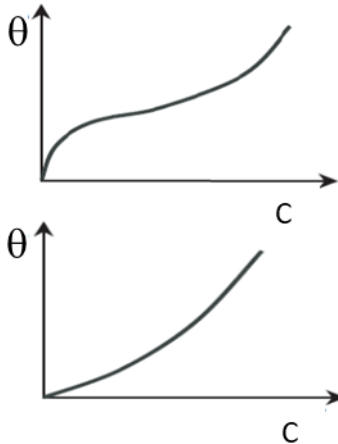
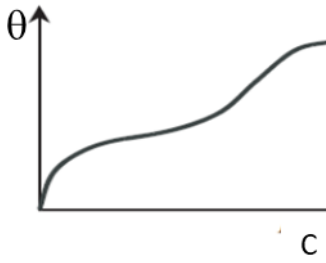
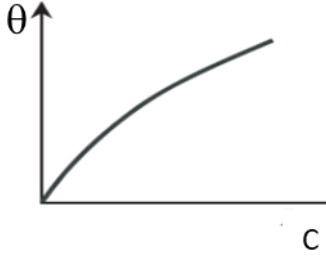
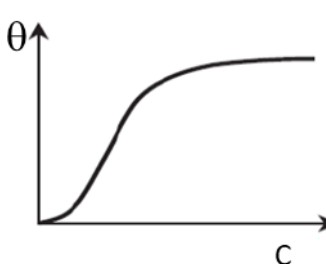


Figure 4.1 (Left) Type of cooperative behavior; (right) schematic representation of the cooperative behavior induced by the lateral interaction effect.

For the positive cooperation, the typical sigmoidal curve shows an inertial beginning (A), where the signal is not susceptible to concentration change (low surface coverage), a dramatic increase in the adsorption rate (B) that culminate in the final plateau (C), in which the monolayer condition or the maximum number of molecules is reached. The A and C regions indicates the minimum and the maximum concentration limits below and above which no quantitative detection can be obtained through SERS. In particular, for the above-saturation point the same aforementioned considerations can be drawn. From both the Langmuir-like and Hill equations, the binding coefficients can be retrieved.

Table 4.1 Summary of some of the most used adsorption theories and equations.

Adsorption Theory	Plot	Boundary Conditions	Equation	Parameters
Langmuir		<p>Monolayer approximation</p> <p>Binding sites energetically equivalent</p> <p>Absence of intermolecular interactions</p> <p>Absence of phase transition at the surface</p>	$\theta = \frac{Q_0 K C_e}{1 + K C_e}$	<p>θ fractional coverage</p> <p>Q_0 maximum monolayer coverage capacities (mg/g)</p> <p>K Langmuir isotherm constant (dm³/mg)</p> <p>C_e equilibrium concentration (mg/L)</p>
Brunauer-Emmet-Teller (BET)		<p>Multilayer adsorption</p> <p>Every layer is in equilibrium with the surrounding environment</p> <p>Langmuir theory applicable for every layer</p> <p>Monolayer conditions at the plateau</p>	$\theta = \frac{q_s C_{BET} C_e}{(C_s - C_e)[1 + (C_{BET} - 1)(C_e/C_s)]}$	<p>θ fractional coverage</p> <p>q_s theoretical isotherm saturation capacity (mg/g)</p> <p>C_{BET} adsorption isotherm relating to the energy of surface interaction (L/mg)</p> <p>C_s adsorbate monolayer saturation concentration (mg/L)</p> <p>C_e equilibrium concentration (mg/L)</p>

Flory-Huggins		<p>Adsorption of binary mixture onto homogeneous surface</p> <p>Accounts for the role of solvent</p> <p>Admits the sorption of molecules different in size, included in the exponential term</p>	$\frac{\theta}{C_0} = K(1 - \theta)^{n_{FH}}$	<p>θ fractional coverage</p> <p>C_0 adsorbate initial concentration (mg/L)</p> <p>K Flory-Huggins isotherm equilibrium constant (L/g)</p> <p>n_{FH} Flory-Huggins isotherm model exponent</p>
Freundlich		<p>Empirical description</p> <p>Heterogeneous surfaces</p> <p>Adsorption proportionality exponent changes with pressure (concentration)</p>	$\theta = K C_e^{1/n}$	<p>θ fractional coverage</p> <p>K Freundlich isotherm constant (mg/g) (dm³/g)ⁿ related to adsorption capacity</p> <p>C_e equilibrium concentration (mg/L)</p> <p>n adsorption intensity</p>
Hill		<p>Adsorption is a positive, negative or non-cooperative phenomenon.</p> <p>Vicinity adsorbate influences the further adsorption.</p>	$\theta = \frac{q_{sH} C_e^{n_H}}{K + C_e^{n_H}}$	<p>θ fractional coverage</p> <p>q_{sH} Hill isotherm maximum uptake saturation (mg/L)</p> <p>C_e equilibrium concentration (mg/L)</p> <p>n_H Hill cooperativity coefficient of the binding interaction</p> <p>K Hill constant</p>

5. SERS substrates

This thesis is about the application of SERS technology to the bioanalytical field, and in particular to biofluids. To this aim, we decided to develop and use simple but reliable devices for the label-free detection of biomolecules, aiming to push their application towards clinics.

5.1 Background

Although the main goal of this thesis was not on the development of nanostructured metal surfaces, but rather on testing available structures for bioanalytical applications with SERS, substrates played a central role, and have been carefully considered and studied. The choice of the SERS substrates always depends on the final application. In the plethora of possible solutions introduced in § 2, the key aspects to be defined are:

1. type of metal,
2. interface chemistry,
3. fabrication method,
4. physical phase (either colloidal or solid).

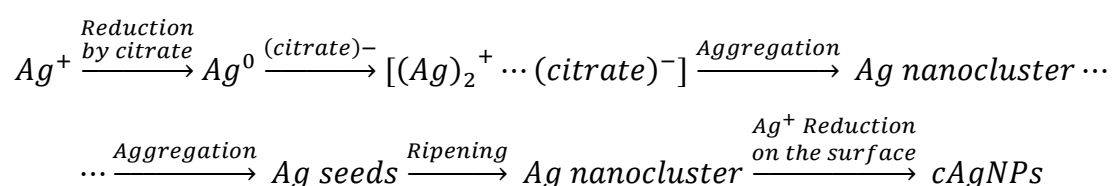
In the present case, we pursued additional desirable characteristics, namely

5. ease of fabrication,
6. limited costs,
7. repeatability and stability over time (shelf-life)

The aim was to test a substrate obtained with a simple NPs fabrication bottom-up strategy with complex matrices for both qualitative and semi-quantitative analysis. In particular, the citrate-reduced silver nanoparticles have been used both in colloidal form and aggregated on a rough porous surface, i.e., the cellulose fiber network of Whatman filter paper, to be used as a solid support. These two physical phases address different needs for different applications, whilst sharing the chemical nature of the nanoparticles. In this chapter, the protocol for the synthesis of the citrate reduced silver nanoparticles (cAgNPs) and two different protocols for the preparation of the paper-based SERS substrates are reported together with their characterization. The choice of silver as metal derives from its known good performance with biofluids in terms of SERS response reported by several authors [24,36,110]. In spite of Ag

greater chemical reactivity, which make Ag substrates more prone to contamination with respect to Au, this metal is known to yield substrates with higher enhancement factors [14,52]. The Lee-Meisel synthesis uses sodium citrate both as reducing and capping agent [111].

The Lee-Meisel protocol is widely known, used and characterized since its publication. It is based on the reduction of silver ions in solution through citrate salt as reducing agent, given its large electropositive reduction potential in water ($\text{Ag}^+ \rightarrow \text{Ag}^0$, $E_0=+0.799 \text{ V}$). Citrate both reduces the Ag^+ ions to its metallic form and stabilize the growing nanoparticles through electrostatic repulsion:



The size and the shape of the resulting NPs depends on several parameters: the stoichiometry of the reaction, the boiling time, the speed of stirring, as found by Pillai et al [112]. The citrate ions, together with the positively charged silver ions, form a double electric layer on the NP surface, which shields the van der Waals attractive forces experienced by the bare NPs. The repulsive Coulombian forces between citrate ions on the metal surface work as an electrostatic stabilization of the colloid, hampering aggregation further NPs aggregation. To overcome this electrostatic barrier, it is possible to increase the ionic strength of the dispersion medium or displace the citrate ions with neutral ligands/analytes which display affinity for the metal. In these ways, aggregation is induced: this is the key for the SERS enhancement to occur, due to the hot-spots formation in the gap between NPs.

The reasons behind the use of paper as solid support for many kinds of sensors has been already introduced in § 2. Being very inexpensive, easy to handle and compatible with aqueous samples, hence with bioanalytical applications, it results a winning choice. Moreover, the porous surface adds roughness to the aggregate distribution, improving the hot-spots formations.

The fabrication of the paper-based solid substrates finds its origin in a previous work by Dalla Marta and co-workers ([51], <http://hdl.handle.net/11368/2742099>), who developed a simple strategy of dip-coating nanoparticles deposition on paper substrate. For all the technical details, the reader is addressed to the correspondent publication. Moreover, a second protocol inspired by [92] revealed a good performance in terms of time of substrates preparation and overall spectral intensity.

One last but relevant comment regards the combination of the nanostructured substrates and the portable Raman instrumentation (§ 2) used throughout all the SERS measurements included in this PhD thesis. This coupling allows to optimize the

fabrication of a sensing method aiming at a future realistic application of SERS by means of affordable, manageable and portable devices.

5.2 Materials and Protocols

For the list of the reagents, used in the following protocols please refer to Appendix 1.

Warning: Each glassware element must be accurately washed with No-Chromix® solution and Aqua Regia, in this order. After each step, rinse thoroughly with MilliQ water.

5.2.1 Citrate-reduced silver nanoparticles:

The colloidal citrate-reduced silver nanoparticles (cAg-colloid) have been synthesized according to Lee and Meisel [111]. Briefly, 10 ml of 1.1% sodium citrate tribasic solution are added dropwise to 500 mL of boiling silver nitrate solution (90 mg AgNO₃ + 500 mL MilliQ water) in a two-necks flask connected to a refrigerator under vigorous stirring. The solution is kept boiling under stirring for 60 min at dark. The color of the solution slowly turns from transparent-uncolored to opaque-greenish. The colloidal solution can be stored in dark at RT and are stable for at least 6-8 months.

Some warning details: attention must be paid to some environmental aspects, like the room temperature and humidity and the glassware cleaning procedure (performed with NoChromix®, aqua regia and thorough rinse). Moreover, the stirring speed and the injection rate must be regular and regulated.

5.2.2 Protocol #1: paper-based Ag-solid substrates

This protocol has been taken from [51] and adapted.

The nanoparticles obtained with the previous synthesis are concentrated 10 times in volume with Ultra Centrifuge (60 min. x 45000 rpm). Contemporary, 1 cm x 1 cm filter paper (2 μm average porosity) squares are placed in well-wise in a 24 multi-well plates. 3 mL of the cAg-colloid are put inside each well and piped together with 62 μL of sodium citrate tribasic 1 M. The suspension immediately turns color from dark green to dark grey: the color shift is symptomatic for the aggregation process in progress induced by the addition of citrate ions. The multi-well has to be kept in dark for 7 days. After this period, aggregates coated the paper surface by precipitating on it; the supernatant has to be carefully removed without touching the delicate substrate in order to avoid any NPs turbulence at this stage, next, the paper-based substrates are allowed to dry. It is preferable to keep the freshly prepared substrates exposed to air at RT for a constant number of hours, in order to limit the oxidative

process on the nanoparticles surface. When dried, the cAg-paper substrates can be stocked immersed in MilliQ water in a Petri dish or in a multi-well. They will be stable for months. The drying step makes the substrates more stable, so that once they are re-immersed again in aqueous solutions the NPs do not detach from the paper support. With respect to the original procedure [51], we simplified the protocol introducing disposable multi-well plates instead of reusable glass vials, reducing time and the use of acids employed in the glassware cleaning procedure. Moreover, the simple addition of sodium citrate 1M instead of weighting the solid salt for each well allow faster preparation and improved repeatability of the support. These two passages required at least 2-3 hours for each synthesis batch with the previous protocol, now reduced to maximum 10 minutes.

5.2.3 Protocol #2: paper-based Ag-solid substrates

This protocol has been taken from [92] and adapted.

The nanoparticles obtained with the Lee-Meisel synthesis are used to prepare the paper-based substrates at the original concentration: no centrifugation is required. 1 cm x 1 cm filter paper (2 μm average porosity) are pretreated with a NaCl 1M solution for 20 minutes to allow a homogenous imbibition of paper. After this period, paper squares are let dry. This step allows the dispersion of Cl⁻ ions across the paper support. Then, the paper squares are put into the 24 multi-well plate together with 1.5 mL of cAg-colloids. The added chloride ions act as aggregating agent directly on the paper surface, locally changing the ionic strength of the suspension. After 24h the supernatant can be removed, and the cAg-paper substrates let dry off for a constant number of hours before stocking them in MilliQ water in a Petri dish or a multi-well. The substrates are stable over weeks. Compared to the original version of the protocol [92], we highlighted some improvement in the intra-batch repeatability measured through the absolute intensity of the spectra of some references compounds by changing the NaCl : NPs volume ratio.

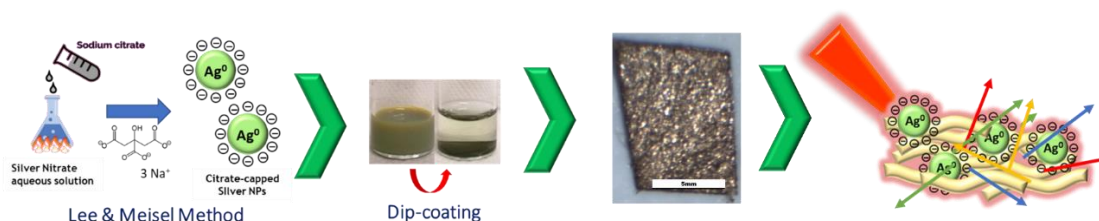


Figure 5.1 Sketch of the generic cAg paper-based solid substrates fabrication protocol.

There are multiple differences between the two protocols for the fabrication of the cAg-paper substrates, as summarized in Table 5.1.

	Protocol #1 cAg-paper	Protocol #2 cAg-paper
Centrifugation	Yes (60 minutes)	No
Volume required	3 mL (cAg 10x)	1.5 mL (cAg 1x)
Stabilization time	7 days	1 day
Shelf-life	Months	Weeks

Table 5.1 Pros and Cons of the two protocols for the cAg-paper substrates fabrication.

5.3 Substrates characterization

The SERS response is strictly dependent on size, shape and aggregation state of the cAg nanoparticles. Hence, several characterization procedures are required. The silver colloidal dispersions have been characterized in size, shape and surface charge by means of UV-Visible Spectroscopy, Dynamic Light Scattering (DLS), Z-Potential, Transmission Electron Microscopy (TEM). The paper-based silver substrates surface has been characterized with Scanning Electron Microscopy (SEM) and SERS.

In particular, UV-Visible spectra have been collected with Cary 60 UV-Vis, Agilent Technologies. The samples were diluted 10 times in MilliQ water in order to avoid the detector saturation and placed in PMMA cuvettes. Data were background corrected and reported as average of three replica. The UV-Vis measurements allow to obtain the extinction band of the surface plasmon of the colloids, which gives information on the size and the polydispersity of the NPs. All the batches used for the SERS measurements reported in this thesis displayed a maximum of the extinction peak at (410 ± 5) nm (Figure 5.2).

For the TEM images, cAg-colloids were diluted 1:1 in volume, deposit on TEM grid and let dry. The samples were characterized in terms of size and shape using the TEM Philips EM 208 at the Electron Microscopy Centre of the University of Trieste. The Lee-Meisel synthesis provides polydisperse NPs, with diameters ranging between 30-80 nm.

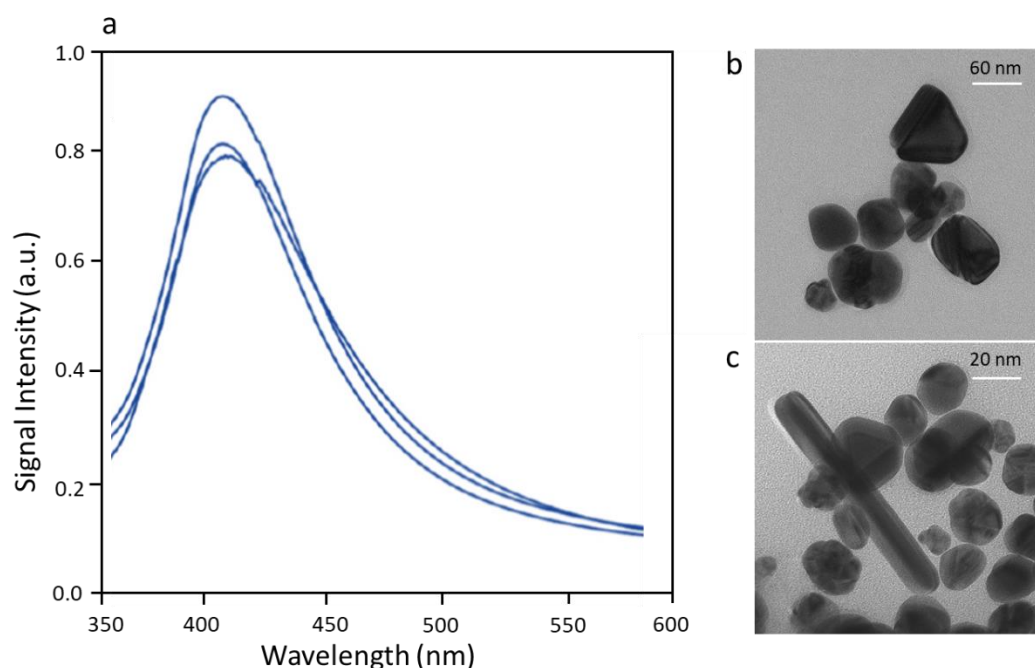


Figure 5.2 (a) UV-Visible characterization of a selection of cAg colloids. (b, c) report two TEM images at different scale of the cAg colloids. NPs are different in size and shape and this accounts for the broad extinction peak observed at the UV-Visible spectrum.

Dynamic Light Scattering is able to provide the hydrodynamic diameter of the NPs in colloidal form. Measurements have been performed with the Malvern Zetasizer Nano Z and the NPs diluted 10 times beforehand, resulting in a dispersion of sizes with maximum at 60 nm. With the same instrument, the Z-potential has been detected. Z-potential gives an estimation of the surface charge at the first ionic shell. The cAgNPs displayed a negative shell of -39.1 mV: a value large enough to induce electrostatic repulsion and to avoid aggregation at the synthesis concentration. Although TEM and DLS outcome cannot be directly compared in terms of measured size, as the physical principles behind the two characterizations are different, the two results were coherent.

The solid substrates surface has been investigated by means of Scanning Electron Microscopy. Specimens were mounted on aluminum stubs covered with two sides conductive carbon adhesive tape and the samples were sputtered with gold (Sputter Coater K550X, Emitech, Quorum Technologies Ltd, UK). Next the samples were immediately analyzed (Quanta250 SEM, FEI, Oregon, USA) operated in secondary electron detection mode with 30kV accelerating voltage. The working distance was adjusted in order to obtain the suitable magnification. The difference between the cAg-paper protocol #1 and protocol #2 is evident in Figure 5.3. The long dip-coating procedure and the high NPs concentration used in the first protocol lead to the high-density coverage of the cellulose surface, in accordance with [113]. However, being paper naturally inhomogeneous, the thick NPs layer can be absent or altered in some

region. This event may corrupt the SERS performance of the substrate in terms of signal repeatability. On the other hand, the second protocol leads to less abundant NPs on the surface, as suspected, but still the distribution of the aggregates is more homogeneous.

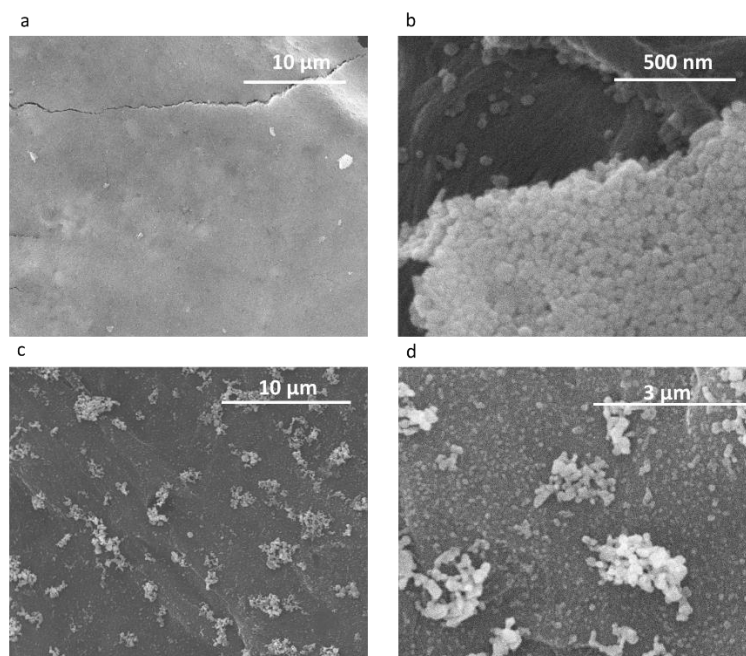


Figure 5.3 SEM images for the cAg-paper (a,b) protocol#1 and (c,d) protocol #2.

The evaluation of the SERS performance for the solid substrates are reported in the next paragraph.

5.3.1 SERS characterization

To evaluate the reliability of the two protocols in terms of intra and inter batch variability, SERS measurements have been performed using adenine as reference analyte. Besides being an important metabolite and an object of study in this thesis (see § 6), adenine gives an intense and well-defined SERS spectrum as a consequence of its high affinity for Ag surfaces: it is not being light or temperature sensitive, it has low-toxicity and it is inexpensive. All these characteristics make adenine a good candidate as a reference analyte. The use of a reference allows a direct comparison between different substrates, so to estimate how the batch synthesis and the paper-based substrates may affect the intensity and area of the one of the main peaks. Briefly, adenine was dissolved in PBS (see § 6 for further details on this kind of samples preparation) at the final concentration of 10 μM. The substrates were immersed in the adenine solution for 5 minutes, then rapidly soaked in MilliQ water and dried in air at RT. Next, the dried substrates are placed on a microscope glass slide and spectra were collected. The procedure has been replied for 5 batches with 10 spectra collected for each case (Figure 5.4).

The instrumental apparatus used has been a i-Raman Plus portable system (BWS465-785S) connected to a compatible Raman video microscope (BAC151B) and connected with the BWSpec software (version 4.03_23_c), by B&W Tek (Newark, DE). Excitation was obtained with a CleanLaze 785 nm laser with an output power of about 500 mW. Laser light is delivered to the sample and collected via an optical fiber probe. The Raman spectrometer uses a quantum efficiency CCD array detector with a wide spectral coverage ($65\text{-}4200\text{ cm}^{-1}$) and a spectral resolution of 2.4 cm^{-1} . Spectra collection used a 10 s CCD exposure for a single accumulation with a laser power at the sample of 10% (138 mW).

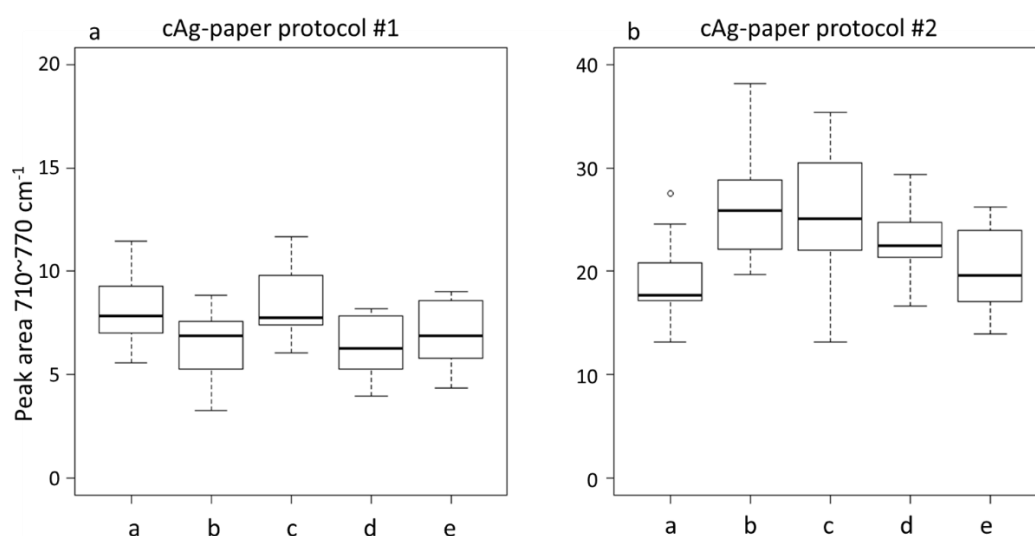


Figure 5.4 Ring breathing mode band area trend for 5 batches of Ag-paper substrates prepared according to (a) protocol #1 and (b) 5 to protocol #2.

The relative standard deviations, calculated as percentile ratio between the standard deviation and the mean for the single batch, range between 16-21 % for the protocol #1 case, and is lowered between 18-23% for the protocol #2. The outcoming average area and relative standard deviations are almost comparable. Hence, the reasons behind the choice of one or the other for a specific application is based on the better results in terms of detection sensitivity and signal-to-noise ratio for the sample under examination. As a note, the protocol #2 reports higher peak area values and absolute intensities too, in spite of a lower density distribution of the hot-spots as observed in the SEM images. A possible explanation may depend on the homogeneity of the aggregate distribution: not only the number of aggregates matters, but also their distribution within the focal volume on the incident laser. However, to the best of our knowledge these results are appreciable with respect to protocols for solid substrates found in literature [51], considering the inter-batch repeatability data. In the attempt to further optimize a protocol to overcome this issue, we tried the internal standard route.

5.3.2 The internal standard approach

Provided that signal repeatability is often an issue and that previous data revealed relative standard deviation around 20%, often not enough for quantitative determinations, we tried to identify a strategy for the use of internal standards. By definition, an internal standard (IS) is a substance different from those present within the specimen, and able to give an instrumental signal clearly distinguishable from the signals of the other analytes. It is added to the sample and to the blank in fixed concentration and its role is to correct the instrumental response or the sample preparation to reduce the error in the quantification of the analyte. This compound can then be used for calibration by plotting the ratio of the analyte signal to the internal standard signal as a function of the analyte concentration of the standards. This is done to correct for the loss of analyte during sample preparation or sensor inefficiency.

In the present case, the required characteristics of the internal standard are:

- i. ability to provide SERS signal
- ii. ability to form covalent bond with the substrate
- iii. no alteration of the adsorption process of the other specimens on the substrate
- iv. no alteration of the IS signal along with the specimen concentration changes.

Accordingly, three different class of internal standard have been chosen and tested at several concentration in presence of other reference analytes: (a) variously substitute mercapto-benzene molecules (thiophenol, 4-nitrothiophenol, 4-thiocresol, 4-mercaptobenzonitrile), (b) sodium sulphite and sodium tiosulphate salts, (c) Cadmium Sulfide nanoparticles, (d) purines isotopologues.

Briefly, none of these have been able to respect all the requisites reported above. Except for the third case, in which the signal of the CdS was not detected in the used range of concentration, the first two cases reported a same issue. In particular, the effect of the crescent concentration of the analytes affected the intensity of the standards peaks, thus preventing any possibility of calibration. All of these showed intense SERS spectra also in micromolar concentration, but most of the peaks correspond to bands of the specimens. Only the thiobenzonitrile showed a peak at $\sim 2200\text{ cm}^{-1}$ (CN stretching), far from the considered samples fingerprints. Nevertheless, the intensity of this peak was short-lived when the substrate with IS was exposed to air at room temperature.

With the isotopologues the aim was to observe a shift in the Raman shift of the correspondent non-isotopic form [4]. In principle, the presence of isotopic atoms in the molecule would affect the force constants for the vibration modes of the involved bounds, with respect to one of the analogue non-isotopically enriched molecules. Indeed, the reduced mass that appears in the k constant formula changes, according

to Eq. 2.1, leading to a consequent shift in the vibrational frequency and, hence, in the Raman shift. The entity of the shift depends upon the k value, and its detection on the instrumental features (i. e., the position of the monochromator slides). The aim was to spike the analyte solution with its isotopologue at fixed concentration and let them adsorb on the SERS, in order to have the isotopologue-signal as an internal standard. In principle, the chemical similarity to the analyte should not interfere with the subsequent adsorption kinetics and orientation of the specimen. Despite this, the “foreign” molecule has revealed to be still considered as an interferent and a competitor with respect to the adsorption kinetic, frustrating its “internal standard-like” purpose.

The bottom-up approach for the chemical synthesis of naked nanoparticles is not always a straightforward process. It is not improbable to face some reproducibility issues, especially in terms of average size, polydispersity, shape and, last but not least, chemical capping. All of these parameters are commonly controlled by a proper good synthesis practice: the temperature and the relative humidity of the room should be constant, the glassware properly cleaned, the reagents stored in anhydrous environment.

The synthesis can be a simple but delicate process, and every change in the protocol and reactants may affect the product. The main outcome of a bad synthesis in spectroscopic application is the lack of repeatability of the SERS signal, up to the appearance of unavoidable background peaks due to the presence of contaminants on the nanoparticles surface.

When struggling with the research of the faulty parameter, just think that the easier answer is often the correct one: water.

A proper purification system (physical, chemical and biological) must be provided in order to avoid the presence of organic contaminants or incorrect pH and conductivity values. Grade 1 water is recommended.

The sooner you control it, the sooner you will avoid repeatability issues.

6 SERS spectra of blood fractions

Liquid biopsy is a gold mine for diagnostic purposes, being minimally invasive and rich in information. SERS is able to open a window and observe some of these aspects and this Chapter means to provide an overview about the kind of spectral data than can be obtained from blood and its constituents, under the chosen experimental conditions.

6.1 Background

As the attention for the analysis of biofluids through label-free SERS arises in the academic and technologic fields, it is increasingly relevant to define what SERS can detect in a liquid biopsy and how to optimize the performance. In other words, sample preparation and data acquisition protocols account for a reliable and robust application in clinic.

In this Chapter, the main characters are blood and its fractions, and how their SERS spectra can be collected and interpreted. Blood tests are routinely used for qualitative and quantitative determination of the health status, as well as for the monitoring of pathologies and of efficacy of therapies. Obviously, efficient and robust devices are required, but still, devices based on optical technologies are not widespread and used to their fullest potential, as one might expect. For instance, the study of the Raman and SERS spectra of blood components can spread over a number of applications, from the identification of peculiar pathological fingerprint [10], to the target drug monitoring [86], to the nanotoxicology field and outside clinics in forensic science [114]. The peculiar features of SERS allow to detect molecules at low concentrations even in very complex systems, as affinity for the metal NPs determine the final spectrum profile. Thus, in chemically complex systems metal NPs can act as a signal “filter”, leading to a significant simplification. For instance, Premasiri (2012) emphasizes how the comparison between the SERS and the non-SERS Raman spectra of the same blood sample can reveal differences all over the spectral range [115]: mainly small metabolites on one hand, hemoglobin and other proteins on the other. This is not surprising, as the metal nanostructure plays an “active” role, enhancing the scattering of the adsorbates only. The other side of the coin is that band assignment can be tricky due to the plethora of components in biofluids. To date, band assignment of the blood spectrum is usually performed through comparisons with pure compounds spectra, although the mission is not an easy task.

Thus, a systematic label-free SERS analysis on blood and its constituents has not been completed yet.

The first Raman (and resonant Raman) investigation on blood constituents, like the heme group, dates back to the middle 70s with Abe, who first attempted bands assignments studying the difference in the spin, coordination and oxygenation state of the tetrapyrrole ring. This study has been confirmed and extended by several authors with both Raman and resonant Raman at various laser sources to unravel the structure and dynamics hemoglobin and other metalloprotein and the porphyrin [114–118]. Literature dedicated to SERS on blood is growing. Premasiri (2013) reported the Raman and SERS spectra of plasma, whole blood and red blood cells on gold surfaces with a 785 nm red laser and the ageing effect on blood samples on the SERS spectra [115]. Recent SERS studies performed on hydroxylamine- and citrate-reduced silver colloids (source 785 nm) revealed that the spectra of serum are dominated by purine metabolites, especially adenine, hypoxanthine, uric acid and reduced glutathione [30,31,119], whose inter-individual variation could represent relevant features to be investigated for diagnostic purposes.

Short laser wavelengths (i.e., 400-530 nm) are often used in Raman and SERS studies of biofluids, although they can match the resonance frequency of hemoglobin and carotenoids: these dominate the resulting spectra that are more likely to be resonant Raman than SERS and thus limit the possible metabolomic-like applications of this spectroscopy [36,51]. For example, Brazhe (2009, 2013) investigated *in vivo* erythrocytes with Raman and SERS on Ag NPs (excitation with 532 nm laser line) to characterize the inner membrane-bound hemoglobin oxidation state [120]. Casella and co-workers (2011) extended to the recognition of hemoglobin and carotenoids signature in whole blood with Raman and SERS through two excitation sources (532 nm, 785 nm), namely in resonance and off-resonance conditions. Thus, the evaluation of the SERS features of the blood fractions starts from the choice of the wavelength source. For this reason, all the Raman and SERS measurements reported in this PhD project used the near infrared 785 nm as laser source, non-resonant with the electronic transitions of porphyrins, bilirubin or carotenoids, as suggested by literature. In fact, previous studies demonstrated 785 nm to be the excitation of choice for biofluids analyses in terms of spectral information, especially when used together with citrate-reduced silver NPs as substrates [10,30,114]. Overall, the influence of blood proteins on the SERS spectrum is not yet clarified, as the protein corona formation around NPs in colloids or on the solid substrates could affect the detection of small metabolites, possibly hindering the enhancement of the scattered signal. Thinking about a realistic future application in clinic, this could be a crucial point in the setting-up of sample preparation procedures: is the protein removal a necessary step?

Our effort is to contribute to pushing the boundaries of the field through a SERS characterization of human blood and its fractions under different experimental conditions, with the implicit aim of providing an optimized protocol for the applications reported in the next chapters. To this end, we are going to evaluate: (i) the comparison between Raman and SERS spectra of blood fractions on both citrate-

reduced silver colloids and paper-based (solid) substrates, (ii) the effect of the sample-to-colloidal NPs ratio and (iii) the effect of sample dilution and protein removal (by filtration) compared to untreated samples. All these data have been compared to the correspondent Raman and SERS existing literature results. Indeed, the effect of proteins removal from biofluids on the metabolomic profile is not often addressed in the frame of Raman and SERS spectroscopy [30], since proteins identification and quantification are usually the focus of the research. The question is if the SERS spectra of blood fractions are significantly altered by the presence or absence of proteins. Starting from the background knowledge developed in this research group, citrate-reduced silver NPs (cAg) will be used in the following measurements, both as colloids and deposited on paper according to an in-house developed protocol [30]. These NPs are stable, and their synthesis is simple, inexpensive and widely used, so they are taking the scene of the “SERS-in-clinic” stage, but still literature lacks a broad characterization of the spectra obtained with biofluids.

6.2 Materials and Methods

6.2.1 SERS substrate fabrication

Citrate-reduced silver nanoparticles have been synthesized according to Lee and Meisel [111], used both in colloidal form (cAg-colloid) and fixed on a paper-based substrate (cAg-paper). The solid substrates have been prepared according to the procedure #1 reported in § 5. For the list of reagents see Appendix 1; for the substrate fabrication protocol and characterization, please refer to § 5.

6.2.2 SERS instrumentation

The measurements have been performed in air at room temperature with a i-Raman Plus portable system (BWS465-785S) connected to a compatible Raman video microscope (BAC151B) and collected with the BWSpec software (version 4.03_23_c), by B&W Tek (Newark, DE). Excitation was obtained with a CleanLaze 785 nm laser with an output power of about 500 mW. Laser light is delivered to the sample and collected via an optical fiber probe. The Raman spectrometer uses a quantum efficiency CCD array detector with a wide spectral coverage (65-4200 cm^{-1}) and a spectral resolution of 2.4 cm^{-1} .

Spectra collection used a 10 s CCD exposure for a single accumulation with a laser power at the sample of 50% (180 mW) and 10% (138 mW) for colloidal and solid SERS substrates, respectively. Raman spectra have been collected with a 50% laser power, too. The spot diameter at the sample was of 105 μm , channeled through a 20x Olympus objective (N.A. 0.25, working distance 8.8 mm). All the samples were placed under the microscope on a standard microscope slide: CaF_2 for liquid samples, glass

for solid substrates. Paracetamol has been used as reference before and during every data collection session to account for eventual laser drifts.

6.2.3 Sample collection

Blood has been sampled from 3 healthy donors after informed consent (mean age at enrolment 34 years, 1 male, 2 females) from the Transfusion Center (Azienda Ospedaliera Universitaria, Trieste). Blood was obtained by venipuncture and processed within 1 hour. For each patient, blood was collected in BD Vacutainer® serum separation tubes and BD Vacutainer® EDTA spray coated tubes for plasma extraction. Blood fraction have been separated within two hours from the drawn and stored at -20 °C.

6.2.4 Sample preparation

Within 1 hour from the collection, blood tubes for serum separation were centrifuged at 800 g for 10 minutes at 4°C to separate serum from blood and placed in ice. Part of the serum aliquots have been subsequently filtered with 10 kDa Amicon Ultra 0.5 mL centrifugal filters (Merck, DE) at room temperature, 30 minutes at 14000 g. The other blood fractions were derived from the EDTA-sprayed blood tubes for plasma separation. One aliquot of the whole blood was stored and plasma, Peripheral Blood Mononuclear Cells (PBMCs) and Red Blood Cells (RBCs) were isolated from whole blood by centrifugation (40 minutes at 600g at 15° C) through a density gradient medium (Ficoll-Paque PLUS, Merck, DE) added to the blood tubes, producing a stratification of the components. The plasma, RBCs and PBMCs fractions were carefully harvested with a pipette in different aliquots. Aliquots of the whole fractions of blood and RBCs were diluted 1:1 with distilled water, while PBMCs with ratio 1:4, to induce cells lysis; half of them was filtered (10 kDa Amicon Ultra 0.5 mL centrifugal filters) at room temperature, 30 minutes at 14000 g. Part of the plasma was only filtered with the same procedure. All the samples were stored at -80 °C and thawed immediately before spectra collection.

6.2.5 Spectra collection

For the Raman measurements, 5 µL of the samples have been placed with a micropipette on a CaF₂ slide and the spectra were immediately collected focusing the laser on the top of the drop.

For the SERS measurements on colloids and solid substrates, different procedures have been followed. The cAg-colloids have been mixed with biofluids at several sample-to-NPs volume ratio as reported in Table 6.1 for a total volume of 10 µL and placed on CaF₂ slide with a micropipette. Spectra have been collected on the drop after 5 minutes in order to allow a proper NPs aggregation. This delay has been established to optimize the signal to noise ratio (data not shown). For the cAg-paper-based solid substrates, 5 µL of sample were dropped on the surface and let dry for about 20 minutes. For pigmented samples (i.e., whole blood), the substrate surface was gently

washed with MilliQ water after 5 minutes of incubation: the metabolites adsorption on the NPs was allowed, preventing the risk of laser photodamage or burn. After drying, the paper substrates were placed on a glass microscope slide and spectra were collected at room temperature (25 °C). Each measurement has been run at least in triplicate. An overview of the samples and measurement conditions are reported in Table 6.2 and in Figure 6.1.

Volumetric ratio									
$\mu\text{L blood} : \mu\text{L cAg}$	1:9	2:8	3:7	4:6	5:5	6:4	7:3	8:2	9:1
Label	1:9Ag	1:4Ag	3:7Ag	2:3Ag	1:1Ag	3:2Ag	7:3Ag	4:1Ag	9:1Ag

Table 6.1 List of the volumetric ratio used to prepare the drop for the SERS analysis on Ag colloids. The Label row indicates how the correspondent samples will be named hereafter.

		Whole		Lysate	
		Unfiltered	Filtered	Unfiltered	Filtered
Cellular fraction	Blood	● ■ R	NA	●	● ■
	RBC	● ■ R	NA	●	● ■
	PBMC	● ■ R	NA	●	● ■
Non-cellular fraction	Serum	● R	● ■	NA	NA
	Plasma	● R	● ■	NA	NA

Table 6.2 Distribution of samples, treatments, and used SERS substrates (■ = SERS@cAg-paper; ● = SERS@cAg-colloid; R = Raman; NA = not available).

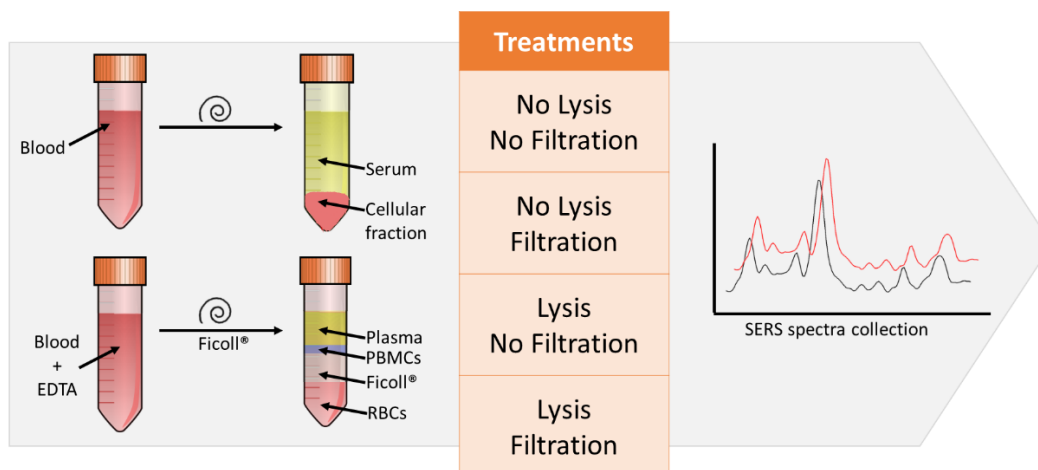


Figure 6.1 Sketch of the sample preparation. Each blood fraction undergoes different treatments according to Table 6.2

6.2.6 Data analysis

Spectra have been entirely processed in the R environment [121] using *hyperSpec* [122], *baseline* [123], *MALDIquant* [124] packages and other in-house developed scripts for spectra visualization.

The steps included: (i) Raman shift range selection, (ii) baseline correction (package *baseline*, method *als*, $\lambda = 6$), (iii) smoothing for noise reduction (data spacing = 3cm^{-1}), (iv) vector normalization.

The criteria for the baseline choice meant to avoid artifacts, and the *als* (asymmetric least squares) allows a correction by the 2nd derivative constrained weighted regression, with λ as constraining factor. The smoothing procedure returns evenly spaced spectra in the selected range, without the risk of overfitting. The smoothing is useful to reduce the signal-to-noise ratio through the *loess* (locally estimated scatterplot smoothing) function. It interpolates each spectrum onto a new x-axis with a local linear fitting by weighted least squares of a polynomial surface on neighbor segments, and the size of the neighborhood is controlled.

6.3 Results and Discussion

6.3.1 SERS and Raman of whole blood and blood constituents.

Raman and SERS normalized spectra of 5 fractions, i.e. i) whole blood, ii) RBCs, iii) PBMCs, iv) plasma and v) serum samples (whole and unfiltered) on Ag paper substrates are compared and reported stacked along the y-axis in Figure 6.2. Looking at the single component, the two techniques show different contributions and

Table 6.3 sums up the line assignments based on literature. Note that spectra vector normalization allows only qualitative description and delete the information on the absolute intensities of the single spectrum.

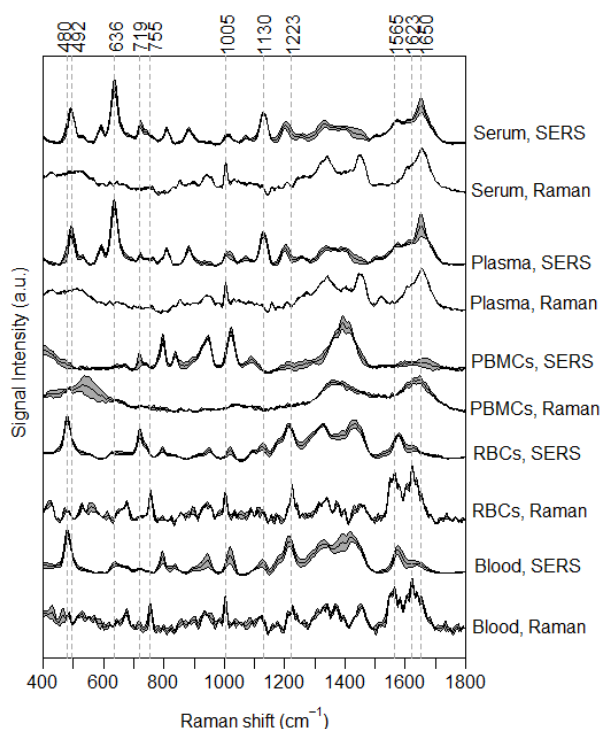


Figure 6.2 Raman and SERS@cAg-paper spectra of unfiltered blood components. Measurements have been acquired with the 785 nm laser; data are vector normalized and reported as mean \pm standard deviation of several replica.

The Raman spectra of whole blood and RBCs are similar and follow the spectral profile seen in [115,116,125,126], dominated by hemoglobin and heme-group vibrations. Heme shows porphyrin breathing at 755 cm^{-1} , pyrrole half-rings stretching at 1126 cm^{-1} and 1375 cm^{-1} , methine bridges stretching at 1580 cm^{-1} , whereas the others reported peaks account for other hemoglobin stretching modes which are sensitive to the distortion of the porphyrin that changes with the redox and spin state of Fe, the presence of ligands (O_2 , CO , NO) and the conformation of the surrounding metalloprotein [120]. Few peaks belong to non-porphyrin moiety, such as amide I (1650 cm^{-1}), phenylalanine stretching (Phe, 1003 cm^{-1}), tyrosine stretching (Tyr, 850 cm^{-1}) and the CH_2/CH_3 amino acid deformation modes (1450 cm^{-1}). All these Raman peaks of whole blood and RBCs are mainly attributable to the oxygenated hemoglobin, compared to the spectra reported in literature [115,127] and its oxygenation state can be arguably due to the exposition to ambient oxygen during the extraction and pre-analytic processing. Moreover, it cannot be excluded that the freezing processes may have disrupted the cellular membrane of the cell fractions, in both RBCs and

PBMCs, causing cytoplasmic hemoglobin to leak out. However, the assignment of some bands (i.e., 480 or 492 cm^{-1}) is still missing.

As expected, Raman and the correspondent SERS spectra for whole blood and RBCs are not completely matching: SERS bands are broader, although more intense (absolute intensity, data not shown), and at different wavenumbers. Simply put, the SERS and Raman spectra are different because they originate from different sources: low-molecular weight adsorbed metabolites in SERS, major protein components in Raman. Moreover, the chosen excitation source, in off-resonance with respect to the porphyrin electronic transitions, makes the heme group contribution overlapped by other more intense bands. The main difference lies in the 725 cm^{-1} peak, that is way more intense in RBCs than in whole blood: we hypothesize that it may belong to purines. Purines are obviously present in whole blood too, but we can assume the presence of a sort of “matrix effect” which hampers their free diffusion or other molecules towards the SERS substrate. Besides, the region between 800 cm^{-1} and 1050 cm^{-1} belongs to the substrate background (see Figure A.3.2 in Appendix 3), the SERS band at 480 cm^{-1} appears in both the samples stronger than the Raman homologues. As a note, background bands are commonly classified as “anomalous” bands, namely spectral features that are not sample-dependent. Their presence is not unusual, and depends on the experimental set-up, as they can derive from various sources, i.e., contaminants, sample degradation, or artifacts like laser photodamage. The latter is common when working with non-colloidal substrates and induces amorphous carbon sp^2 stretching bands in the 1360 - 1560 cm^{-1} region. To avoid them, the set-up has to be optimized, i.e., reducing the incident laser power. Sample photodamage is infrequent with colloids, as the water percentage can efficiently dissipate heat [36,128].

PBMCs Raman spectra does not show any significant trend other than three very weak and extremely broad bands around 520, 1370, 1565 cm^{-1} , therefore not assignable. This result can be related to their low concentration or to the poor tendency to show SERS signals that come from the cellular membrane, assuming it to be intact. In the SERS spectra, only the metal enhanced bands of the citrate background appear (900-1050 cm^{-1}), and the cells are arguably still too diluted to provide appreciable spectra. PBMCs are a rich mixture of cells different in nature, but since their separated populations have not yet been analyzed through SERS, the vibrational profile of this blood fraction is still under investigation and requires further examinations. For these reasons, PBMCs spectra are not going to be further analyzed since the carried information is still poor and strongly protocol dependent. However, the excluded PBMCs spectra are reported in Appendix 2.

Raman* cm ⁻¹	SERS* cm ⁻¹	Tentative Assignment	Blood fraction**
430w		v ₂₁ δ(Fe-O-O)	A, B
480w		-	A, C, D
	492s	-	C, D
568w		v (Fe-O ₂)	B
	638	breathing ring uric acid (s)	C, D
676m		v ₇ , heme	A, B
720s	722s	breathing ring purines (m)	C, D
755s		v ₁₅ , heme breathing	A, B
	810w	-	C, D
	850w	Tyrosine	A, B
1003s	1003m	Phenylalanine	A, B, C, D
1125w		Protein C-N, C-C stretching	A, B
	1130m	v(C-N), uric acid (vs)	C, D
	1203m	-	C, D
1223s		v, δ (N-C-N), hemoglobin (m)	A, B
1375s		v ₄ , heme pyrrol half-ring	A, B
1450s		CH ₂ /CH ₃ Amino acid deformation	A, B
1565s		C=C, C-C, heme	A, B
	1574m	C-C, C-C-H, heme	A, B
1580s		Hemoglobin	A; B
1603vs		v ₁₀ , Hemoglobin	A; B
1623vs		v ₁₀ , Heme methine bridges	A, B
1650s	1650s	Amide I	A, B, C, D

Table 6.3 Position and assignment of bands in Raman and SERS spectra. Estimated precision ± 1 cm⁻¹. Data are from literature [36,114–116,127]. * (vs) very strong, (s) strong, (m) medium, (w) weak. ** (A) blood, (B) RBCs, (C) Plasma, (D) Serum.

Serum and plasma share almost the same profile in both Raman and SERS spectra, respectively. However, the Raman and SERS profiles of the same specimen are still completely different. In the Raman spectra, 1003 cm⁻¹ Phe is the only intense and sharp peak, with the purine broad band in the region between 1300 and 1500 cm⁻¹ and the protein contribution around 1635 cm⁻¹. The SERS spectra are intense and more reproducible than the other blood components, and the overall profile includes uric acid bands (638 cm⁻¹ and 1130 cm⁻¹). Notably, the typical purines peak around 730 cm⁻¹ does not appear. This may due to their low concentration in serum and plasma, donor-dependent, that can be retrieved by the surrounding proteins and/or

by the good practice that allowed a fast after-draw sample processing: it is known that a fast procedure allows to minimize the risk of purine metabolization with the high production of hypoxanthine that would alter the original sample and spectrum [115]. The intense peak at 492 cm^{-1} appears again but it is blue shifted with respect to the correspondent band in whole blood and RBCs.

To the best of our knowledge, this is the first non-resonant Raman and SERS complete characterization of all the blood fractions, in the frame of the chosen instrumental set-up. So far, the most remarkable result is that whole blood Raman spectra strictly relates to the RBCs spectra, hence to heme group and hemoglobin, and the SERS ones, obtained with our solid substrates, are informative respect to the metabolites present in the biofluid.

Unfiltered samples mixed with colloidal NPs did not show evident SERS spectra, although some significant signals have been detected mixing the sample with the 10 times concentrated colloid at room temperature. In Figure 6.3, the spectra of the filtered and unfiltered serum analyzed with silver solid substrates and colloids at two concentrations (1x and 10x) are shown.

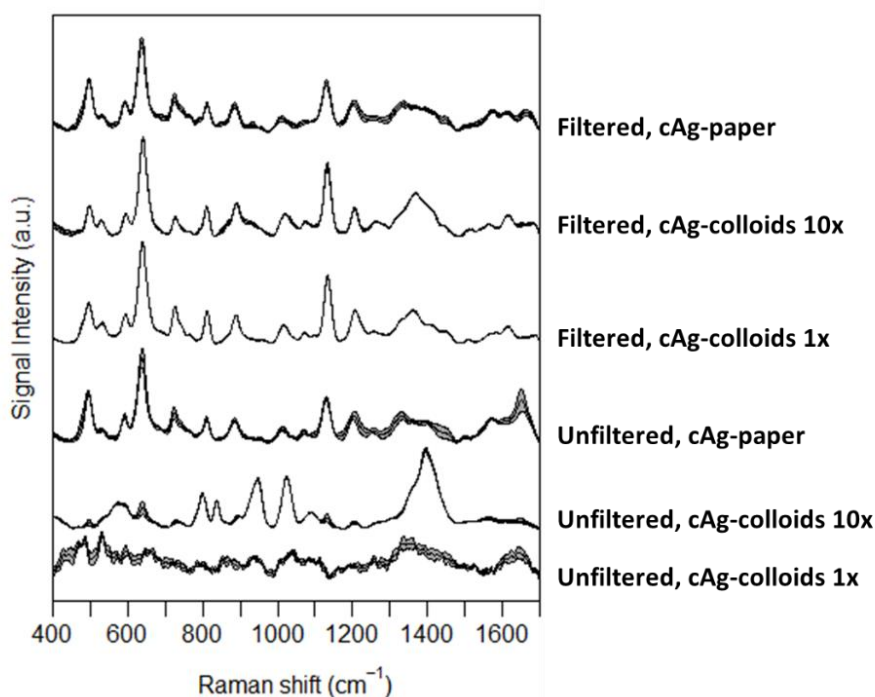


Figure 6.3 Effect of filtration and SERS substrate form and concentration. Measurements have been acquired with the 785 nm laser; data are vector-normalized and reported as mean \pm 1 standard deviation (shaded area) of several independent replicas, with cAg-paper = paper-based citrate-reduced silver substrates, cAg-colloids = citrate-reduced silver colloids.

For the sake of clarity, only one sample-to-NPs ratio (1:9 Ag ratio) is reported for the cAg-colloids. The filtered samples yield very similar spectra (upper part of the plot). Hence, the concentration of the cAg-colloids does not add any peculiar information to the spectra and is unnecessary. Conversely, the unfiltered samples (lower part of the plot) show different spectral profiles: the intensity for the cAg-colloids 1x case is too low and noisy, while the cAg-colloids 10x case shows some signal, but it is dominated by the intense citrate signal ($900 - 1100 \text{ cm}^{-1}$). If filtration allows metabolites to freely reach the NPs surface, in the unfiltered samples the formation of the so-called protein corona around NPs hampers their coupling and the hot-spots set up, which induce the enhancement of the scattering. However, NPs concentration induces partial preaggregations which are responsible for the background bands. Moreover, small metabolites may be still able to pass through this shell with a slower kinetics and to approach the metal surface. The SERS signal is then detectable, although with a reduced intensity due to the lower amount of NPs aggregations. It is worth noting that cAg-colloids 1x and cAg-paper reported the same normalized spectral profile, at the considered sample-to-colloid ratio. This suggests that the diffusion of the analytes from the bulk solution within the paper network toward the deposited metal nanoparticles mimics the diffusion from the bulk solution to the nanoparticles suspended in the colloid. As a final comment, unfiltered serum on cAg-colloids 1x (synthesis concentration) can give SERS spectra after 24h of incubation at room temperature (data not shown), but such a long sample preparation is considered impractical for the purposes of this thesis, as we focused on the optimization of faster protocols, suitable for point-of-care approaches. The solid substrate provides the typical spectra of serum, as the proteins do not alter the aggregation state of the already aggregated NPs. For all these reasons, mixtures of colloids and unfiltered samples are not going to be further used in this project, as they did not yield significant SERS signals unless after several hours of incubation.

6.3.2 SERS of biofluids: effect of the colloid/biofluid volumetric ratio

When colloids are used for SERS, a proper sample-to-NPs ratio has to be chosen since the relative intensities may change with the volume ratio. Considering the two most representative samples, the SERS spectra for the nine combinations of cAg colloids with lysed and filtered RBCs, and serum are reported in Figure . Indeed, RBCs and whole blood share a similar SERS pattern, and the same can be said for serum and plasma; PBMCs suffer of some limitations already discussed in the previous paragraph. The analogous experiments and data of whole blood, PBMCs and plasma are reported in Appendix 2. In particular, blood, RBCs and PBMCs were lysed beforehand with MilliQ water - not required for plasma and serum - and the protein fraction was filtered with a 10 kDa cut-off centrifugal filter. Overall, all the spectra share a similar pattern with purine regions at 722 cm^{-1} and between $1300-1450 \text{ cm}^{-1}$, uric acid at 638 cm^{-1} and 1130 cm^{-1} , and the aforementioned unassigned band at 485 cm^{-1} , here red shifted of 7 cm^{-1} with respect to the solid substrates reported in the previous paragraph. This frequency shift is relatively small and indicates that the

electronic structure of the molecules is not dramatically perturbed. It may be due to the different structure the substrates (liquid sample on cAg-colloids vs dried sample on cAg-paper substrate) and of the sample preparation. Of course, no features due to proteins are present in this case, due to the filtration step. The trend is similar for all the considered cases: the more the biofluid is diluted in the colloid, the more the SERS spectrum intensity increases and the signal-to-noise ratio is reduced, with barely no effect on the relative intensities of the overall profile of the spectra, with some exceptions.

RBCs spectra are almost superimposable in the whole concentration range. Brazhe (2012) found the same on erythrocytes mixed with hydroxylamine-reduced silver NPs with a 532 nm laser, proving that the shape of the peaks was stable over four ratios, with growing intensities for more diluted samples [125]. This effect may address to the favorable probability for a larger number of molecules to adsorb on the NPs surface: the larger the number of adsorbed compounds, the more intense the signal. Conversely, when the number of available adsorption sites on the metal surface is reduced with respect to the analytes (i.e., 9:1 Ag ratio), the number of aggregate and hot-spots is statistically lower for a same focal volume. The result is a lower signal enhancement.

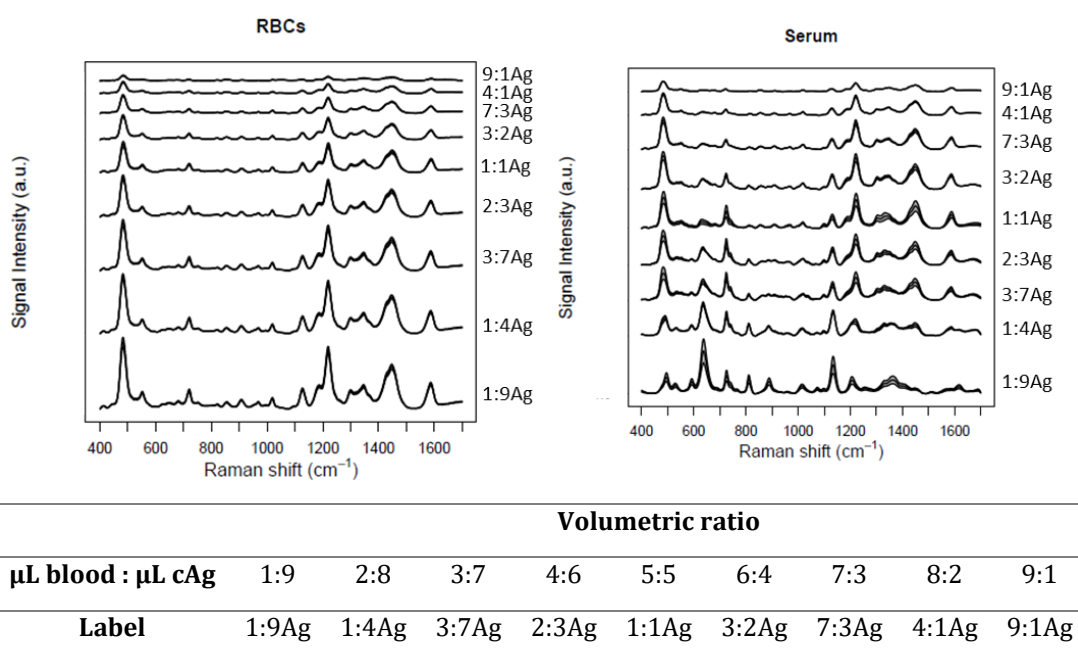


Figure 6.4 Effect of the cAg-colloids dilution on filtered RBCs and serum. Measurements have been acquired with the 785 nm laser; data are vector normalized and reported as mean \pm 1 standard deviation (shaded area) of several independent replicas. The y-labels replicates the effective ratio and Table 6.1 is reported again for a clear read.

The remarkable intensity of the peak at 485 cm^{-1} in all the five cases might suggest a charge transfer interaction between the unknown compound and the metal NP, typical of the thiol moieties. Indeed, several authors assign the band to a S-S vibrational mode, often hinting to the cysteine bridges in proteins (i.e., hemoglobin or lysosomal proteins, rich in disulfide bonds) [71,115,119,130]. However, our experiments on filtered biofluids clearly demonstrate that this cannot be true, as filtration removes the macromolecular fraction ($> 10\text{ kDa}$), but the 485 cm^{-1} band is still present. A possible explanation is that small peptides might have passed through the 10 kDa filter, or simply attribute it to other low-molecular weight compounds, still unknown. Whatever the origin of this band is, it always occurs together with bands at 1220 and 1586 cm^{-1} , which can thus be ascribed to a prominent but still unknown metabolite.

Serum samples show a peculiar behavior: the relative intensities of the coupled peaks at 485 and 1223 cm^{-1} on one hand, and at 638 and 1130 cm^{-1} on the other, undergo an opposite trend starting from the 1:4 Ag dilution upwards, with the more diluted case dominated by the purine peaks, which decrease in the higher ratio case in favor of the unknown compounds. A possible explanation may regard the competition between analytes in terms of concentration versus affinity. Our speculation addresses the unknown molecule to be more concentrated in biofluids than the purine and to be able to saturate the NPs even at high NPs concentration, hence to dominate the SERS spectra. On the contrary, purines have a higher affinity to the NPs although their concentration is poor, hence their contribution to the SERS signal prevails when they can adsorb on a larger number of metal sites. However, this is only a hypothesis. In our view, the key to explain this behavior lies in the identification of the unknown compound responsible for the 485 , 1220 and 1586 cm^{-1} : once its chemical structure is known, targeted experiments with the pure substance could shed some light on its competition with uric acid for the adsorption on Ag.

All these aspects are relevant and need to be unraveled, as the potential use of serum (and plasma) for clinic purposes requires a clearer description of the spectral trend and profile.

6.3.3 Effect of filtration and lysis on SERS of biofluids

In the superabundance of constituents of blood, three macroscopic classes can be roughly identified: small molecules (i.e. metabolites), macromolecules (proteins, DNA) and cells (PBMCs, RBCs and platelets). In their race for the NPs surface, the open question is if a preferential adsorption occurs and how we can recognize it. To this aim, we performed simple preprocessing steps able to induce changes in the sample composition or species concentration. The blood fractions underwent two kinds of procedures: lysis (for the cells case) and filtration in cross combination, so that four classes of processes were obtained. Samples were: non-lysed and unfiltered, non-lysed and filtered, lysed and unfiltered or lysed and filtered, as reported in Table 6.2 and in Figure 6.1. However, only two examples are shown for a clearer comparison,

as previously reported: RBCs and serum. Again, similar spectra can be observed for blood and plasma, respectively, whereas the spectra of PBMCs are flawed by the background due to the poor concentration. The excluded spectra are reported separately in Appendix 3, for completeness.

In Figure 6.5, the effect of lysis and filtration treatments compared to the untreated samples (not-lysed and unfiltered) on cAg-paper substrates. The cAg-colloids have been here set aside, since the effect of filtration has already been discussed. The band assignment is the same already described, with the unknown compound with an intense band at 485 cm^{-1} , the purine region at about 735 cm^{-1} and between $1300\text{-}1400\text{ cm}^{-1}$, the uric acid signature at 650 cm^{-1} and 1130 cm^{-1} , the amide I band a 1628 cm^{-1} and the Phe peak at 1002 cm^{-1} . The main differences can be addressed to the qualitative alteration of the relative intensities among these groups of bands. Filtration seems to not affect the serum spectra, and the only evidence is the intensity reduction of the amide I band (1650 cm^{-1}). On the contrary, treatments induce some alterations in the RBCs spectra. Lysis causes a slight increase of the average purines peak with respect to that of the unknown compound in unfiltered RBCs. If our hypothesis on the competitive binding of these two classes of molecules is true, lysis causes dilution of the sample and reduces the probability for the binding of the unknown compound in favor of the purines one. RBCs proteins are present on the metal surface, although less than in the serum case. Proteins in biofluids are able to bind other molecules (e.g., serum albumin). When filtration occurs, the main effect on the spectra regards the alteration of the intensity ratio between 735 cm^{-1} and 485 cm^{-1} peaks and is symptomatic of a different degree of interaction with the proteins. Filtration impoverishes the sample of everything bound to the proteins and increases the relative concentration of the remaining species.

The unfiltered and intact RBCs on cAg-paper spectra match what was observed by Drescher (2013) with the same protocol, but on colloidal cAg (laser source: 785 nm) [131]. Moreover, Genova (2017) observed that lysis of intact cells and the proteins removal do not heavily affect the overall SERS spectra and neither does the presence of organelles, membranes, stress grains or macromolecules in the unfiltered samples [119]. Indeed, in our case, non-lysed and lysed RBCs display similar spectra, but this might be due to the disruption the intact RBCs underwent in the freezing-thawing procedures during the sample preparation. Also, a partial lysis as a consequence of the interaction with the nanostructured metal surface cannot be excluded.

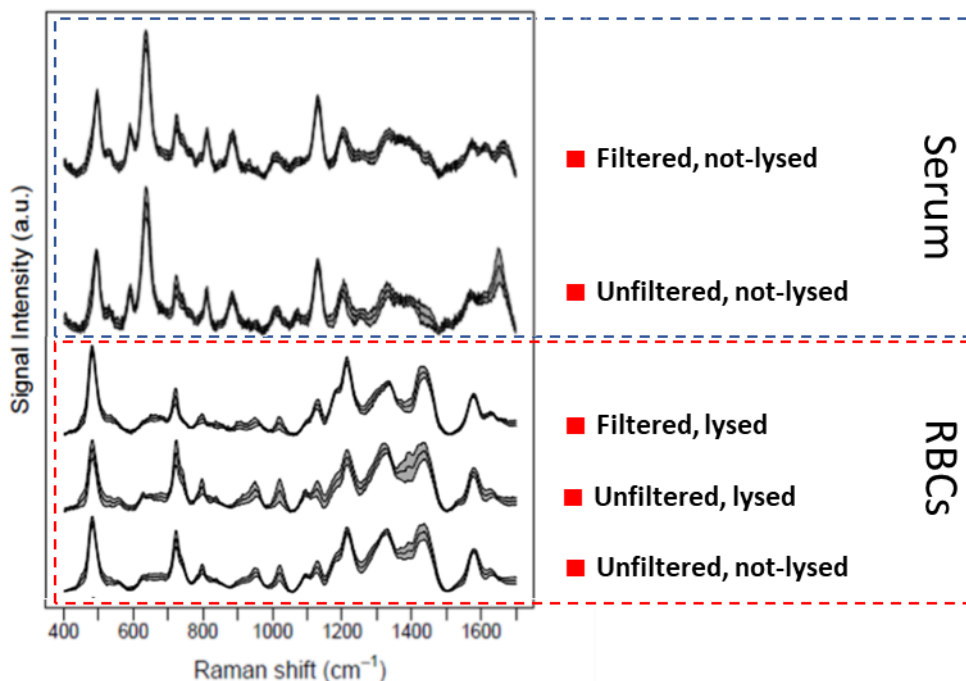


Figure 6.5 Effect of lysis and filtration. ■ = cAg-paper solid substrates. Measurements have been acquired with the 785 nm laser; data are vector-normalized and reported as mean \pm 1 standard deviation (shaded area) of several independent replicas.

In conclusion, the lysis and filtration steps do not affect that much the SERS spectra under the conditions chosen for these experiments, although they can alter the relative concentration of metabolites and their peaks intensities.

However, whole blood and intact RBCs revealed to be not perfectly suitable for SERS analysis on our solid paper-based substrates: they require additional washing steps before the measurements to remove the heme fraction, otherwise the red 785 nm laser would photodamage the sample also with low source power. For this reason, blood and RBCs on cAg-paper are not going to be further used in this project.

For the practical application of label-free SERS on liquid biopsies, the use of plasma and serum, both filtered or unfiltered, can easily overcome the background issue and their spectra have been demonstrated to be more sensitive to metabolic variation. Moreover, the choice between the developed cAg paper-based solid substrates or cAg-colloids is only ruled by convenience, often connected to the available volumes of sample, since the spectral features are almost identical.

6.4 Highlights:

- The use of Raman and SERS spectra (with cAg-colloids and cAg-paper) of whole blood and RBCs is not suggested for untargeted-metabolomics studies, since fewer metabolites are detected with respect to plasma or serum. Moreover, whole blood and RBCs are more easily subjected to photodamage.
- Plasma and serum SERS spectra are more similar and display bands due to metabolites such as purines and uric acid. The metabolic profile as detected by SERS can be altered by preanalytical procedures (i.e., long waiting before the fraction separation and filtration). The main outcome is an increased hypoxanthine levels due to the extracellular metabolism of purine: cellular fraction is not involved here, but filtration can stop the process, as the enzymatic fraction would be removed.
- Ratio: higher samples dilutions imply higher probability for the analytes to reach the metal surface and to be detected. The overall profile is not that affected, although some alteration in the relative intensities can be observed in plasma and serum. In general, 1:1 and 1:9 ratios provide the same pattern in whole blood and RBCs, except for the intensities. PBMCs signature is sample-preparation dependent and requires further investigations. For applicative purpose the ratio choice may depend on other factors, like the available amount of sample.
- Filtration: while it is essential to obtain SERS spectra from colloids, it remains an optional step for SERS on solid substrates. Proteins affect the spectra only to a limited extent, and the overall shape of the spectra does not vary. It is an additional step that can prolong the sample preparation protocol.

7 The Nanostructure-Biofluid interface: a model

The understanding of the boundary conditions and the mechanisms involved in the bioanalytical sensing are fundamental aspects, which need to be unraveled as well as the applicative ones. Unlike this approach seems to be a step back, it is actually a step forward in the study of the biofluids spectra, to further define the role of proteins in biofluids in the frame of SERS investigations. The complexity is reduced to a model system composed only by human serum albumin and three metabolites, known to commonly appear in the SERS spectra, as stated in § .6 From another perspective, proper SERS substrates are a tool for the analysis of the so-called protein and non-protein corona.

7.1 Background

Nanoparticles are playing and will play an important role in the modern and future society, considering their widespread application all over diversified fields such as medicine, cosmetics, industry, and the impact they have on living organisms and on the environment.

Something happens when NPs get in touch with biological matrices. Protein corona (PC) is the classic name given to the protein layers spontaneously formed around nanoparticles, irrespective of their nature, when put in contact with a biological environment (e.g. biofluids, cytosol). The physicochemical properties of this assembly depend on the NPs, on the media composition and its evolution in time. In particular, the corona is called “hard” when part of the proteins remains on the NPs surface for a long time preventing the adsorption of other molecules. Otherwise, the corona is “soft” when the macromolecules on the NPs surface dynamically exchange with the surrounding medium. This can be a consequence of the evolution of the composition of the solution, or due to kinetics and thermodynamics driving forces, but little is known about this process in literature [132,133]. Anyways, research could benefit from PC for signaling when NPs are built for specific targets, but it may become a drawback if the NPs function is hampered by the PC. The latter is the case when SERS is implemented with colloidal metal nanoparticles. As far as SERS is concerned, the presence of proteins in biofluids and the formation of PC hinders NPs aggregation, limiting the hot-spots formation and the enhancement of the scattered light.

The introduction of paper-based solid SERS substrates helps to overcome the issue of the hampered nanoparticle aggregation, since in substrates obtained by a bottom-up approach NPs are pre-aggregated and immobilized on a solid support. Proteins, as well as other low molecular weight molecules, can adsorb on its surface and now their SERS signal can be detected, overcoming the lack of aggregation issue. In the frame of the label-free SERS analysis on biosystems, the spotlight shifts to the detection of small metabolites, since the SERS cross-section for proteins is usually low [134]. Much less, in fact, is known about the “non-protein corona”, i.e. the adsorbed layer formed by low-molecular weight metabolites. SERS spectra of biofluids are offering us an insight into this “non-protein” or “metabolic” corona, but the interplay between these metabolites and the protein corona is completely unexplored (Figure 7.1).

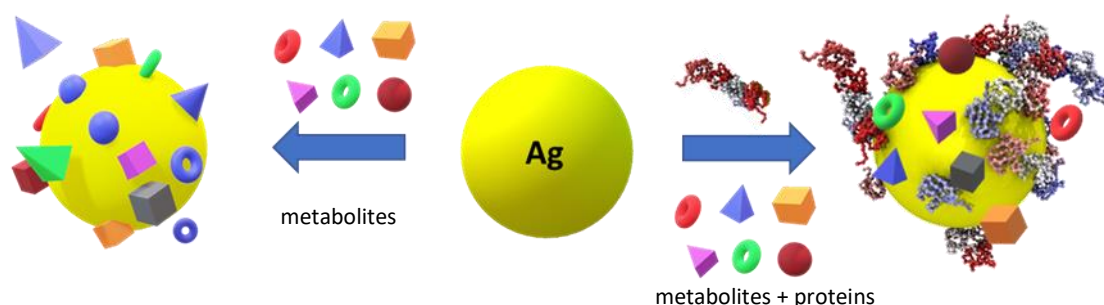


Figure 7.1 Sketch for the non-protein (left) and protein (right) corona.

The aim of this Chapter is to interpret the complexity of the biological matrix reducing it to a model system and to provide a systematic analysis on the competitive adsorption on nanostructured metal surfaces of small metabolites commonly observed in SERS spectra (e.g. adenine, hypoxanthine, uric acid). Moreover, we will try to examine how human serum albumin (HSA), one of the most abundant proteins in serum, can quantitatively affect the adsorption of such metabolites. Adenine, hypoxanthine and uric acid are purine metabolites and their presence within the SERS spectra has been discussed in § 6 and confirmed in literature [30,115]. They are poorly soluble in water and their concentration in blood range between 0.2 – 0.6 μM for adenine, 1-10 μM for hypoxanthine and 200 – 400 μM for uric acid [135]. These broad ranges derive from the huge variability among organisms, gender, age and pathological conditions.

All the measurements have been performed with the in-house developed solid SERS substrates, described in § 5, assuming to be able to identify concentration/signal relations. The choice of the substrate protocol accounts for the good spectroscopic performances in terms of signal-to-noise ratio for the whole concentration ranges.

Furthermore, the objectives of this work include: (i) analyzing the adsorption binding trend of low molecular weight biomolecules in the physiological concentration range

and above; (ii) verifying the effect of protein filtration on the SERS spectra on a mixture of the considered analytes in their physiological concentration; (iii) evaluating the diffusion of the small metabolites through the protein layer on the NPs and vice versa. All these goals are based on the univariate analysis of concentration-sensitive peaks, by means of SERS spectra on the used solid substrates, in an effort to perform quantitative determinations.

These data would be a step forward in the understanding of spectra of biological fluids and in the identification of a rationale for the binding on NPs phenomenon of both macromolecules and small ligands through SERS.

7.2 Materials and Methods

7.2.1 SERS substrate fabrication

The solid substrates have been prepared according to the procedure #2 reported in Chapter 5, starting from citrate-reduced silver NPs according to Lee and Meisel (cAg-colloids). For the list of reagents see Appendix 1; for the substrate fabrication protocol and characterization, please refer to § 5.

7.2.2 SERS instrumentation

The measurements have been performed in air at room temperature with a i-Raman Plus portable system (BWS465-785S) connected to a compatible Raman video microscope (BAC151B) and collected with the BWSpec software (version 4.03_23_c), by B&W Tek (Newark, DE). Excitation was obtained with a CleanLaze 785 nm laser with an output power of about 400 mW. Laser light is delivered to the sample and collected via an optical fiber probe. The Raman spectrometer uses a quantum efficiency CCD array detector with a wide spectral coverage ($65\text{-}4200\text{ cm}^{-1}$) and a spectral resolution of 2.4 cm^{-1} . Spectra collection used a 10 s CCD exposure for a single accumulation with a laser power at the sample of 138 mW (10%). This power level has been chosen in order to avoid samples and substrates photodamage. The spot diameter at the sample was of $105\text{ }\mu\text{m}$, channeled through a 20x Olympus objective (N.A. 0.25, working distance 8.8 mm). All the substrates were placed under the microscope on a standard glass microscope slide. Paracetamol has been used as reference before and during every data collection session to account for eventual laser drifts.

7.2.3 Sample preparation and spectra collection

Adenine, hypoxanthine and uric acid stock solutions 1 mM were prepared dissolving the powders in NaOH 1M and diluting them in PBS up to the desired concentrations reported in Table 7.1. HAS 4% was prepared dissolving the powder in phosphate

buffered saline (PBS) 1x. For the adsorption curve trial, each aliquot of the metabolites solutions was also prepared in presence of HSA 4% for a final volume of 500 μ L. The concentration ranges differ from one to the other, with crowded points around the physiological conditions. The solid substrates were cut into 4x4 mm piece and immersed the solution for 5 minutes, then thoroughly washed in MilliQ and sit to let dry for 30 minutes before measurements collection. Each condition has been observed on three substrates and in several replicas.

	Concentrations (μ M)
Adenine \pm HSA 4%	0.1, 0.2, 0.4, 0.6, 0.8, 1, 1.2, 1.4, 1.6, 1.8, 2, 5, 10, 15, 25, 50, 75, 100
Hypoxanthine \pm HSA 4%	0.1, 1, 2, 3, 4, 5, 6, 7, 8, 9, 10, 15, 25, 40, 50, 75, 100
Uric Acid \pm HSA 4%	10, 50, 100, 150, 200, 225, 250, 275, 300, 320, 350, 375, 400, 425, 450, 475, 500

Table 7.1 Concentration ranges for the analysis of the adsorption curves.

For the mixed solution and the evaluation of the effect of protein filtration, the metabolites concentrations were: adenine 0.2 μ M, hypoxanthine 10 μ M, uric acid 250 μ M, in the same batch. Both HSA 4% and HSA free versions were prepared. The solutions were used as prepared and after centrifugal filtration with 3 kDa cut-off Amicon Ultra 0.5 mL filters (Merck, DE), 15 minutes at 14000 g at room temperature. Protein-free metabolites solutions were filtered too in order to include the effect of the filtration efficiency. The solid substrates were cut into 4x4 mm piece and immersed the solution for 5 minutes, then thoroughly washed in MilliQ and sit to let dry for 30 minutes before measurements collection. Each condition has been observed on three substrates and in several replicas (Figure 7.2).

Controls are included as filtered protein-free solutions and with-protein unfiltered residual.

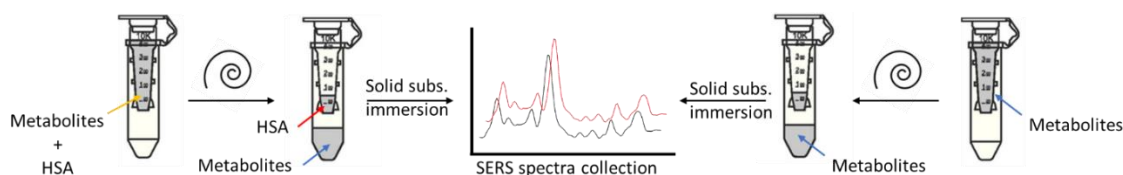


Figure 7.2 Schematic procedure: evaluation of the protein removal by centrifugal filtration.

The evaluation of the diffusion through the protein barrier involved the single solute solutions of adenine 10 μ M, hypoxanthine 10 μ M, uric acid 250 μ M and HSA 4%. For the samples preparation, two orders were followed: (i) the silver solid substrates were immersed for 5 minutes in the metabolite solutions, rinsed in MilliQ water,

immersed for 5 minutes in HSA 4% solution, rinsed again and let dry for 30 minutes before spectra collection; (ii) the same procedure as before was followed, but inverting the order of HSA and metabolites. Each condition has been measured in several replicas (Figure 7.3).

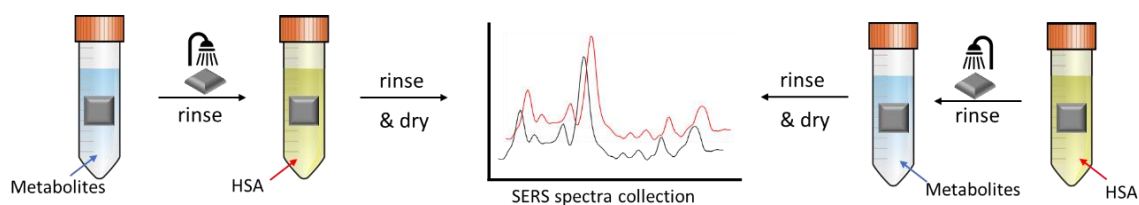


Figure 7.3 Schematic procedure: metabolites permeation through the protein barrier on the solid substrate (grey square).

7.2.4 Data analysis

Spectra have been entirely processed in the R environment [121] using *hyperSpec* [122], *baseline* [123], *ROCR* [136] and *MASS* [55] packages and other in-house developed scripts for spectra visualization.

The steps included: (i) Raman shift range selection, (ii) baseline correction (package *baseline*, method *als*, $\lambda = 6$), (iii) smoothing for noise reduction (data spacing = 3cm^{-1}), (iv) vector normalization.

The criteria for the baseline choice meant to avoid artifacts, and the *als* (asymmetric least squares) allows a correction by the 2nd derivative constrained weighted regression, with λ as constraining factor. The smoothing procedure returns evenly spaced spectra in the selected range, without the risk of overfitting. The smoothing is useful to reduce the signal-to-noise ratio through the *loess* (locally estimated scatterplot smoothing) function. It interpolates each spectrum onto a new x-axis with a local linear fitting by weighted least squares of a polynomial surface on neighbor segments, and the size of the neighborhood is controlled.

7.3 Results and Discussion

7.3.1 Adsorption curves

The comparison between the adsorption of metabolites on the surface and the same process in presence of HSA allows to evaluate the influence of the protein on the final SERS spectra. To this aim, the study has been extended to a wide range of metabolites concentrations with the double intent to characterize the whole system and to investigate the potential of the solid substrate in terms of analytes detection.

In Figure 7.4, the typical SERS spectra of adenine, hypoxanthine, uric acid and HSA on our silver solid substrates obtained with a 785 nm laser source are reported. Their profiles are known from literature and the intensity of their peaks accounts for the orientation of the molecule and its functional groups with respect to the silver nanostructured surface. Table 7.2 summarizes the assignment of the vibrational modes of the purines in analogy to what is reported in literature for the adsorption on silver NPs [137–139]. For the purines, the most characteristic peaks belong to the in-plane ring breathing mode sitting around 735 cm^{-1} for adenine and hypoxanthine and shifted to 640 cm^{-1} in the uric acid spectrum. The gap in wavenumbers can be related to the covalent structure of the uric acid, which is different from the other purines and rich in carboxyl groups. Density functional theory (DFT) calculations and experimental SERS studies on adenine seem to indicate that it tends to adsorb “edge-on”, namely orthogonal to the NPs surface through the nitrogens in position 3 and 9 [137,140–142]. This hypothesis is supported by the fact that the intense ring breathing mode exclude a “face-on” coordination through the π electrons and the band of the in-plane C8-N9 and N9-H deformation (1335 cm^{-1}) is well amplified in both adenine and hypoxanthine spectra, hence it should be close to the metal surface.

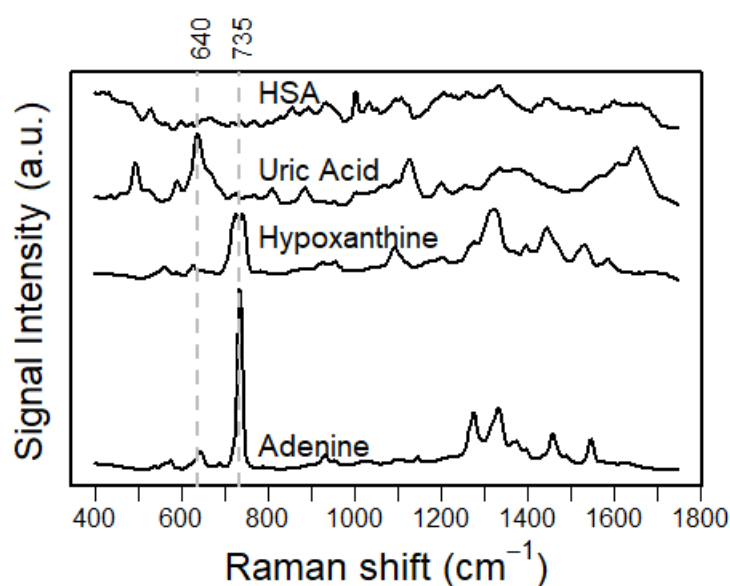


Figure 7.4 SERS spectra of adenine, hypoxanthine, uric acid and human serum albumin (HSA) on silver solid substrates with (laser source 785 nm, laser power 10%). Data are baseline subtracted, vector normalized and stacked for the sake of clarity.

Hypoxanthine is chemically similar to adenine: they differ only for a carbonyl and amine group in C6, hence it is supposed to adsorb in the same way on silver and the intense band at 1095 cm^{-1} (C8-N9 rocking) can confirm it. Unlike adenine, hypoxanthine shows two overlapped ring breathing bands, with maxima shifted at 725 cm^{-1} and 744 cm^{-1} , which has already been observed on both silver [137] and gold

[138] NPs; this aspect will be further addressed later in this section. Uric acid has three carbonyl groups that stretch at 1650 cm⁻¹ together with the C-N stretching and the N-H in-plane bending of the pyrimidine.

SERS* cm ⁻¹	Adenine***	Hypoxanthine***	Uric Acid***
500 (s)			C-N bnd, ip ring vibrations
565 (s)		Ring deformation	
575 (w)	oop C2-H, N9-H		
625 (m)		Ring breathing	
640 (vs)			C=O bnd, ring breathing
645 (m)	wag C5-N7-C8		
730 (vw)			N-H bnd
735 (vs)	Ring breathing	Ring breathing**	
815 (m)			C-N bnd, ip ring vibration
888 (m)			C-N str, oop N-H bnd
923 (w)		N1-C2-N3 bnd	
935 (vw)	str C5-N7		
1020 (m)	ip ring vibrations	ip ring vibrations	C-N str, ip ring vibrations
1095 (m)		C8-N9 rck	
1134 (s)			C-N, C-C str
1150 (vw)	str C8-N9, bnd N9-H		
1206 (m)			ip N-H str, bnd
1275 (m)		C8-H8 imidazole	
1325 (s)		C2-H2 imidazole	
1335 (s)	ip str N1-C2, C6-N1, C4-C5, N3-C4, C8-N9, bnd N9-H		
1368 (w)			C=O
1375 (s)	ip bnd C2-H, N9-H, N10-H12, str C5-N7, C6-N10, N1-C2		
1650			CO str, CN, ip NH bnd

Table 7.2 Band assignments according to [137–140]. str = stretching, bnd = bending, rck = rocking, wag = wagging. * (vs) = very strong, (s) = strong, (m) = medium, (w) weak, (vw) = very weak. ** In hypoxanthine it is split in two at 725 (imide) and 744 cm⁻¹ (amide). ***ip =in-plane, oop = out-of-plane.

The band at 888 cm⁻¹ is particularly intense and belongs to the N1-H out-of-plane bending in the pyrimidine ring between the carbonyl groups. This evidence indicates that the molecule adsorbs on silver through the C=N, N-H and C=O moieties of the six

terms ring and the out-of-plane bending band at 888 cm^{-1} suggests a tilted orientation, as only in this case is the z tensor of the polarizability of N1-H would be perpendicular to the silver surface [142]. Albumin has a low SERS cross section; the spectra is noisy and only the weak phenylalanine peak (1003 cm^{-1}) is evident (noise is amplified due to the vector normalization procedure). Before going any further, a concern for the analysis of these model solutions to be highlighted is the effect the pH would have on the SERS spectrum. Purines are known to be sensitive to pH changes and this effect may alter their orientation on the silver surface, resulting in changes in relative intensities [77]. Since purines are poorly soluble in water at neutral pH, they have been primarily dissolved in alkaline solution (NaOH 1M) and then diluted to the desired concentration with PBS. This implies that the higher concentrations are not completely buffered and still slightly basic, and this, in turn, influences the deprotonation states of the molecule, according to their pKa. Figure 7.5 reports the molecular structure, the tautomers and the pKa of the three metabolites. At neutral pH, adenine is uncharged in solution, while hypoxanthine exists in the two monoanionic amide-imine tautomers (N9 deprotonated) like uric acid, deprotonated at N3 [142–144]. For the sake of clarity, only the hypoxanthine tautomerism has been depicted.

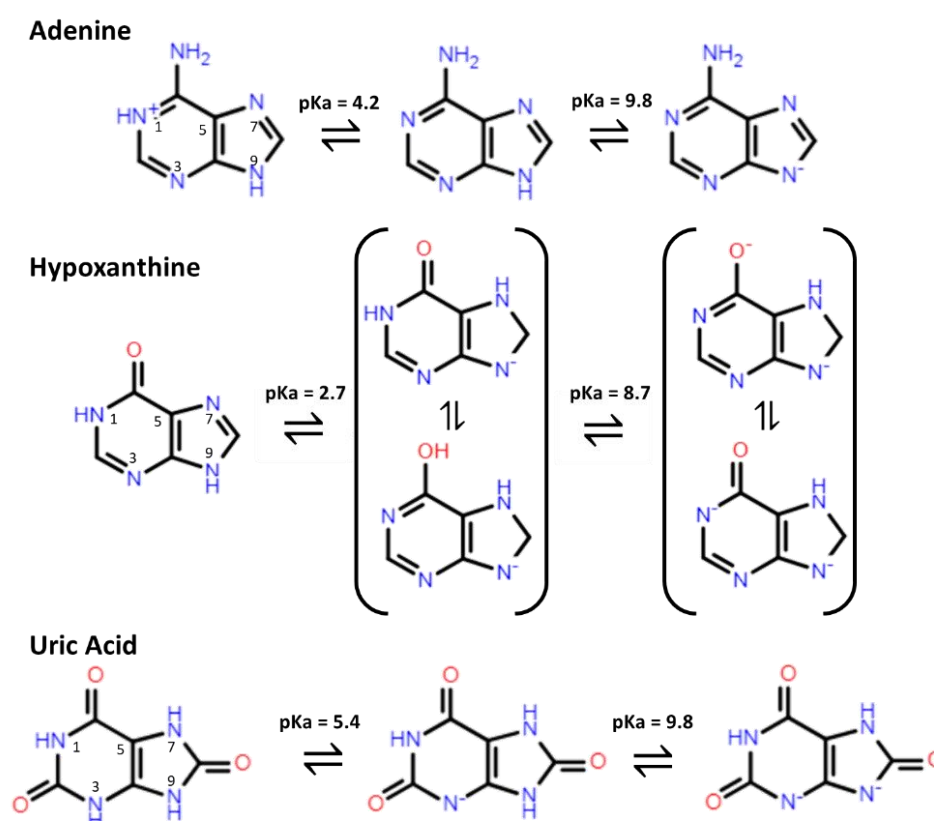


Figure 7.5 Adenine, hypoxanthine and uric acid structures and protonation state according to pH. All the purines undergo isomerism. Here the amide-imide tautomerism is reported only for hypoxanthine.

In this frame, the pH values of the three samples at the used conditions are reported in Table 7.3.

Adenine		Hypoxanthine		Uric Acid	
C (μM)	pH	C (μM)	pH	C (μM)	pH
0,1	7,45	0,1	7,38	1	7,40
0,2	7,45	1	7,40	10	7,89
0,4	7,45	2	7,73	50	11,08
0,6	7,45	3	7,73	100	11,54
0,8	7,47	4	7,8	150	11,75
1	7,50	5	7,85	200	11,90
1,2	7,58	6	7,86	225	12,05
1,4	7,60	7	7,86	250	12,06
1,6	7,62	8	7,88	275	12,01
1,8	7,65	9	7,88	300	12,04
2	7,73	10	7,89	325	12,07
5	7,85	15	8,20	350	12,11
10	7,89	25	10,47	375	12,15
15	8,20	40	10,8	400	12,18
25	10,5	50	11,08	450	12,30
50	11,09	75	11,25	500	12,41
75	11,25	100	11,54		
100	11,54				

Table 7.3 pH values for the three metabolites solutions at the experimental conditions.

Figure 7.6 a and b report the average SERS spectra of adenine in the whole range of concentrations. For better clarity, only some representative concentrations have been included. For the univariate analysis, the area under the ring breathing peak is evaluated, as it is the dominant feature and it is concentration-sensitive. The plots in Figure 7.6 c and d report the evolution of the peaks area versus the concentration of the analytes. The relative intensities of the peaks do not undergo significant changes in the adenine spectra, nor shifts are present, suggesting that adenine does not change its orientation on the metal surface as the concentration increases. The area of the 735 cm^{-1} peak follows a sigmoidal trend both in absence and presence of HAS (the dashed lines in Figure 7.6 c are guide for the eye). The effect of albumin is evident: the peak is proportionally less intense over the whole concentration range, and this can be due to the steric effect of the protein on the metal surface, which hamper or compete with the metabolite adsorption, or to an adenine sequestration upon HSA-binding. Albumin is able to bind various ligands, negatively and positively charged,

endogenous and exogenous, included adenine, sequestering it from the bulk solution, thus hindering adsorption. The adsorption mechanism is still under investigation and has not been unambiguously defined, hence no fitting equations are going to be used to extrapolate binding constants for the observed phenomena. However, the trend resembles a cooperative behavior, as described in § 4. Cooperativity is a common trend that can be identified in several fields and implies an acceleration of the process ongoing after an initial inertial phase. The reason of the acceleration varies depending on the system. The typical curve shows a slow beginning, where the signal is not dependent on concentration, followed by a dramatic increase in the adsorption rate that culminates in the final plateau, in which the monolayer condition is reached or in which the maximum number of the analyte molecules are adsorbed [107]. The lower and upper limits and the slope of the sigmoid strictly depend on the features of the solid substrate with respect to the analyte under exam. In general, purines tend to form clusters in aqueous solution by means of π - π stacking interactions, which may be the cooperation driving force. This is a type of hydrophobic interaction between the purines induced by the solvent (water) and it is enthalpically-driven rather than entropically-driven. Indeed, the energy lost in the disruption of the hydrogen bond web during the aggregation is recovered by the stabilization of the stacked clusters [145]. The aggregation of purine in aqueous solution has been extensively reported in literature as well as their orientation on the silver and gold nanoparticles [146]. Nevertheless, little is reported about the stacking of purines bound by a metal surface and their preferential mutual orientations. Our data seem to have no clear indication of an ongoing hydrophobic π - π interaction between adenine molecules, however, since no shift is detected upon increasing adenine concentration. Moreover, SERS spectra do not show any alteration of the peaks positions nor the identification of several population of orientation, hence it is possible to hypothesize that only one orientation is mainly detectable, namely the edge-on adsorption on silver through N3 and N9. The experimental facts might be compatible with an initial edge-on adsorption of small adenine aggregates from the solution, and not by individual molecules. This would explain why shifts are not detected upon increasing adenine concentration, even admitting a cooperative mechanism of adsorption.

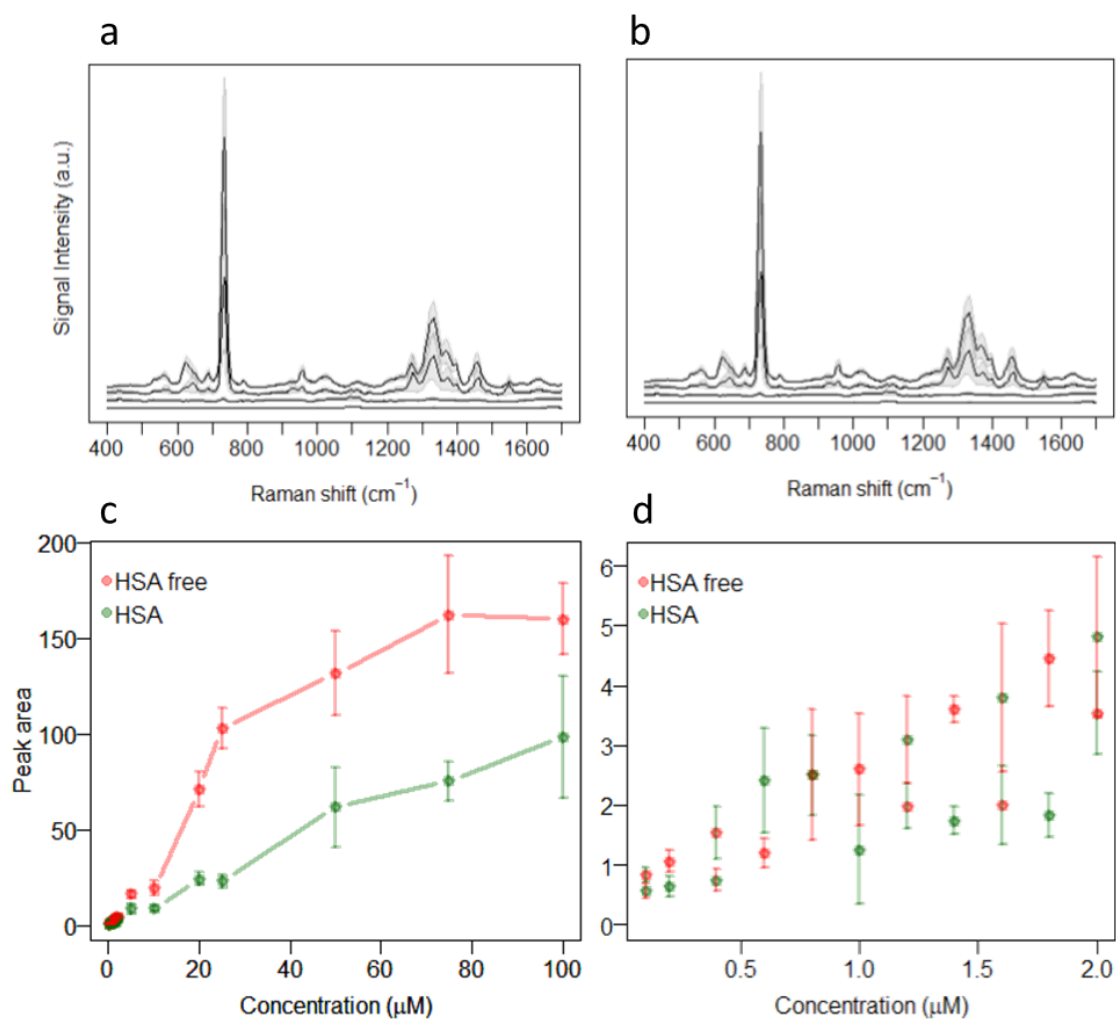


Figure 7.6 Representative SERS spectra of adenine (a) without HSA and (b) with HSA, at four crescent concentrations reported as average \pm 1 standard deviation (shaded area). Laser source 785 nm, laser power at the sample 10%, 1 scan of 10 seconds of exposition. (c) Mean (\pm 1 standard deviation) of the peak area trend versus concentration and attempt of a sigmoidal fitting, (d) magnification of the 0.1 – 2 μ M region.

However, further examinations are required to confirm this hypothesis. In the physiological range (0.1 – 2 μ M, Figure 7.6 d), adenine shows a linear trend for the HSA and condition. The setting-up of an accurate purine quantification method goes beyond the purpose of this experiment, but, nevertheless, preliminary data indicate that this might be feasible.

In the case of hypoxanthine spectra (Figure 7.7 a and b), a significant change in the relative intensity of the ring breathing doublet at 725 cm⁻¹ and 744 cm⁻¹ happens. The discussion on its origin involves several factors, such as the orientation of the molecule on the NP surface, the protonation state, the presence of isomers. Actually, hypoxanthine exhibits remarkable amide-imide tautomerism ($\text{H-N-C=O} \rightleftharpoons$

N=C–O–H, Figure 7.5) that may primarily account for the band shift. The intensity of the blue shifted peak increases, reaches an equilibrium at about 50 μM with the red shifted and then exceeds it in terms of intensity. The pH may have a role in this. Indeed, hypoxanthine exists in different structures in different pH. In physiological buffer (pH 7.4), the amide form in Figure 7.5 is stable, whereas the imide prevails at alkaline pH [135]. At 25 μM the pH increases, induces the second deprotonation at N1 and the stabilization of the amidic structure, since the oxygen can more efficiently delocalize the negative charge. The negative charge induces a change in the orientation of the molecule with respect to the silver surface. According to literature, it goes from an almost perpendicular position coordinated through the N3 and N7, to a tilted orientation or nearly parallel to the metal surface including the electrons of N1 and O6 to the interaction [137]. Conversely, the presence of HSA alters the spectra pattern, not only as far as the overall intensity is concerned. The ring breathing band is present but does not change neither with concentration or pH in terms of relative intensities and suggests the stabilization of the amide form. A possible reason can be found in the stabilizing role of the protein on the silver surface, which hinders sterically the orientation change of the small molecules and somehow “fixes” them on the surface. However, since the double band accounts for the population of the two tautomers, the binding curve has been built including the area under the spectra in the region between 690 cm^{-1} and 770 cm^{-1} . The trend of the peak area versus sample concentration is different from what observed for adenine: the sigmoid is flattened and it does not reach a plateau in the considered concentration range, but again, the HSA affects the binding kinetics of the metabolite. The range of interest (1-10 μM) does not allow any kind of quantification within these experimental conditions: the signal is weak, and few differences appear among the low concentrated samples.

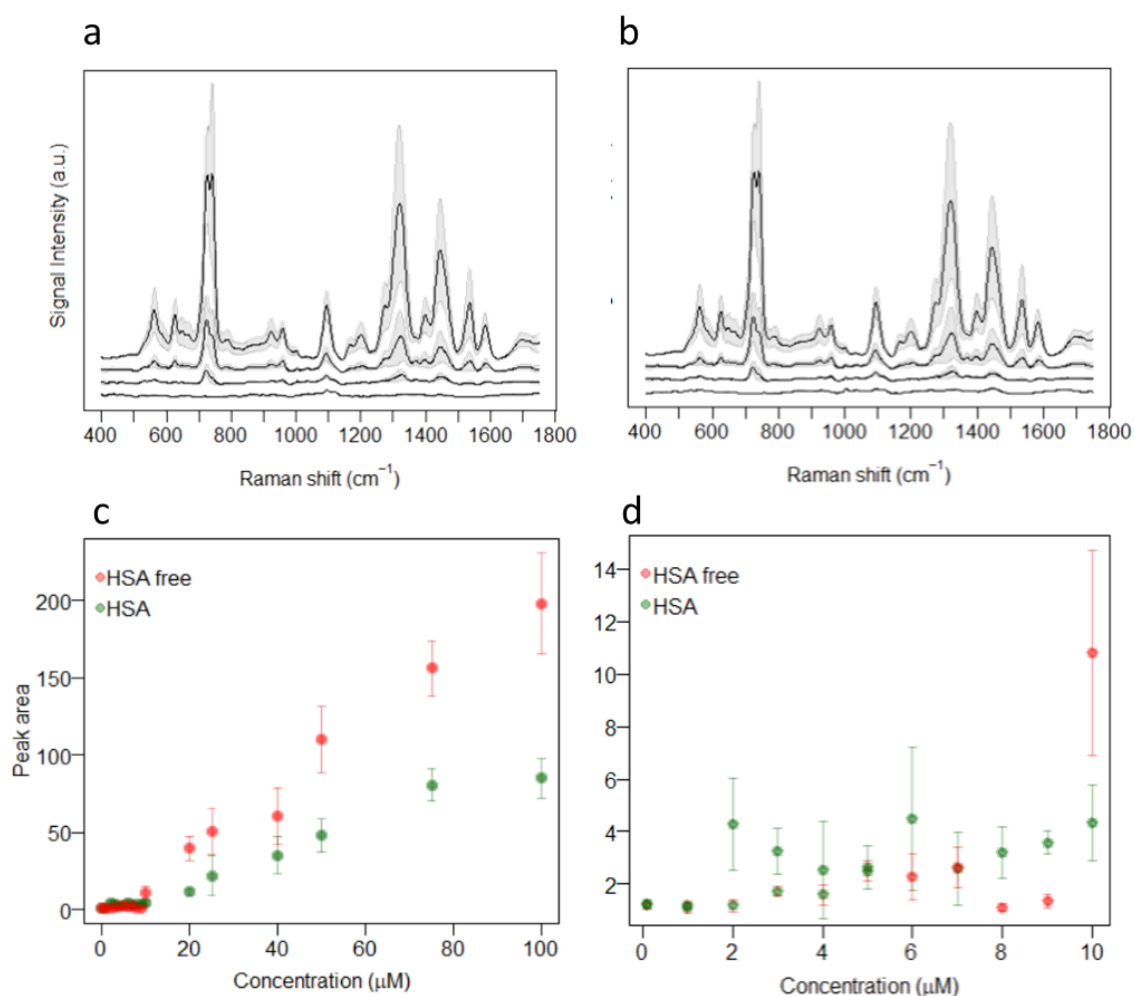


Figure 7.7 Representative SERS spectra of hypoxanthine (a) without HSA and (b) with HSA, at four crescent concentrations reported as average ± 1 standard deviation (shaded area). Laser source 785 nm, laser power at the sample 10%, 1 scan of 10 seconds of exposition. (c) Mean (± 1 standard deviation) of the 735 cm^{-1} peak area trend versus concentration, (d) magnification of the $0.1 - 10 \mu\text{M}$ region.

Uric acid displays a pattern similar to the hypoxanthine one (Figure 7.8). Indeed, a splitting of the ring breathing peak (640 cm^{-1}) appears starting from $150 \mu\text{M}$ and becomes more evident at higher concentrations. Even in this case, the high pH promotes the deprotonated form and its several amide-imide tautomers which adsorb differently on the silver nanoparticles and broaden the ring breathing bands [147]. At the same time, the intensity of the $\text{C}=\text{O}$ peak (1650 cm^{-1}) decreases as far as the imide structure of uric acid prevails. The overall intensity of the spectra decreases with concentration, probable symptom of the increased molecular crowding surrounding the SERS substrates which may partially reabsorb the scattered signal. In presence of HSA 4% the situation changes, according to the hypoxanthine series: the ring breathing band is slightly asymmetric and the relative intensity with the $\text{C}=\text{O}$

peak is not changing in the concentration range, but a single preferential orientation is observed, namely the amide form, in analogy with the case of hypoxanthine.

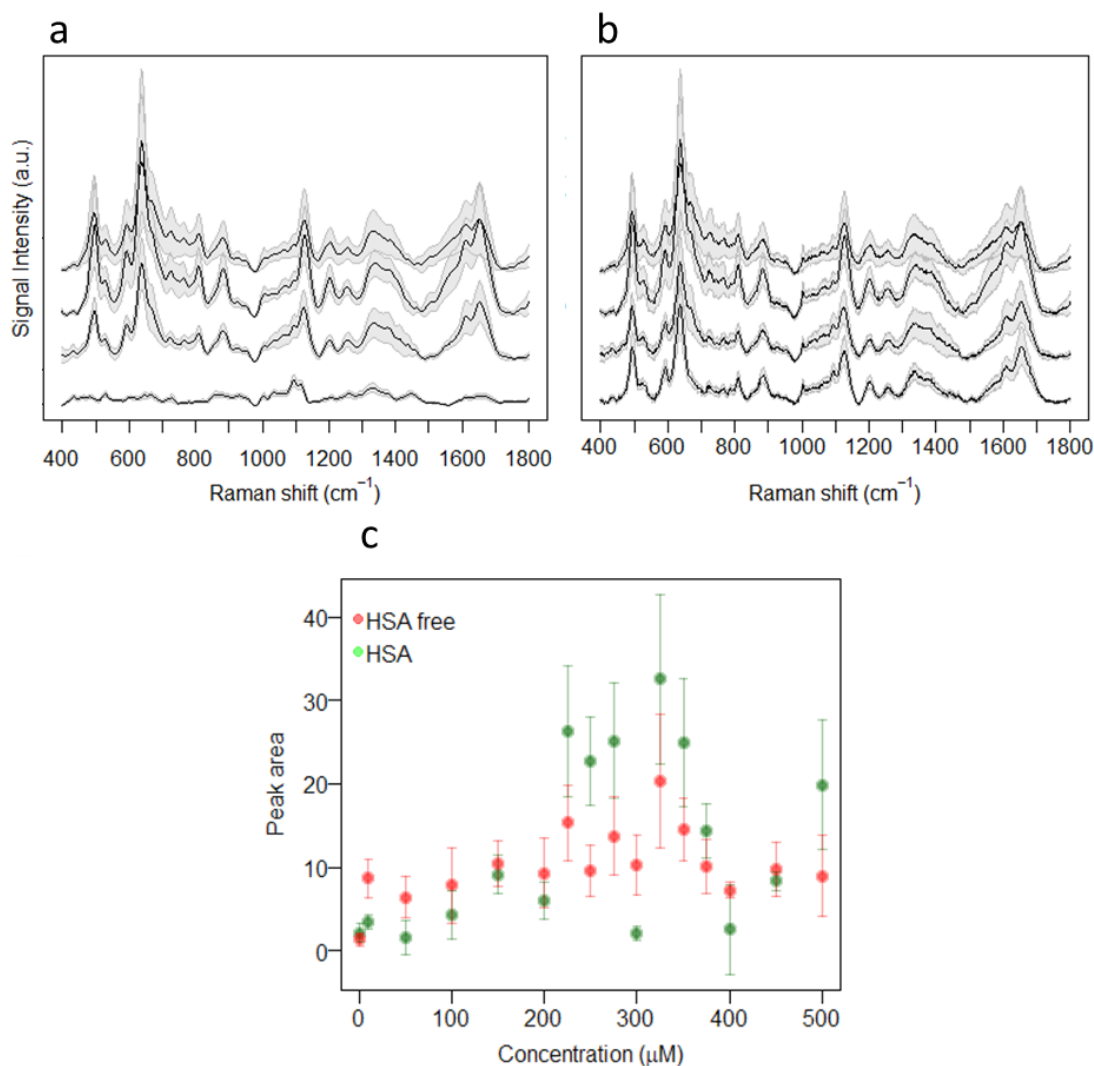


Figure 7.8 Representative SERS spectra of uric acid (a) without HSA and (b) with HSA, at four crescent concentrations reported as average \pm 1 standard deviation (shaded area). Laser source 785 nm, laser power at the sample 10%, 1 scan of 10 seconds of exposition. (c) Mean (\pm 1 standard deviation) of the 640 cm⁻¹ peak area trend versus concentration.

The evolution of the ring breathing peak area with concentration suffers of both the abundance of isomers at high pH and of the aforementioned issues due to the high concentration levels. It is not possible to identify a specific trend, then, although in this case, HSA has a surprising effect: the intensity and area of the peaks are higher with respect to the protein free case. This may reveal that the protein does not only show steric effects, but actively interacts with the dissolved species. In the adenine and hypoxanthine cases, HSA reduced their available concentration as freely diffusing species with a scavenging mechanism. In the uric acid case, HSA seems to promote the

adsorption of the metabolite. This point deserves further studies, in particular as long as the use of SERS solid substrates can be extended to biofluids analysis in which uric acid plays a key role.

In general, paper-based solid substrates are great tools for the analysis of metabolites in presence of proteins, as the pre-aggregation reduces the SERS-suppressing effect of the protein corona.

The protein corona is present anyway and this systematic approach revealed that albumin:

1. changes the adsorption kinetics for the metabolites towards the metal surface,
2. acts both as physical/steric and chemical hindrance for the metabolites,
3. induces the preferential adsorption of peculiar stabilized chemical structure.

Provided this, the answer to the original question “does albumin affect the adsorption process of small metabolites?” is positive. The next question regards whether the protein removal would further affect the SERS spectra of the system and how.

7.3.2 The role of protein filtration

The SERS analysis of the blood constituents revealed how the filtration process can affect the relative intensity of uric acid, adenine and hypoxanthine. This effect has been evaluated in the simplified model system, where adenine, hypoxanthine and uric acid coexist in a mixture at their indicative physiological concentrations (0.2 μM , 10 μM , 250 μM , respectively) both as protein-free and in presence of HSA 4%. All the samples have been filtered by centrifugation with a 3 kDa cut-off and the resulting SERS spectra are reported in Figure 7.9. To include the role of the filtration efficiency, also the protein free mixed solutes solution has been filtered accordingly. Indeed, both the filtered samples spectra display reduced intensities with respect to the corresponding unfiltered controls (high filter retention rate), but the profiles are not affected.

Looking at the spectra, the most remarkable difference does not regard the filtration step, but rather depends on the presence of HSA in the solution. In the frame of the chosen experimental conditions, the contribution of hypoxanthine is the more pronounced in the protein-free solution, whereas the uric acid fingerprint is weaker. The addition of HSA to the solution heavily changes the spectral profile: the relative intensities of the 735/640 cm^{-1} bands are inverted and the uric acid bands emerge. In analogy to what observed in the previous paragraph, albumin reduces the hypoxanthine adsorption rate and enhances that of uric acid. So far, the mechanism behind this behavior is not clear. A partial explanation may involve the electrostatic repulsion between the metabolites, especially uric acid, and HSA. Indeed, the pH is > 12 in the 250 μM uric acid solution, hence all the metabolites of the mixture are in their deprotonated form, as well as the protein, although little is known about the HSA conformation and the binding with purines in this extreme condition [148,149]. Surprisingly, the filtration of the mixed metabolites and HSA turns into spectra similar

to the unfiltered case: part of the adenine/hypoxanthine fraction is preferentially retained by HSA while uric acid increases in terms of relative concentration and its contribution to the spectra emerges. This may reveal an unseen aspect of the story, an intrinsic feature of the protein. It might be not the protein *corona* to modulate the metabolites-nanoparticle interaction, but it is the protein itself to specifically alter the chemical composition of the medium surrounding the nanoparticle, hence the final spectra.

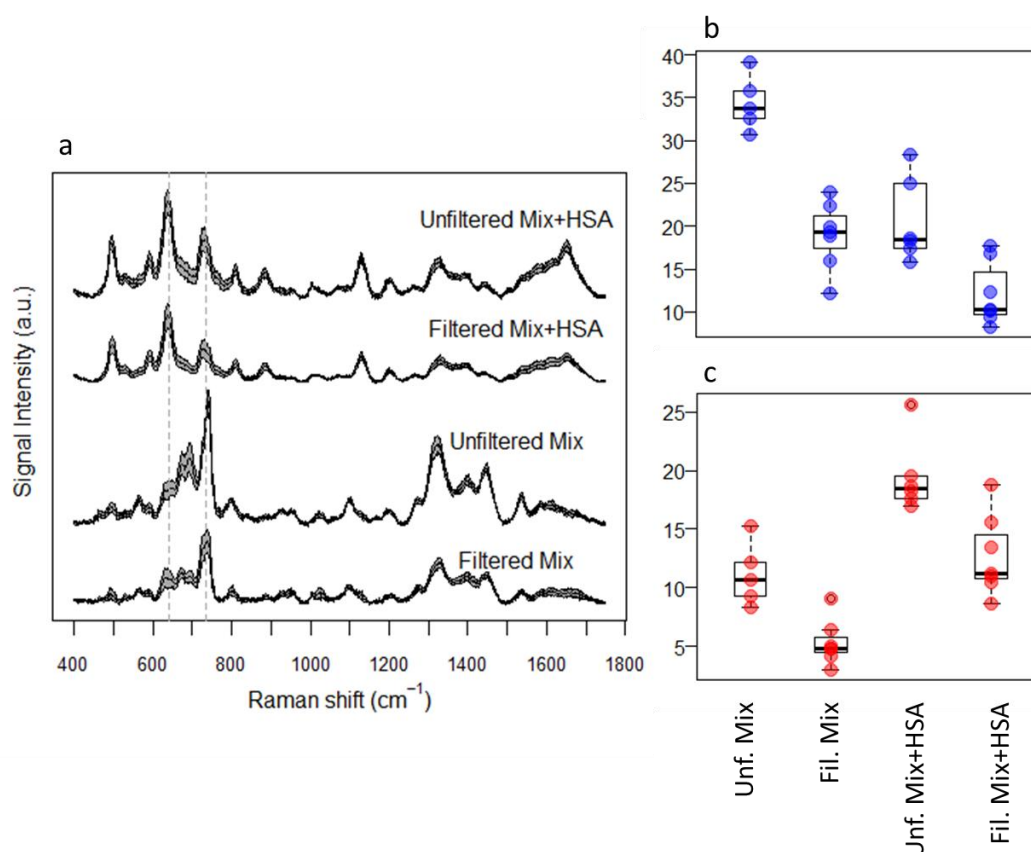


Figure 7.9 Effect of HSA filtration on the spectra of the mixed solutes solutions. (a) Average spectra \pm 1 standard deviation are reported. Laser source 785 nm, laser power at the sample 10%, 1 scan of 10 seconds of exposition. The boxplots focus on the area of the ring breathing of hypoxanthine/adenine and uric acid, with maxima at (b) 735 cm⁻¹ and (c) 640 cm⁻¹, respectively. Mix = metabolites mixture, Mix+HSA = mixture of metabolites and HSA 4%. Filtered (Fil.) and unfiltered (Unf.) data observed pairwise quantitatively show the filter interference on the sample recovery, and the introduction of HSA reverses the relative intensities of the two bands.

7.3.3 The metabolites permeation through the protein corona

To complete the overview on the protein influence over the SERS spectra on silver solid substrate, we focused on the effect of HSA steric hindrance on the nanoparticles. In other words, how much is the protein permeable to small molecules? Conversely,

is the NPs-metabolite binding strong enough not to be altered after the addition of HSA? According to the protocol described in the Methods section, each metabolite has been adsorbed on the paper-based cAg substrate before or after the addition of HSA to the substrate itself (Figure 7.10). The conditions are different with respect to the previous tests: now metabolites and protein do not co-adsorb competitively, but they follow their own separated kinetics.

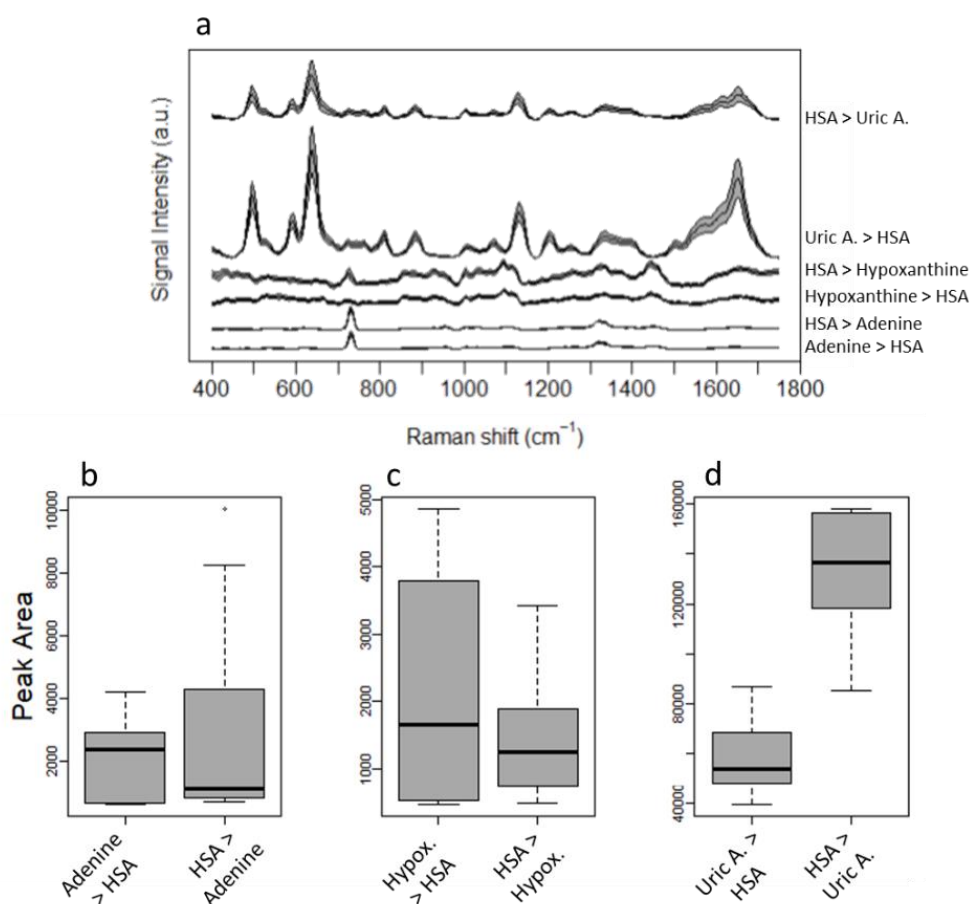


Figure 7.10 Metabolites permeation through the HSA layer. (a) Average spectra ± 1 standard deviation. Laser source 785 nm, laser power at the sample 10%, 1 scan of 10 seconds of exposition. Labels on the right indicate the order of immersion. (b, c, d) Peak area values for the three metabolites in the two orders of immersion.

The average spectra of adenine in the two conditions are comparable, whereas the hypoxanthine signal increases slightly when added after HSA. The point is that the metabolite is able to diffuse through the protein layer and reaches the NPs surface, but the uric acid example has a different outcome. The presence of pre-adsorbed HSA reduces the number of available sites and the small molecules are not able to overcome it. A reasonable explanation involves again the protonation state of the species: at the used concentrations and neutral pH, adenine and hypoxanthine are neutral or mono-deprotonated, respectively, and the electrostatic repulsion

experienced with respect to HSA has a low impact on their adsorption. Uric acid exists in its fully deprotonated form at basic pH and may find hindrance to the permeation through a negatively charged protein. Hence, the HSA > uric acid case has a lower intensity with respect to the other case.

In summary, the protein plays a key role in the adsorption kinetics of the considered metabolites, and it affects their diffusion from the solution to the nanostructure interface. Hence, extra-care is required when working with protein samples provided the complexity of interaction between macromolecules and small ligands which deeply depends upon their chemistry (protonation, pH, etc.).

7.4 Highlights:

- The presence of the protein and metabolic corona around nanoparticles mutually affects the outgoing SERS signal, especially when the two species co-adsorb.
- Both chemical (specific binding, aggregation, impoverishment of the solution) and sterical hinderance (size exclusion effect) occur.
- pH matters: high pH alters the protonation state and the 3D conformation or stacking of both protein and metabolites.
- The SERS substrates we developed are stable up to pH = 12.

8 SERS and Diagnosis

Established the fundamental aspects of the SERS technique in the bioanalytical field, it is now time to approach the clinic application. The open question regards whether or not the developed SERS sensor is able to correctly predict the state of health of an individual, pursuing the challenge of the Point of Care technology.

8.1 Background

Nowadays, early diagnosis of diseases is an absolute priority, allowing proper therapeutic choices and the improvement of living conditions. To date, only few diseases can take advantage of screening campaigns and prevention policy.

In this frame, SERS has been drawing the clinical attention worldwide for over a decade, being a versatile, nondestructive and cost-effective technique for diagnostic and theranostic purposes [86,150]. It is now established that label-free SERS spectra of biofluids reflect the metabolic profile of the patient, playing its role in the metabolomic area. Therefore, it has been usefully applied in diagnostics to provide a new instrumental approach complementary to the accepted immunochemistry, histopathology and imaging techniques [31,36].

In the latest years, several papers have been published on label-free SERS on biofluids for diagnostic purposes. Cancer diagnosis is the top-rated topic, including prostate [151–154], breast [31,155], lungs [155–157], bladder [95], colorectum [158], nasopharynx [159–161], esophagus [35,162], cervix [163], oral cavity [164], stomach [165], liver [99,161,166] tumors, but also hepatitis [167], chronic kidney disease [168], bacterial infections [169–172] and so on. Liquid biopsy is by far predominant, being minimally invasive in most cases. Saliva, serum, plasma, urine, cerebrospinal fluids are usually investigated. This is the real advantage of SERS application in diagnosis, allowing to avoid more invasive techniques like biopsy, while keeping a high accuracy with a rapid response, and reducing the physical and psychological impact on the patient.

The full SERS potential is reached when spectra are unraveled through multivariate data analyses for supervised classification purposes (i.e., PCA-LDA). This aspect is an integral part of the studies presented here.

Established all these positive aspects, it is time to identify the proper way to channel the SERS diagnostic potential in the clinical routine. As remarked in § 1, the experimental set-up must be tailored for the specific application in order to guarantee optimal performances in terms of reliability, stability of results, user-friendliness, aiming at the Point of Care technology and reducing the costs for the health system. It is a long way, but the final goal would be to implement the diagnostic pathway within the screening or detection steps, bringing the analyses from the bench to the bedside (Figure 8.1).

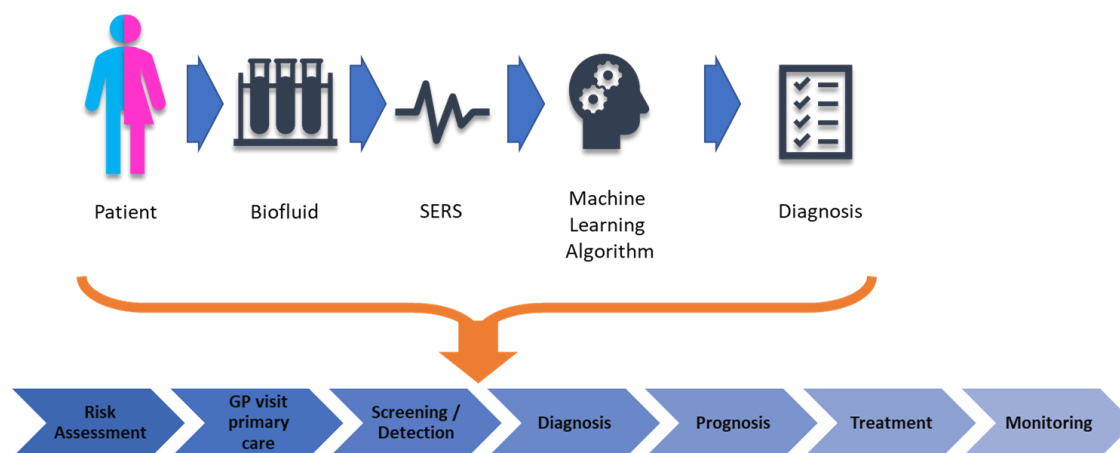


Figure 8.1 The aim for a new diagnosis pathway with SERS.

In this paragraph, three different frameworks have been proposed, namely breast cancer, liver inflammation and hepatocellular cancer. Particular attention has been given to the Design of the Experiment (DoE) trying to overcome some limits we faced in the past [31] and which are often found in literature, especially considering the number of tested subjects.

8.1.1 Role of the preanalytical steps

Starting from the preliminary results reported in papers by Cervo and Bonifacio, attention has been paid to the samples collection and preparation [31,36]. In accordance with Premasiri, a mandatory requirement in the preanalytical step is the time of action. In particular, samples must be prepared and measured or stocked within 1 hour from the draw and cells (RBCs, PBMCs) should be separated from plasma or serum [33]. The reason lies in the increasing levels of hypoxanthine in the extracellular environment as metabolic product of RBCs with time at 4 °C: this can pass from the original μM level to the hundred μM in few hours. The same deterioration is found after freezing-thawing cycles, which must be limited. This ageing effect can heavily affect the SERS spectra: Ag NPs are extremely sensitive to purines concentration changes, as observed in the previous Chapters. If purines signature can prevail over other contributions, any consideration on spectroscopic

data in terms of metabolic fingerprinting is flawed [33]. Conversely, SERS is often suggested as a powerful tool for the monitoring of purines levels in biofluids, like in forensic science for the ageing of blood samples, notwithstanding the fact that metabolites concentration is subject sensitive.

Moreover, considerations should be given to the design of the experiment to be able to collect homogeneous data in terms of sample preparation and instrumental conditions, as well as to randomize the nanoparticles batches (this step is necessary in order to verify the robustness of the method and to simulate a realistic routinely application of the technique).

8.1.2 Breast Cancer

Breast cancer (BC) is the main cause for cancer death in women worldwide and the most spread non-cutaneous female tumor in Europe [173,174]: in the lifetime, 1 out of 8 women experience BC.

At the first diagnosis, early tumors are most frequently detected (50%, stage 0-1) with respect to the locally advanced ones (33%, stage 2-3). Metastatic tumors are rare (5%) [175]. Thanks to the progresses and the scientific knowledges obtained over the last 50 years on both the therapies and the screening tools, the survival rate for women after five years from the BC diagnosis rose up to 87%. This is a great result, but not enough: only in Italy, every year 12000 new cases of metastatic BCs are diagnosed, and about 36000 women must confront with this disease. The breast cancer screening is one of the first weapon able to reduce the mortality. Besides, the risk of overdiagnosis is still too high, and there are no methods to understand if a lesion would become an invasive cancer or not [176]. Since the late 70's, the diffusion of mammography as the golden standard screening technique between 50 and 69 years old paved the way towards early detection. Indeed, in Europe the survival rate increased up to 40% in the 5 years after the first diagnosis from the introduction of mammography, compared to a constant or slightly increased incidence [177]. Nevertheless, mammography is painful, exposes the subjects to X-Rays doses and entails high costs for the national healthcare systems, and this is an issue that hampers the spread of the screening all over the poorer countries. Ultrasounds are in general not recommended as screening techniques but can be used for a better investigation under clinic control. The main drawbacks of mammography are to be found in the overall high false positive (15%) and false negative rate (10%), commonly due to the heterogeneity of the breast tissue density in the screened subjects that induce misleading diagnosis [178,179]. Moreover, mammography is inadequate for young women for the same reason and the lack of alternative for early detection techniques leads to death more than 20,000 women younger than 50 in Europe every year, as BC in young age is usually more frequent (40% in Europe versus 22% for over-50), aggressive and with a lower survival rate (Globocan 2108, gco.iarc.fr). Breast cancer classification can follow several standard parameters, like grade, type, stage and gene expression. The grade (1 - 3) is assessed by pathologists

observing the appearance of the tissue and cells after biopsy. It ranges from the normal-like cells to the unrecognizable cells due to growth. The type addresses to the location of the carcinoma (ductal, lobular, etc) and the invasiveness (in situ or not), including inflammatory BC, metastatic or rare BC forms. The stage (0 - 4) regards the evolution of BC and extension in volume and location. The classification considers the gene expression similarity to health cells (Luminal A-like and B-like), the amount of expressed HER2 (HER2+, HER2-), the presence of estrogen and progesterone receptors on the cellular membrane (ER+/-, PGR+/-). The subgroups are characterized by different diagnostic frequency, prognosis and therapy. For instance, Luminal A features a reduced proliferation and a better outcome with respect to the Luminal B, but is the most frequent. Triple Negative tumors are characterized by the absence of ER and PGR receptor and HER2 normal levels. They are rare, but still the most dangerous, difficult to treat and with the worst prognosis. These biomarkers are quantified on tissue biopsy. To date, no BC biomarkers have been approved in biofluids: in clinic, tests on serum include the quantification of the carbohydrate antigens 15.3 (CA 15.3) and of the carcinoembryonic antigen (CEA), which relate to the BC progression and to the therapy monitoring in advanced stages [176].

In the frame of a collaboration with the CRO Institute (Aviano, IT), label-free SERS has been applied for an early diagnosis on serum samples, aiming to identify the effect of cancer on metabolism, especially at the very first stage. The intent was to provide a complementary approach to the accepted immunochemistry and histopathology methods, following some preliminary results recently published by our research group [30,31] that provided good accuracy, sensitivity and specificity rate.

8.1.3 Liver disorders

As known, liver plays a pivotal role in the metabolism and catabolism of lipids, proteins, amino acids, carbohydrates, hormones, urea and other building blocks. Liver diseases are strictly connected to the alteration of specific metabolic pathway, and this effect may be observed in the fingerprint of biofluids that SERS spectra can provide.

In the frame of a collaboration with the Fondazione Italiana Fegato Onlus (Italian Liver Foundation, FIF, Trieste, IT) two projects have been developed to build up an early diagnosis liquid biopsy method able to discriminate:

1. patients with several non-alcoholic fatty liver diseases (NAFLD), by means of plasma samples,
2. patients with cirrhosis, hepatocellular carcinoma (HCC) and controls, by means of serum samples.

The FIF Onlus supported and defined the inclusion criteria, the partial design of experiment and the samples recruitment.

8.1.3.1 NAFLD progression and diagnosis

The non-alcoholic fatty liver disease (NAFLD) is a manifestation of the metabolic syndrome at hepatic level and is one of the most spread disorder worldwide (20-30% of the general population). It correlates with nutritional or metabolic disorders and with the increased fatty acid levels in serum: they accumulate in liver cells leading to steatosis and balloon cell degeneration [180]. Moreover, apparently healthy subjects can manifest these disorders, being then at higher risk [181]. 10% of NAFLD can evolve into more severe diseases, like nonalcoholic steatohepatitis (NASH), liver inflammation, fibrosis, cirrhosis and cancer (HCC) [182]. Although steatosis alone is considered non progressive, the molecular evolution to more complicated forms of liver disorders is still poorly understood (Figure 8.2) [183,184]. The correct identification of the stage of the disease spectrum is of paramount importance in the therapeutic choices, considering that severe conditions (i. e., inflammation or fibrosis) can compromise the organ regeneration, while mild ones (i. e., steatosis) can still be treated with no counter effects [185–187]. The gold standard for NAFLD diagnosis and staging is the liver biopsy, but the decision to perform this procedure is hard due to the high risk of complications. Currently, the non-invasive diagnostic techniques are reliable only for patients with body mass index (BMI) < 30 kg/m² and include elastography, ultrasound, Magnetic Resonance Imaging (MRI), multivariate analysis of risk factors and hepatic enzymes levels. These methods are not suitable for patients with BMI > 30 kg/m², making them a high-risk target. Moreover, the MRI is far from being an acceptable screening technique, as it is not effective in terms of time and costs, beside the fact that the multivariate algorithms are not reliable [188].

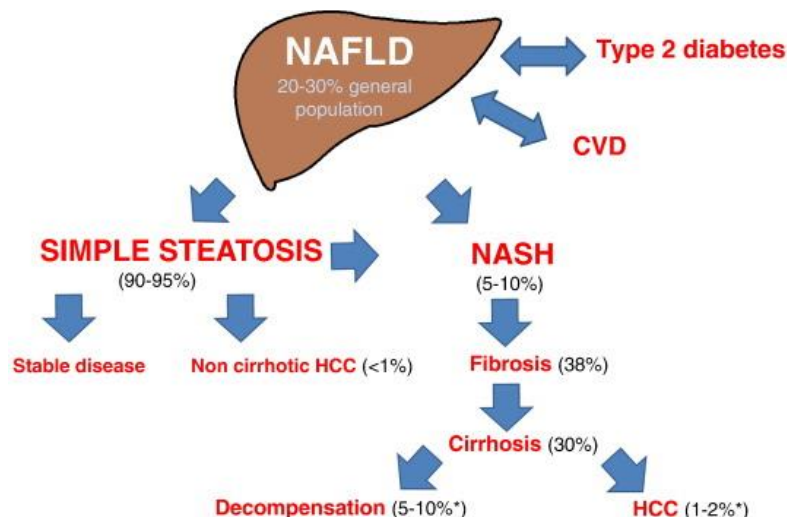


Figure 8.2 Evolution of the non-alcoholic fatty liver diseases [189].

The main aim of this study is to provide a non-invasive and accurate diagnosis method to allow to distinguish between liver inflammation and the NASH, as they deserve different therapeutic regimes. NAFLD within the inflammation stage can be

pharmacologically treated, while worse liver failures may lead to the loss of liver function and, then, transplant is the only option.

8.1.3.2 From cirrhosis to Hepatocellular Carcinoma

The hepatocellular carcinoma (HCC) is the fifth most frequently detected neoplasia and the second leading cause of cancer-related death worldwide. It occurs mostly after the exposition of a cirrhotic liver (LC) to risk factors, such as B and C hepatitis viruses, alcohol addiction, nutrition and metabolic disorders. LC is also a limiting factor for anticancer treatments, as it alters pharmacokinetics, increases the risk of hepatotoxicity and may limit surgical approaches. As a consequence, it is fundamental to distinguish between cancer and LC for a proper treatment of the diseases [190]. For instance, liver transplant is the principal potential cure for both of them: data show that the 70% of patients is alive after 5 years from the surgery [191]. However, the shortage of donors compels the identification of priority criteria for transplant itself or other surgery alternatives, which must pass through the correct identification of the boundary between HCC and LC [192]. The urgent need is to find a cancer diagnostic tool that could overcome the issues which are connected to the common routines. To date, HCC detection follows the *Barcelona clinic liver cancer* (BCLC) staging system through the positive accordance of two imaging techniques (ultrasound, solid nuclear magnetic resonance, axial tomography) [193]. However, they are only able to detect tumor masses with diameter higher than 5 mm, hence in an advanced stage [194]. On the other hand, the analyses of the HCC biomarkers and molecular mechanisms of oncogenesis have been going through metabolomic studies on liquid biopsy that lead to an earlier detection of HCC. Liquid nuclear magnetic resonance, liquid and gas chromatography hyphenated to mass spectrometry are some of the available analytical techniques, but still too onerous in terms of costs and machine-time considered their low sensitivity [20,195,196].

In this frame, SERS is tested again for the multi-marker label-free diagnosis of these diseases, as depicted in the former clinic cases. Positive results would allow to introduce the SERS technique as support to the clinical analyses to identify faster a proper therapy or to evaluate sooner the need to turn to transplant.

8.2 Materials and Methods

The procedures shared by the three experimental sections are presented hereafter in order to avoid redundancy. The common parts relate with the SERS substrate fabrication, the instrumental apparatus and data analysis protocol. Conversely, specific cohort recruitment procedures, sample preparation, spectra collection, results and discussion will be found in the dedicated sections.

8.2.1 SERS substrate fabrication

Citrate-reduced silver nanoparticles have been synthesized according to Lee and Meisel [17], used both in colloidal form (cAg-colloids) and fixed on a paper-based substrate (cAg-paper). The solid substrates have been prepared according to the procedure #1 reported in Chapter 4, starting from citrate-reduced silver NPs according to Lee and Meisel (cAg-colloids). For the list of reagents see Appendix 1; for the substrate fabrication protocol and characterization, please refer to § 4. The choice of the substrate protocol accounts for the good spectroscopic performances in terms of signal-to-noise ratio for the considered samples.

8.2.2 SERS instrumentation

The measurements have been performed in air at room temperature with a i-Raman Plus portable system (BWS465-785S) connected to a compatible Raman video microscope (BAC151B) and collected with the BWSpec software (version 4.03_23_c), by B&W Tek (Newark, DE). Excitation was obtained with a CleanLaze 785 nm laser with an output power of about 400 mW. Laser light is delivered to the sample and collected via an optical fiber probe. The Raman spectrometer uses a quantum efficiency CCD array detector with a wide spectral coverage ($65\text{-}4200\text{ cm}^{-1}$) and a spectral resolution of 2.4 cm^{-1} . Spectra collection used a 10 s CCD exposure for a single accumulation with a laser power at the sample of 50% (180 mW) and 138 mW (10%), for cAg-colloids and cAg-paper measurements, respectively. This power level has been chosen in order to avoid samples and substrates photodamage. The spot diameter at the sample was of $105\text{ }\mu\text{m}$, channeled through a 20x Olympus objective (N.A. 0.25, working distance 8.8 mm). All the substrates were placed under the microscope on a standard glass microscope slide. Paracetamol has been used as reference before and during every data collection session to account for eventual laser drifts.

8.2.3 Data analysis

Spectra have been entirely processed in the R environment [121] using *hyperSpec* [122], *baseline* [123], *ROCR* [136] and *MASS* [55] packages and other in-house developed scripts for spectra visualization.

The preprocessing steps included: (i) Raman shift range selection, (ii) baseline correction (package *baseline*, method *als*, $\lambda = 6$), (iii) vector normalization. Principal Components Analyses have been performed for explorative purpose, to highlight possible separations in the dataset and the variables which mostly account for that separation. PCA has been used for explorative analyses and the supervised classification was performed by means of PCA-LDA, with a leave-on-out cross validation.

8.3 Detailed methods, Results and Discussion

8.3.1 Breast Cancer diagnosis

8.3.1.1 Cohort of samples

To increase the sample size with respect to the preliminary data obtained by Cervo (2015), 465 samples have been recruited: 241 controls and 224 patients, included 20 cases of benign tumor. BC samples are stratified according to the incidence of available cases at the oncologic Institute, hence with unbalanced proportion among the classes. Table 8.1 reports the number of elements for each BC classes and subclasses. In some cases, subclassification was missing (i.e., biotype, stage). The median and quartiles of the age ranges are homogeneous: 56 (48-63) years old for patients, 53 (42-64) for controls, with the 1st and 3rd quartiles in brackets. This range has been selected since BC is most frequently detected in this age, which in turn matches with the start of the mammography screening.

Patients: 224 – age: 56 (48-63)		Controls: 224 – age: 53 (42-64)		Total samples: 465		
<i>Disease</i>						
Benign: 20	T. in situ: 19	Tumor: 185				
<i>Hystologic type*</i>						
Benign: 20	DCIS: 17	LCIS: 1	Lobular: 13	NST: 148	Other: 24	
<i>Biotype</i>						
Benign: 20	HER2+: 19	Luminal A like: 13	Luminal B like HER 2-: 23	Luminal B like HER2+: 16	Triple Negative: 20	Unclassified: 68
<i>Stage</i>						
Benign: 20	0: 20	I: 101	II: 48	III: 30	Unclassified: 5	

Table 8.1 Cohort composition. Each row accounts for the only classification of patients. Age expressed as median (1st quartile – 3rd quartile). *DCIS = Ductal carcinoma in situ, LCIS = Lobular carcinoma in situ, NST = no special type (invasive).

8.3.1.2 Sample collection and preparation

Serum samples have been prepared and stored by CRO-Biobank (the biobank of the CRO National Cancer Institute, Aviano, Italy), according to Cervo et al. [197]. Briefly, blood samples are collected from healthy donors and patients at the time of the first diagnosis, without any kind of chemotherapy in progress. Serum tubes (Monovette®, Sarstedt) are used for blood collection, stored at 4 °C immediately after drawing and transported to the lab in ice packed boxes. The tubes are centrifuged (10 minutes, 2680g) at room temperature and the serum fractions transferred to barcoded tubes and stored at -80 °C until the SERS analysis or different preprocessing step. Serum aliquots have been used both filtered and unfiltered. Filtration step included: thawing at room temperature, immediate centrifugal filtration (3 kDa cut-off, Amicon Ultra® 0.5 mL) at 13000g, 4 °C for 75 minutes. Samples have been thawed only one time each,

in order to limit the deterioration process described in the Background. Every deviation from the collection and storage protocol is registered on a database, together with the anthropometric parameters of the subject, like menopausal status, age, body mass index or smoking habits. For each cancer case, information on the stage, histologic type and biotype of the BC classification is registered. All the enrolled participants signed the informed consent to participate in the study. The CRO-Biobank project has been approved by the CRO Institutional Ethics Committee.

8.3.1.3 Spectra collection

Filtered serum samples have been analyzed immediately after thawing by means of cAg-colloids, (Figure 8.3). Accordingly, 5 μL of biofluids have been mixed with 45 μL of cAg-colloids (ratio 1:9Ag) and placed on a CaF_2 slide with a micropipette. Spectra have been collected on the drop after 5 minutes in order to allow a proper NPs aggregation. This delay has been established to optimize the signal to noise ratio (data not shown). Measurements have been performed only once for each sample: on one hand the overall number of available samples was limited, on the other, the intent was to provide an estimation of the diagnostic performance based on a single shot, miming the realistic use as potential point of care. The choice of the sample-to-colloid ratio (1:9Ag) accounted for the same principles. Only filtered serum aliquots have been used with colloids to avoid the protein corona formation.



Figure 8.3 Sketch of the sample preparation for spectra collection.

8.3.1.4 Breast Cancer diagnosis: Results and Discussion

A pilot study previously performed in our group demonstrated promising results in terms of BC early diagnosis working with filtered serum mixed with cAg-colloids [197]. For this reason, the analysis here reported has been performed accordingly. Among the 465 samples, the BC classes reported in Table 8.1 were not equally distributed in terms of sample size. Since classification and prediction algorithms are less biased working with balanced classes (see § 4), the first step was to merge them. Grossly, a primary classification involved the distinction between donor and patients, 241 and 224 samples, respectively. Figure 8.4 reports (a) the average spectra for the two classes and (b) the scores plots of first two components of the Principal Components Analysis (PCA). At first glance, both the lack of significant differences between the average spectra of the two classes and the scores plots are not good signs in terms of classification performance. The spectral features are the same already described in the previous Chapters, but no significant differences appear. Both classes share the same variability, in terms of standard deviation, meaning that the intraclass

variability is comparable with the interclass one. This is somewhat surprising because the preliminary measurements performed in our research group highlighted the real possibility to discriminate between controls and patients at different stage of BC. Nevertheless, at the time the number of samples was reduced to 60 samples (20 donors + 20 BC stage 0 + 20 BC stage 4) [31], and they were meticulously matched in terms of age, smoking habits and body-mass index. Hence, increasing the number of the samples reduces the metabolic distinction between healthy donors and BC patients, as inferred from the spectral data. Ultimately, increasing the number of samples only proves the intrinsic variability that each sample (and person) introduces in the class.

Body fluids evolve continuously, during the day, with diet, across the age and the gender and in presence of pathological conditions and therapeutic treatments. Metabolism changes accordingly. Inasmuch as the sample size increases, the intraclass variability increases too. A label-free approach is able to test this chaotic trend, since all the possible biomolecules that are adsorbed on cAgNPs are considered makers and a reflection of the actual metabolic profile. For this reason, two or more classes can be distinguished if and only if the peculiar metabolic conditions are separate enough, in SERS active components, to display a spectral difference. If the requirement fails, a lack of clear distinction among the groups emerges, undermining the classification. The peaks assigned to hypoxanthine and uric acids are the most intense and variable throughout the whole dataset, and greatly influences the inter-sample variability. Uric acid concentration can span the 120-400 μM range, and the value is ascribed to a number of factors, from the age, the dietary habit and lifestyle, the alcohol and smoke consumption, the use of drugs, the hormonal cycle, the presence of comorbidity and so on, beyond the effect of cancer on metabolism [110]. These aspects influence the dispersion of the composition of blood and serum in both donors and patients, and it is amplified by expanding the sample size. Moreover, sample matching in terms of age and body-mass index, both factors that are known to have an impact on the metabolic profile, was not as close as in the case of the preliminary study. In a less controlled cohort of samples (such as the ones in the case of an extensive screening study) small interclass differences can be lost among intraclass variation. PCA is a powerful tool to highlight the trend of the variable accounting for the larger variability within the system, expressed as Principal Components (PC). The first PCs retain the most variability, and as long as the PC number increases the loaded information in each one decreases, whereas the cumulative variable slowly approaches a plateau. The number of explicative variables to be retained depends on the system. It should not be too low, to lose the small but significative variations spectra always carry, but not too high to include noise, redundant information and collinearity. In this specific case, additional PCs did not introduce meaningful information or separation among the classes, at least from an explorative point of view.

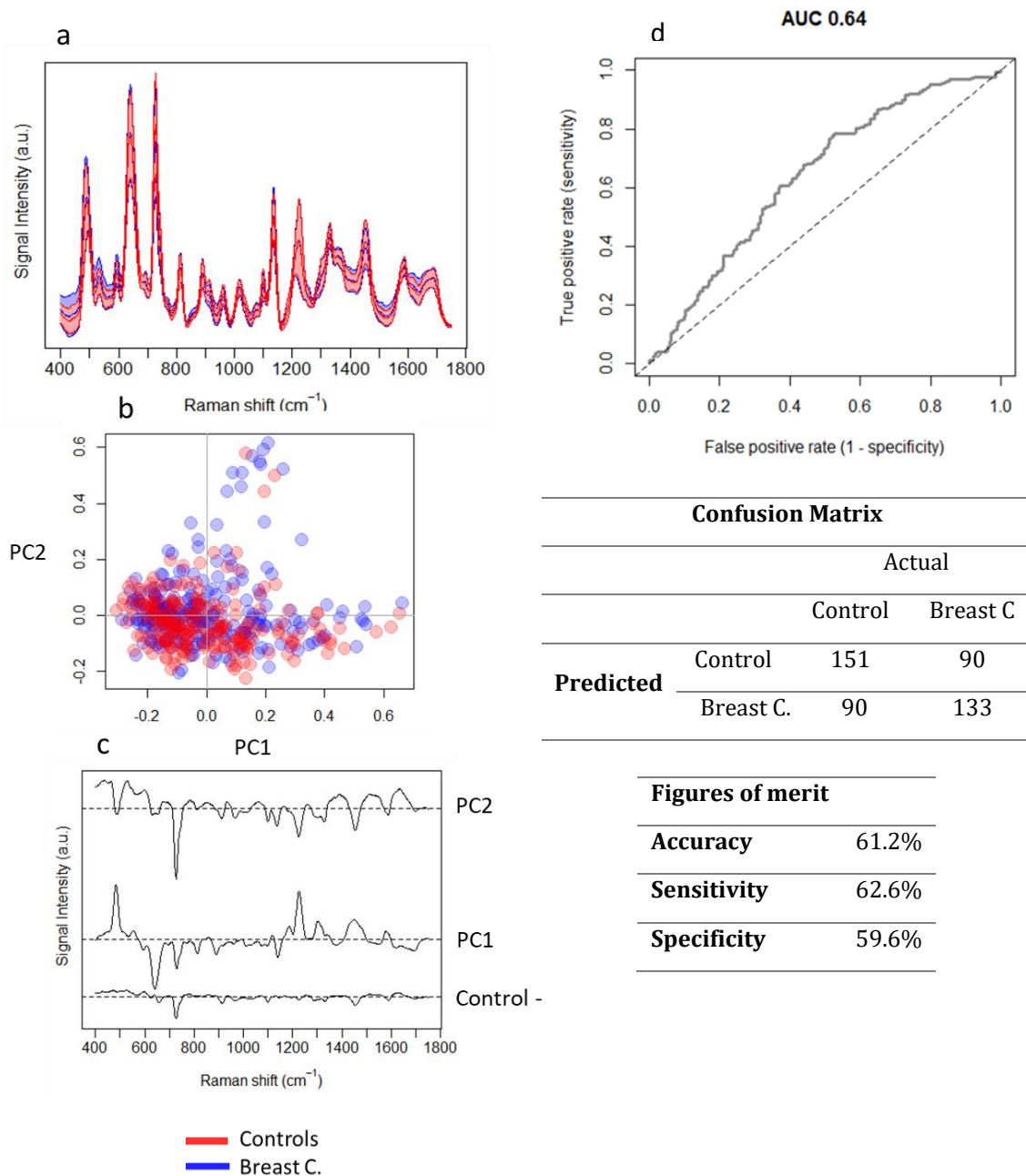


Figure 8.4 (a) Average spectra of the controls (blue) and of the patients (red) \pm standard deviation (shaded area). Laser source 785 nm, 10 seconds of acquisition time, 1 scan, 50% laser power. (b) The scatter point in the scores plot of the first three principal components are colored according to the same legend. (d) ROC curve, confusion matrix and figures of merit for the PCA-LDA classification performance for breast cancer diagnosis on filtered serum on cAg-colloids.

Classification has been tried using the combined PCA-LDA algorithm, here used for predictive modeling. The model has been trained on a part of the dataset, according to a 10-fold cross validation approach and then tested on an independent segment of the samples. The number of variables to be retained for the classification has been identified through a repeated double cross validation method on the training set, as

described in § 3. The figures of merit have been extracted from the confusion matrix reported in Figure 8.4. Label-free SERS analysis of serum samples for breast cancer identification reported an overall accuracy of 61.2%, a specificity of 59.6% and a sensitivity of 62.6%. The ROC curve (Figure 8.4 d) has an area under the curve (AUC) of 0.64. The performance is not satisfactory enough when compared to the result achieved with mammography (sensitivity 68% and specificity 75% [199]). Hence, the initial hypothesis based on the possible improvement of mammography statistics has to be rejected. These analyses on an extended data set allow us to state confidently that this label-free SERS method based on the analysis of serum, despite promising initial results, does not work to diagnose breast cancer.

The same classification procedure has been applied on the solely BC samples spectra looking at stage or histologic subclass classification. However, the result is the same or worse, and the classification performance is just slightly better than randomly guessing the class membership. Hence, the developed spectroscopic method is not able to separate clearly spectral patterns neither in the control-vs-donor case, nor among different molecular origins of the disease.

Actually, literature rarely reports studies on the effect of BC on metabolism: usually protein loading, circulating DNA fragments and gene expression are considered, all elements not easily detectable through SERS with the approach presented in this thesis. The same conclusion has been drawn for filtered and unfiltered serum on the other cAg-paper SERS substrates. Neither filtration nor substrate nature (colloids vs paper) have been able to exalt the peculiar features discriminating BC samples from healthy ones. Indeed, many other variables could have affected the sample measurements: samples treatment (freeze-thawing time and cycles), cAg nanoparticles synthesis, laser drifts, environmental conditions (temperature, humidity), order of the measurements. However, all these aspects have been carefully evaluated and randomized in order to reduce any confounding variables and bias. Of course, also preprocessing of data plays a relevant role: it is fundamental not to create artifacts that may alter the meaning of the spectra. For this reason, the effect of several parameters on the classification accuracy has been tested (baseline algorithm, number of components for classification, validation pattern), although no differences have been encountered. On the other hand, BC probably does not affect metabolism as much as supposed, or at least not enough to generate significative differences among groups. To provide a complete insight on this issue, also other label-free methods have been tested, namely the SERS analysis of filtered and unfiltered serum on cAg paper-based solid substrates and filtered serum on hydroxylamine Ag-colloids. However, no differences have been obtained with respect to the present case.

Unfortunately, the aim of this specific method has not been achieved under the chosen experimental conditions. However, three relevant messages derive from this experience:

1. Sample size really matters: whatever the trial, it is just necessary to test it on increasing sample size and verify the initial hypothesis on large numbers (following the guidelines of Beleites et al. [102], at least 80 independent samples / class). Preliminary/pilot studies are useful and necessary, but only to stimulate further research.
2. Bias reduction or removal is mandatory, and the study design has to be carefully planned, in terms of patient enrollment, sample collection and data acquisition.
3. Metabolism alterations strictly depends on the considered pathologies, and not all of them can be classified through a label-free approach, especially if the alterations are not strong enough.

The “negative” result turns out to be a relevant one. As the label-free SERS for diagnosis route is becoming more and more followed by several authors in these years, the large-scale outcome we presented here may represent a red flag over pitfalls and data misinterpretation.

8.3.2 NAFLD progression and diagnosis

8.3.2.1 Cohort of samples

The analysis of plasma samples for the early diagnosis of non-alcoholic fatty liver diseases is a proof of concept, never tested so far by Raman/SERS methods. For this reason, we opted for a pilot study, with a small sample size: 38 samples from women with NAFLD at different stage.

The age ranges and the body mass index were comparable among the classes. The stages include: (i) pure liver steatosis, (ii) liver steatosis and inflammation, (iii) early non-alcoholic steatosis hepatitis (NASH), (iv) fibrotic NASH. All the subjects gave their written informed consent before participating in this study, approved by protocol N. 22979 Local Ethical Committee (Comitato Etico Regionale Unico, FVG, SSN).

Provided all the considerations reported in the BC case, it was necessary to merge data into two classes, since the main goal is to distinguish the disease progression between the inflammatory state to the early non-alcoholic steatohepatitis. The blend turned into groups so far on called A (pure steatosis + steatosis and inflammation) and B (early NASH and fibrotic NASH), as in Table 8.2.

Group	NAFLD	No.	Gender	Age: median(quartiles)
A	Pure steatosis	9	F	53 (46 - 56)
	Steat. & Inflamm.	9	F	47 (42 - 55)
B	Early NASH	11	F	41.5 (35 - 50)
	Fibrotic NASH	9	F	46 (34 - 52)
Total		38	F	

Table 8.2 Cohort composition. Age expressed as median (1st quartile – 3rd quartile).

8.3.2.2 Sample collection and preparation

Plasma samples have been prepared and stored by the Liver Center of the University Hospital of Trieste (Italy). Briefly, blood samples were obtained by venipuncture and collected in BD Vacutainer® EDTA spray-coated tubes for plasma extraction and processed within 1 hour. The whole blood was centrifuged once at 2000g (10 minutes at 15 °C) through a density gradient medium (Ficoll-Paque PLUS, Merck, DE) added to the blood tubes which produces a stratification of the components. The plasma was carefully harvested with a pipette, transferred in another vial and centrifuged for further 5 minutes at 6000g to clarify plasma samples (4 °C). Unfiltered plasma aliquots were subsequently stored at -20 °C and thawed immediately before the SERS measurement. Part of the aliquots have been filtered to remove the protein fraction through centrifugal filtration (3 kDa Amicon Ultra 0.5 mL centrifugal filters, 14000g, 15 minutes at room temperature) and spectra were promptly collected.

All the participants in the campaign signed informed consent to participate in the study. The project has been approved by the Comitato Etico Regionale Unico del Friuli Venezia Giulia (Prot. No. 2018 Os-008-ASUITS, CINECA no. 2225).

8.3.2.3 Spectra collection

Plasma samples have been analyzed immediately after thawing following three approaches: (i) filtered plasma @ cAg-colloids, (ii) filtered plasma @ cAg-paper, (iii) unfiltered plasma @ cAg-paper (Figure 8.5). In the first case, 5 µL of biofluids have been mixed with 45 µL of cAg-colloids (ratio 1:9Ag) and placed on a CaF₂ slide with a micropipette. Spectra have been collected on the drop after 5 minutes in order to allow a proper NPs aggregation. This delay has been established to optimize the signal to noise ratio (data not shown). In the second and third cases, 5 µL of filtered or unfiltered sample was dropped on the surface of the cAg-paper substrates and let dry for about 20 minutes. After drying, the paper substrates were placed on a glass microscope slide and spectra were collected at room temperature (25 °C). Measurements have been performed in three replicas. The choice of the sample-to-colloid ratio (1:9Ag) is due to the small number of available samples. Only filtered plasma aliquots have been used with colloids to avoid the protein corona formation.

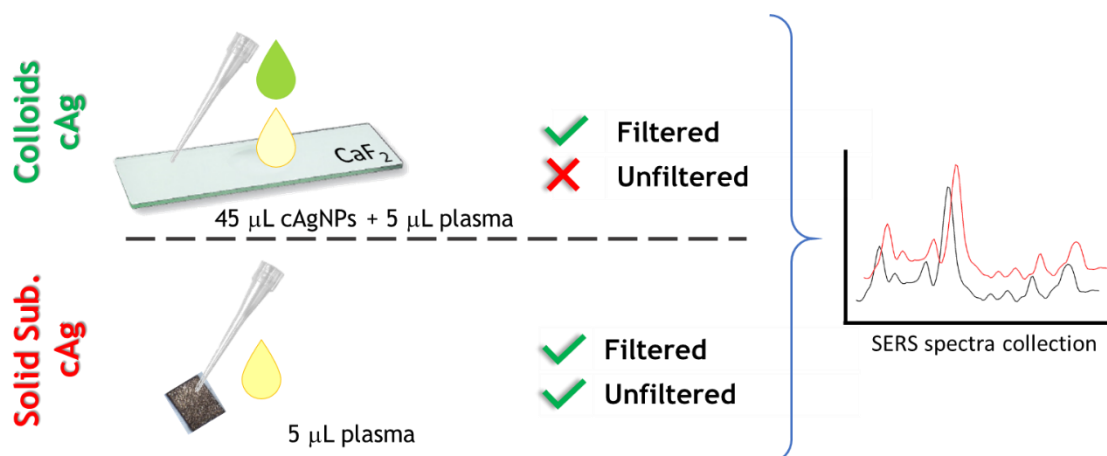


Figure 8.5 Sketch of the sample preparation for spectra collection.

8.3.2.4 Results and Discussions

Figure 8.6 reports the average spectra for the groups A and B and the differences of the mean (“B-A”) for the filtered plasma on cAg-colloids. Only these representative results are presented; the main outcome related to the other protocols can be found in Appendix 4. Spectral differences can be found all over Raman shifts, in particular in terms of relative intensities. Group A samples are characterized by a lower intensity ratio between purines (735 cm^{-1}) and uric acid bands (640 cm^{-1}), with respect to group B. Also in this case, just like in the breast cancer diagnosis campaign, the intraclass variability is significant, but lower than the differences between classes. The difference spectrum illustrates exactly the same trend, suggesting that the most severe NAFLD conditions come along with high uric acid levels. Indeed, several papers reports how the concentration of uric acid and urate increases in early NASH conditions [200], although this is not a sufficient condition for a confident diagnosis of the disease, since high uric acid levels can be related to diverse physiological or pathological conditions, irrespective of steatosis. It has been demonstrated that hyperuricemia is associated with an increased risk in NAFLD, although the role of uric acid is still ambiguous. On one hand, it is a powerful antioxidant, able to act as scavenger for oxygen radicals and to reduce the fatty liver in obese mice. Conversely, uric acid becomes a strong oxidant in metabolic syndrome environment, turning into a risk factor for NAFLD. Moreover, uric acid levels and NAFLD are associated with cardiac disease as they contribute to vascular inflammation. This is a further reason behind the need for a reliable diagnostic method for the identification of NAFLD diseases and its nature [201].

In the PCA scores, the two groups are nicely separated according to PC1 and the correspondent loading is specular to the aforementioned difference spectrum. This corroborates the hypothesis that the relative concentration of the two mainly detected analytes are discriminative with respect to the evolution of the disease. The diagnostic classification model has been built according to the PCA-LDA algorithm

previously discussed and validated with a leave-one-out approach to optimize the classifier results.

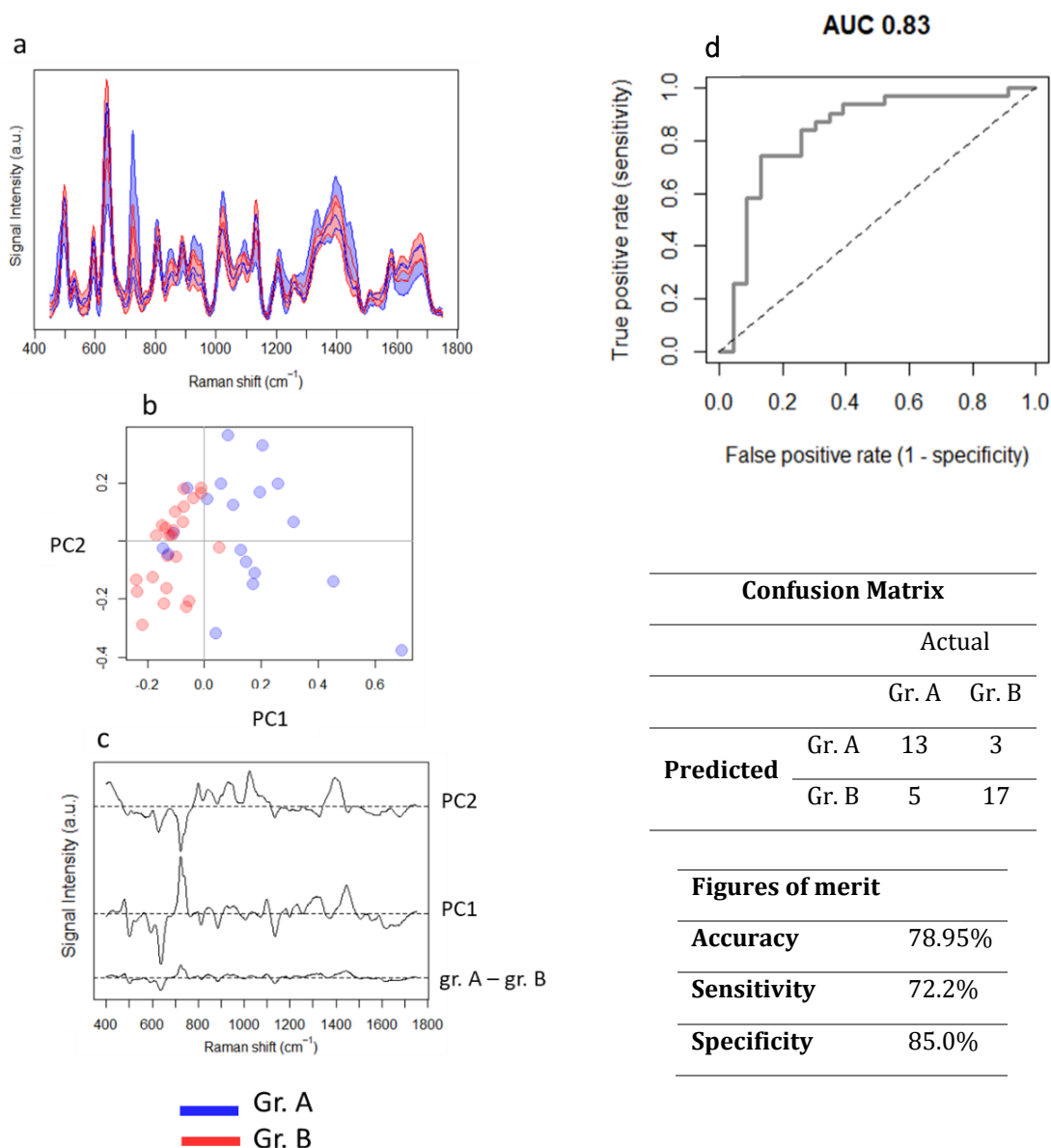


Figure 8.6 Results for plasma@cAg-colloids. (a) average spectra (± 1 standard deviation in shaded area). Laser source 785 nm, acquisition time 10s, 1 scan; (b) two of the most significant Principal Components and (c) the corresponding loadings. At the bottom, the difference spectra (Gr. A – Gr. B) reveal the same trend of the loadings of the PC; (d) ROC curve, confusion matrix and figures of merit for the PCA-LDA model.

The figures of merit have been extracted from the confusion matrix reported in Figure 8.6. Label-free SERS analysis of plasma samples for NAFLD stage discrimination reported an overall accuracy of 78.5%, a specificity of 72.2% and a sensitivity of 85%. The ROC curve (Figure 8.6 d) has an area under the curve (AUC)

of 0.83. The outcome is surprisingly good: by far, there are no similar techniques able to merge good prediction accuracy for the considered pathological conditions with a compact and fast sensing device, without the need for specific biomarkers detection. Moreover, the relative low rate of false positive and false negative encourages the hypothesis that metabolic signature detected through label-free SERS can truly open a way to a potential clinic application in the liver disease classification. Unfortunately, at the moment, the absence of a healthy control group hampers a possible extension of the approach to the early diagnosis of the diseases, but it may help in the identification of the disease evolution. It would be interesting to expand the selection of clinical cases to apparently healthy subjects, in which the presence of the disease is always late detected, being hence at higher risk.

Accordingly, the perspective of a possible robust development of the method is real, although the situation experienced with the breast cancer case definitively suggests and encourages to enlarge the sample size to obtain reliable and accurate predictions before drawing further conclusions.

8.3.3 From cirrhosis to Hepatocellular Carcinoma

8.3.3.1 Cohort of samples

In this campaign 268 subjects divided into controls and patient (both female and male) have been enrolled (Table 8.2). They are divided into two groups: 106 (82 men, 24 women) who were diagnosed with HCC, 61 (39 men, 22 women) with cirrhosis and 101 (72 men, 29 women) healthy controls. The recruitment, management and diagnosis out of the samples have been organized by the Liver Center of the University Hospital of Trieste (Italy). All the patients provided written informed consent and patient anonymity has been preserved. Investigation was conducted according to the principles expressed in the Declaration of Helsinki. The study was approved by the regional ethical committee (Comitato Etico Regionale Unico del Friuli Venezia Giulia, Prot. No. 2018 Os-008-ASUITS, CINECA no. 2225).

	Male No., age	Female No., age
Controls	72, 56 (52-60)	29, 56 (54-58)
Cirrhosis	39, 63 (57-72)	22, 69 (66.3-71)
Hepatocellular C.	82 70 (64-75)	24, 75, (73-80)
Total	193, 62 (56-72)	75, 67 (56.5-74.5)

Table 8.2 Cohort composition. Age expressed as median (1st quartile – 3rd quartile).

8.3.3.2 Sample collection and preparation

Blood drawing has been performed after overnight fasting. Serum samples have been prepared and stored by the Liver Center of the University Hospital of Trieste (Italy).

Briefly, blood samples are collected from healthy donors and patients at the time of the first diagnosis, in case of cancer, without any kind of chemotherapy in progress. Serum tubes (Vacuvette®, Greiner Bio-One GmbH, Kremsmünster Austria) are used for blood collection, stored at 4 °C immediately after drawing and transported to the lab in ice packed boxes. The tubes are centrifuged (10 minutes, 3500rpm) at room temperature and the serum fractions transferred to barcoded tubes and stored at -80 °C until the SERS analysis or different preprocessing step. Serum aliquots have been used only unfiltered.

8.3.3.3 Spectra collection

Serum samples have been analyzed immediately after thawing following only the unfiltered plasma @ cAg-paper approach (Figure 8.7). 5 μL of biofluids have been dropped on the surface of the cAg-paper substrates and let dry for about 20 minutes. After drying, the paper substrates were placed on a glass microscope slide and spectra were collected at room temperature (25 °C). Measurements have been performed in three replicas. Only unfiltered serum has been analyzed, provided the low samples volumes available.



Figure 8.7 Sketch of the sample preparation for spectra collection.

8.3.3.4 Results and Discussion

The need of an analytical method able to discriminate between two severe liver conditions, namely cirrhosis and liver tumor, is urgent and of uttermost relevance in the frame of therapy and liver transplants management. Encouraged by the positive results obtained in the NAFLD plasma analysis, the present measurement campaign means to extend the SERS actual value to another field within the liver disease diagnosis. A consideration may want to be given to the age imbalance found in the HCC cases with respect to the other. This is justified in terms of relative incidence of this type of cancer related to cirrhosis. However, a crossed comparison between age ranges and the pathological classes revealed that age does not heavily influence the spectral profile distribution. First of all, female and male subjects had to be separated and not analyzed within the same dataset. It is well known that metabolism is gender dependent too, and it would be an error not to remove this confounding factor from the analysis [202]. Provided this, the most relevant outcome shared by both genders, is the control-to-patients discriminations. Figure 8.8 reports the average spectra for controls vs cirrhosis (left) and controls vs liver tumor (right), for male subjects. The correspondent female sample plots are reported in Appendix 4 to avoid redundancy,

since the load information is comparable to the plots here presented. Just like in the NAFLD case, the spectral differences are addressed to the relative intensities for hypoxanthine or adenine and uric acid bands, although on different samples and acquisition protocol, as confirmed by the loadings in plots b and e. The difference between the average spectra of the groups (controls – cirrhosis and controls – HCC) highlights the same bands that appear in the loadings. In both cirrhosis and HCC, the uric acid concentration is higher than in the controls, and this may be associated with a strong oxidative stress and inflammation typical of the severe liver disturbs [190,193]. The predictive models based on PCA-LDA and validated through a leave-one-out cross validation process, reported different rate of accuracy, sensitivity and specificity for the two cases, as reported in Figure 8.9. For the model, the area under the ROC curve is 0.81 for the “controls vs cirrhosis” and 0.88 for the “controls vs HCC”. In general, the predictive model for the cancer case provides overall better results, compared to the cirrhosis case in which the good accuracy comes together with a substantial lack of sensitivity. This means that, for the present model, the detection rate for the true positive is poor. The results are really promising. Label-free SERS approach allows the integration of a fast, low cost and easy method for the recognition of liver disturbs also in the frame of cirrhosis and HCC. Moreover, this trial is based solely on unfiltered serum: protein may have a role in the class discrimination, as seen in the loadings (Figure 8.8 c and f), but the most relevant point is that good predictive accuracy comes along with a simplified preanalytical step. The fluid does not require filtration, but the warning about the good sample treatment is always high. This applies especially to the case in which purines levels and the relative intensity with respect to uric acid is diagnostically relevant. Literature reports papers on the use of SERS and silver NPs to perform HCC diagnosis on serum samples. Liu and co-workers (2018) reported similar alteration of the spectral profile in the cancer cases, with respect to the donors [203]. Although the band assignment is often incongruent with ours, they found some evidence in the role the peaks at 640 cm^{-1} and 730 cm^{-1} in classes differentiation. Arguably, Liu associates the reduction of the purine level in HCC to the abnormal metabolism of DNA. Indeed, this can be a reason, together with the accelerated metabolism of purines that increases the uric acid levels [202]. Nevertheless, we did observe the same alteration in cirrhotic cases and – whilst with plasma samples – in the NAFLD case of study. This demonstrates that something more is happening and the SERS substrate itself could potentially play an active role in this frame, as suggested in § 5.

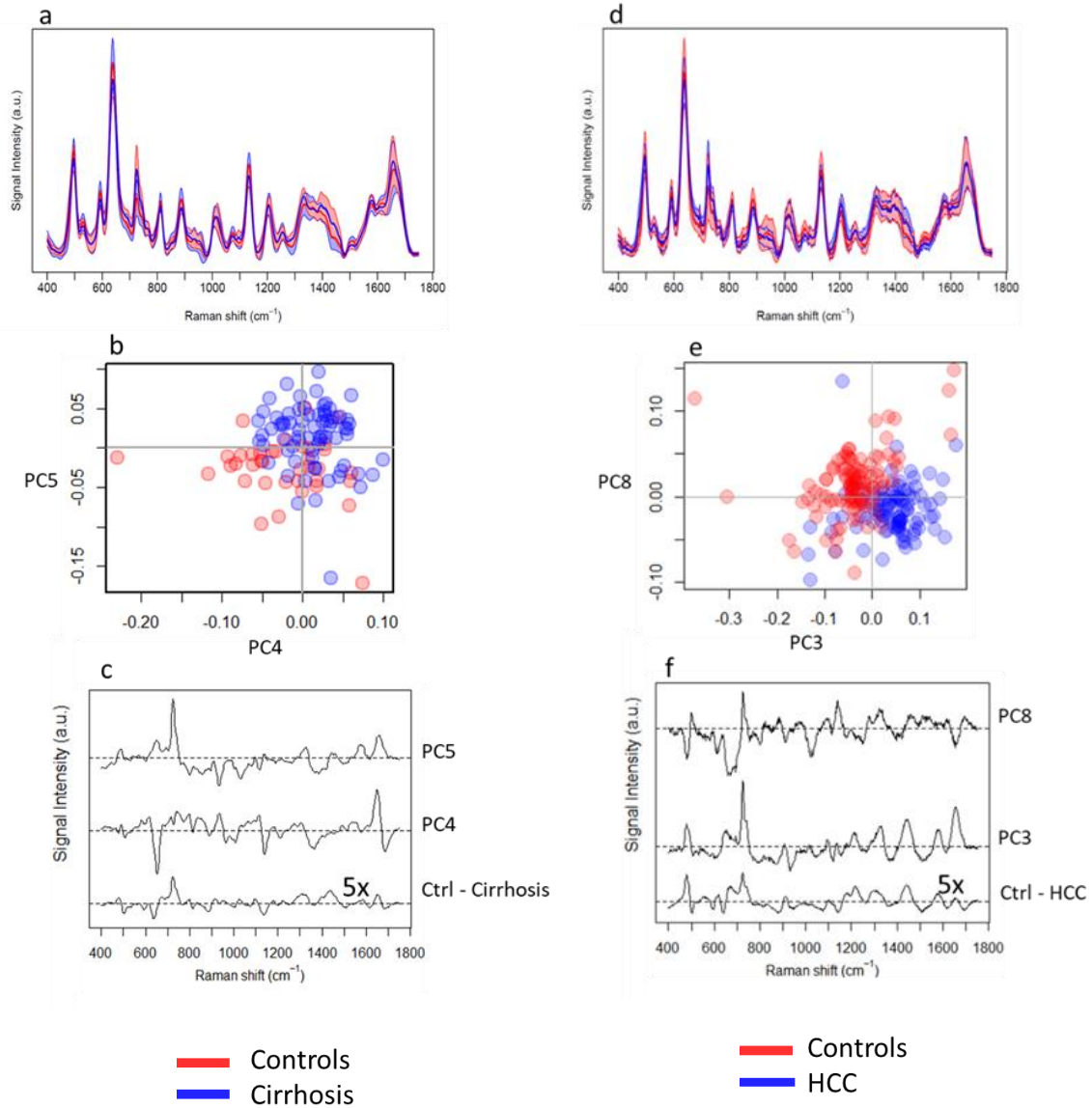


Figure 8.8 Results for serum@cAg-paper for male subjects: (left) controls vs cirrhosis, (right) controls vs hepatocellular carcinoma (HCC). (a, d) average spectra (\pm standard deviation in shaded area). Laser source 785 nm, acquisition time 10s, 1 scan; (b, e) two of the most significant Principal Components and (c, f) the corresponding loadings. At the bottom, the 5 times magnified difference spectra (Controls - Pathology) reveal the same trend of the loadings.

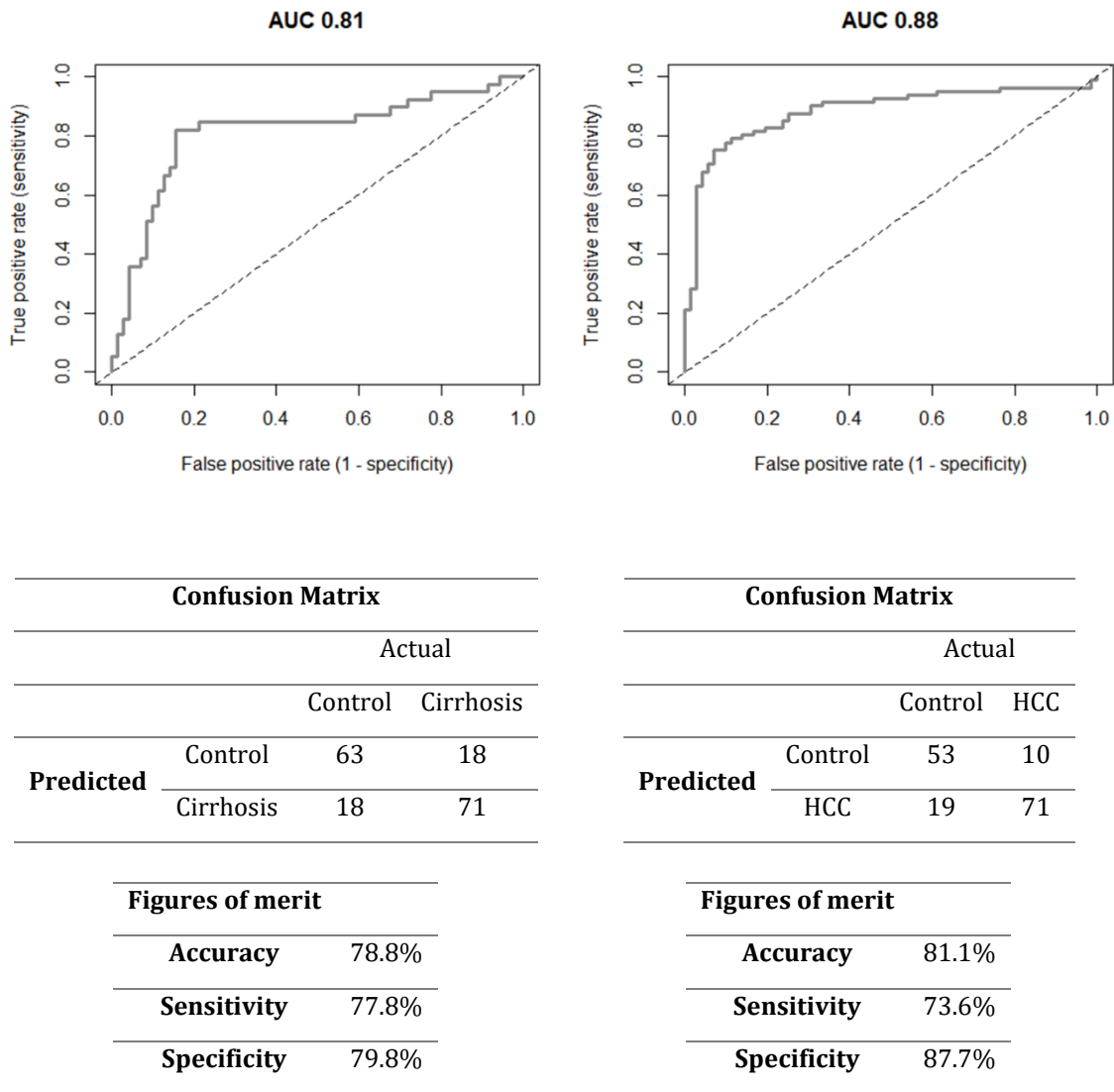


Figure 8.9 ROC curve, confusion matrix and figures of merit for the PCA-LDA model for the case of (a) controls vs cirrhosis and (b) controls vs hepatocellular carcinoma.

Unfortunately, the outcome for the cirrhosis/liver cancer comparison did not exhibit any correlations, neither with PCA, nor with multivariate prediction. This negative result can have more than one reason. For instance, the HCC samples belong to patients at the earliest stage of tumor, and the effect of the disease is probably not very evident yet. Comparisons with more advanced stages of the disease would certainly help in the characterization of the SERS potential in this field. As a last note, the differences between controls and patients in both the NAFLD and cirrhosis/HCC cases are very similar. In general, a possible explanation – to be confirmed – may regard the lack of SERS specificity for the disease of interest. SERS can be an interesting tool for the detection of metabolism alteration, irrespective of its origin. This aspect urges further insights, analyzing a larger number and type of samples, i.e.

analysis of several liver pathological conditions with the same kind of sample and procedure in order to accept or refuse this hypothesis.

8.4 Highlights:

- SERS as label-free approach toward diagnosis revealed intriguing advantages and pitfalls to be carefully evaluated before a campaign of measurements is launched. The number of involved variables and confounding factors is huge, starting from the metal substrates preparation, to the design of experiment for the sample recruitment, to the sample preparation and storage. The operative protocol must be studied in detail *a priori* and strictly followed.
- Not every biofluid is suitable for diagnostic purposes, as already stated in § 5, and, most of all, not every disease can be positively detected through SERS.
- The main obstacle in the diagnostic process on filtered serum is due to the sample size: the increasing intrinsic intraclass variability may overshadow the interclass variability, with a concomitant decrease in the diagnostic accuracy.
- The disease has to strongly impact metabolism with respect to the controls.
- For breast cancer diagnosis, the strive to find discriminative factors between healthy and pathological conditions is limited by the lack of specificity of the chosen set-up for the metabolic effects of the disease.
- Livers pathologies massively alter the metabolic pathway of a patient with respect to the control, to a different extent, depending on the pathology. Provided the lack of detection techniques for early diagnosis, label-free SERS turned out to be a promising candidate for the development of a Point of Care tool for the identification of NAFLD stages, cirrhosis and hepatocellular carcinoma.

9 Conclusions

In the pursuit of developing cutting-edge technologies in the clinical field, the dialogue between researchers and physicians is mandatory to identify the unmet clinical needs to be tackled. To date, frontiers in early detection of diseases aim at the design of simple, minimally invasive, cost effective but reliable and affordable diagnostic methods. Methods with such characteristics used to sound utopian, but these methods can soon turn into reality thanks to the recent development of electronics, plasmonic, photonics, nanotechnology and data analysis. A cocktail of science and technology that found home also in SERS. This thesis shed light on issues that must be overcome before label-free SERS can be successfully applied as a routine technique in diagnosis. In particular, the discussion articulated from the simple to the complex system, namely the model solution of protein and metabolites, the blood and its fractions up to the qualitative classification of serum and plasma samples on the basis of the spectral features. Everything seen from the label-free SERS point of view, by means of citrate reduced silver substrates.

In SERS, what can be observed depends on the peculiar binding nanoparticles-analytes. In biofluids, the mutual interaction of proteins and metabolites corona around nanoparticles can alter the spectral profile of the system according to both chemistry (including the pH and the ionic strength) and mechanics of interaction (due to size exclusion effects). When dealing with protein-rich systems, it would be good practice to evaluate how much the presence of proteins can affect the overall SERS signal compared to the protein-free system. The macromolecules removal can introduce alterations too.

The same can be said for extremely complex systems, like blood, in which we can address also to a sort of “matrix effect” that can regulate the availability of freely diffusing species. However, a lot has to be further understood about this kind of effect.

Indeed, the label-free analysis of blood under several conditions allowed to identify which fractions are better addressed to SERS analysis, provided the metabolic information they can carry. We are speaking about serum and plasma samples, which have been enrolled for the disease diagnosis section, accordingly. Plasma and serum SERS spectra are similar and display bands due to metabolites such as purines and uric acid. The metabolic profile as detected by SERS can be altered by preanalytical procedures (i.e., long waiting before the fraction separation and filtration). The main outcome is an increased hypoxanthine level due to the extracellular metabolism of purine: cellular fraction is not involved here, but filtration can stop the process, as the enzymatic fraction would be removed. Anyways, good practices are required when handling this kind of specimens, otherwise considerations on the metabolic differences between classes shall be invalid. The other side of the coin is that SERS could be successfully employed for blood sample dating. Overall, the sensor –

intended as integration between the metal nanostructured support and the Raman apparatus – play a relevant role in all the aforementioned considerations. Sample to colloids ratio, protein filtration turned out to be relevant aspects to consider during the setting up of a protocol. For instance, filtration is essential to obtain SERS spectra from colloids, but it remains an optional step for SERS on solid substrates, often avoidable to reduce the number of preanalytical steps. We have been focusing on a simple but reliable system which, of course, can be further optimized to improve the diagnostic performance

To this extent, the analysis of samples from patients with three different diseases confirmed that SERS can detect metabolic differences, provided that the pathological condition significantly alters the analyzed biofluids as far as the low molecular weight composition is concerned. Indeed, breast cancer did not cause detectable class differences or, better, the effect on metabolism is not that marked, hence the intra-class variability is overwhelmed by the inter-class one.

Of course, sample size matters: the larger the dataset, the larger the variability. Hence, it is necessary a stronger metabolome alteration to perform a classification based on the chosen experimental conditions. Nevertheless, the limits in the strive for diagnosis is probably related to the lack of specificity of the chosen set-up for the metabolic effects of the disease. Conversely, liver diseases expressed this condition and good classification performances have been retrieved also with simple classification algorithms, like PCA-LDA. Livers pathologies massively alter the metabolic pathway of a patient with respect to the control, to a different extent, depending on the pathology. However, to confirm this preliminary trial we need to go for larger dataset and more varied system, to mimic a realistic diagnostic pattern.

Indeed, a well build design of experiment is truly the greater part of the analysis

As a note, literature often shares promising results in terms of diagnostic performance with SERS on biofluids. As this thesis reported, the reader should beware of enthusiastic conclusions and always consider the design of experiments, as conclusions reached on small sample size are hardly reproduced on a large scale.

The conclusion is that if “the simpler the better”, referring to the SERS substrates in use, extra care is required when dealing with complex systems. For this reason, we aim to further develop the proposed method and to structure it into a real applicative Point of Care device, not forgetting the huge role the fundamental research plays in the field. More than this, the same implementation can be done in other areas, from agro-food, to pharma. Nevertheless, our study should encourage researchers to put their efforts in this promising technique, which is a premise for non-invasive, cost-effective, and fast diagnosis processes.

Acknowledgements

To my family and friends.

I would like to genuinely express my gratitude to my advisors, Professor Valter Sergo and Professor Alois Bonifacio, for having me in their group and for the support and care. This voyage revealed to be truly non-linear. Thank you, because, above all, it has been like feeling at home.

My acknowledgments are devoted also to the institutions that provided us all the clinical samples analyzed in these years and a great scientific support: Dr. Riccardo Spizzo and Dr. Silvia Cervo on behalf of Centro di Riferimento Oncologico in Aviano (UD), and Professor Claudio Tiribelli, Dr. Devis Pascut, Dr. Pablo Giraudi, Dr. Natalia Rosso on behalf of the Fondazione Italiana Fegato – Onlus in Trieste.

My sincere thanks also go to my lab fellows, Dr. Alessia Di Silvestre, Dr. Elisa Mitri, Dr. Stefano Fornasaro, who shared with me their knowledge and support.

Not least all the friends I've met along these years: Sabrina, Barbara, Federica, Rita, Marco, Caterina and Irene, Lucia, Alessio, Luca, Odeta, for having helped me in any possible way, Ilaria and Alessia for the 373 suffered shared moments. All these people are characterized by rare qualities: integrity, honesty, passion, audacity. Thank you for having shared all of them with me. Most of these are women in science and I wish them a bright future of personal and professional fulfillment.

Now the most important thanks and love go to my family, mum, dad, my sister Elena, my grandfather and my uncles. Always with me, although I couldn't have been with them as much as I'd love to. Thank you for having always believed in me, no matter what. I hope I could repay you for all your sacrifice someday. Elena, you are the best I could've ever wished for! :) Last but not least, my complete gratitude and love to Tommaso, who shared these years with me, the first but not the only.

Thank you all for your support and friendship!

Appendix 1

List of reagents

<i>Reagent</i>	<i>Grade of purity</i>	<i>Producer</i>	<i>CAS</i>
Laboratory glassware washing			
NoChromix®	N.A.	Merck	328693
Sulfuric Acid 95-97 %	Puriss.p.a	Merck	7664-93-3
Nitric Acid > 65 %	Puriss.p.a	Merck	7697-37-2
Nanoparticles Synthesis			
Sodium Citrate Tribasic	≥ 99 %	Merck	6132-04-3
Silver Nitrate	≥ 99.0 %	Merck	7761-88-8
Hydroxylamine Hydrochloride	99.999%	Merck	5470-11-1
Sodium Chloride	ACS	Merck	7647-14-5
Metabolite Solutions			
Phosphate buffered saline (tablets)	N.A.	Merck	Sigma-P4417
Sodium hydroxide	ACS	Merck	1310-73-2
Adenine	≥ 99 %	Merck	73-24-5
Hypoxanthine	≥ 99 %	Merck	68-94-0
Uric acid	≥ 99 %	Merck	69-93-2
Human serum albumine	≥ 98 %	Merck	70024-90-7
Blood treatment			
Ficoll® Paque Plus	N.A.	Merck	N.A.

MilliQ water (grade 1, Merck, DE) has been used for all the preparations.

Appendix 2

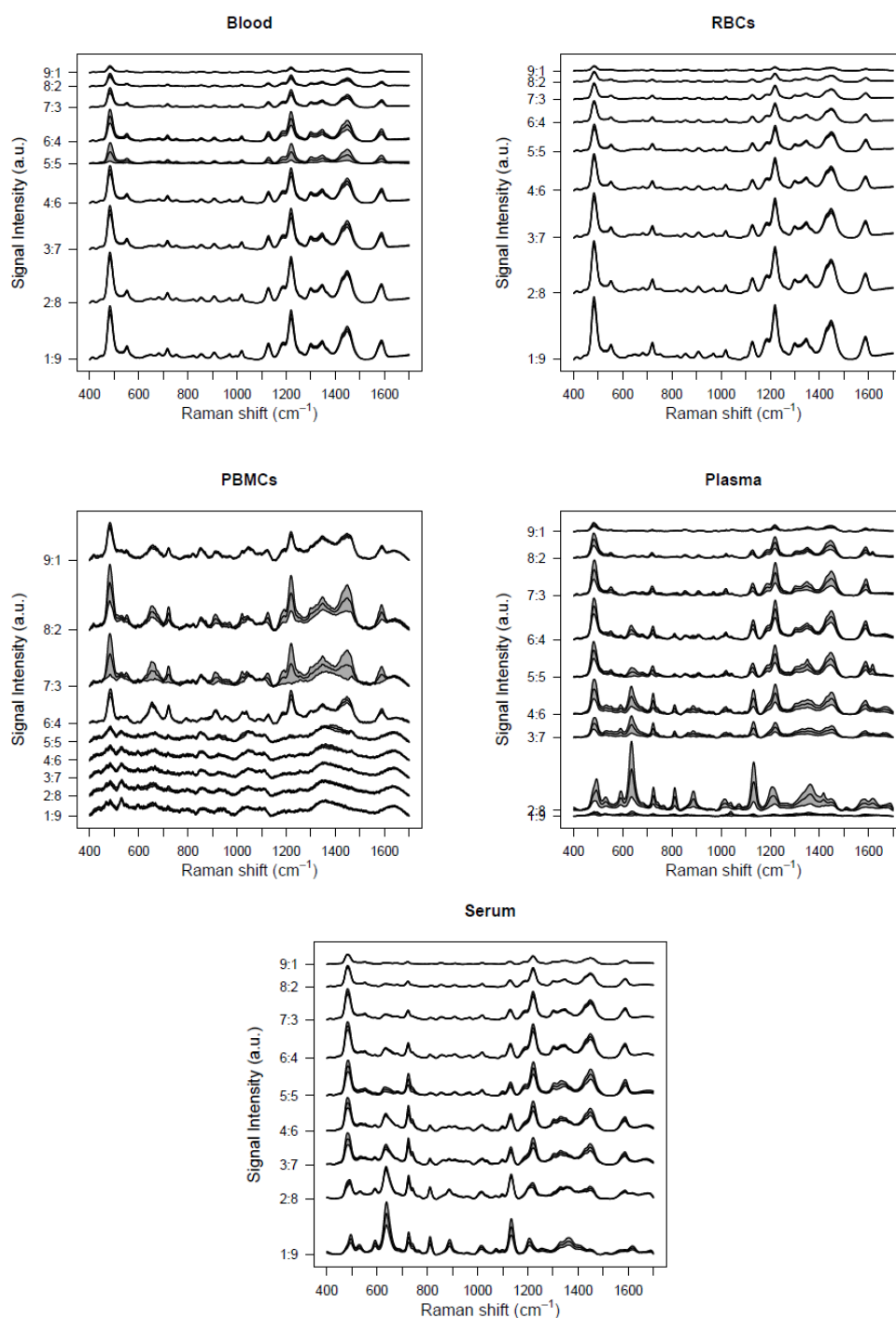


Figure A.2.1 Effect of the silver colloid dilution on filtered blood, RBCs, PBMCs, serum and plasma. Measurements have been acquired with the 785 nm laser; data are vector normalized and reported as mean \pm 1 standard deviation (shaded area) of several independent replica.

PBMCs show a different trend with respect to the other blood fractions: almost no significant signals are visible in the more diluted conditions (from 3:2Ag to 1:9Ag) while intense spectra appear at higher concentrations of sample in the colloid. A possible explanation may be found in the limit of detection of the PBMCs themselves with cAg-colloids, as they may require a higher sample to NPs ratio to provide a SERS signal. It is worth remembering that the PBMCs samples were lysed with a 1:4 proportion in MilliQ water, four times more than all the other blood fractions (see the sample preparation section).

The case of plasma is peculiar since no peak is visible in the most diluted sample (1:9Ag), whereas the spectra from the 1:4Ag ratio on are much more defined and intense. In analogy with the PBMCs case, it can be speculated that the 1:9Ag condition would be too diluted to provide SERS signals, whereas a turnaround is seen with the subsequent dilutions. The result has been confirmed with several replica, and other explanations are still unclear.

Appendix 3

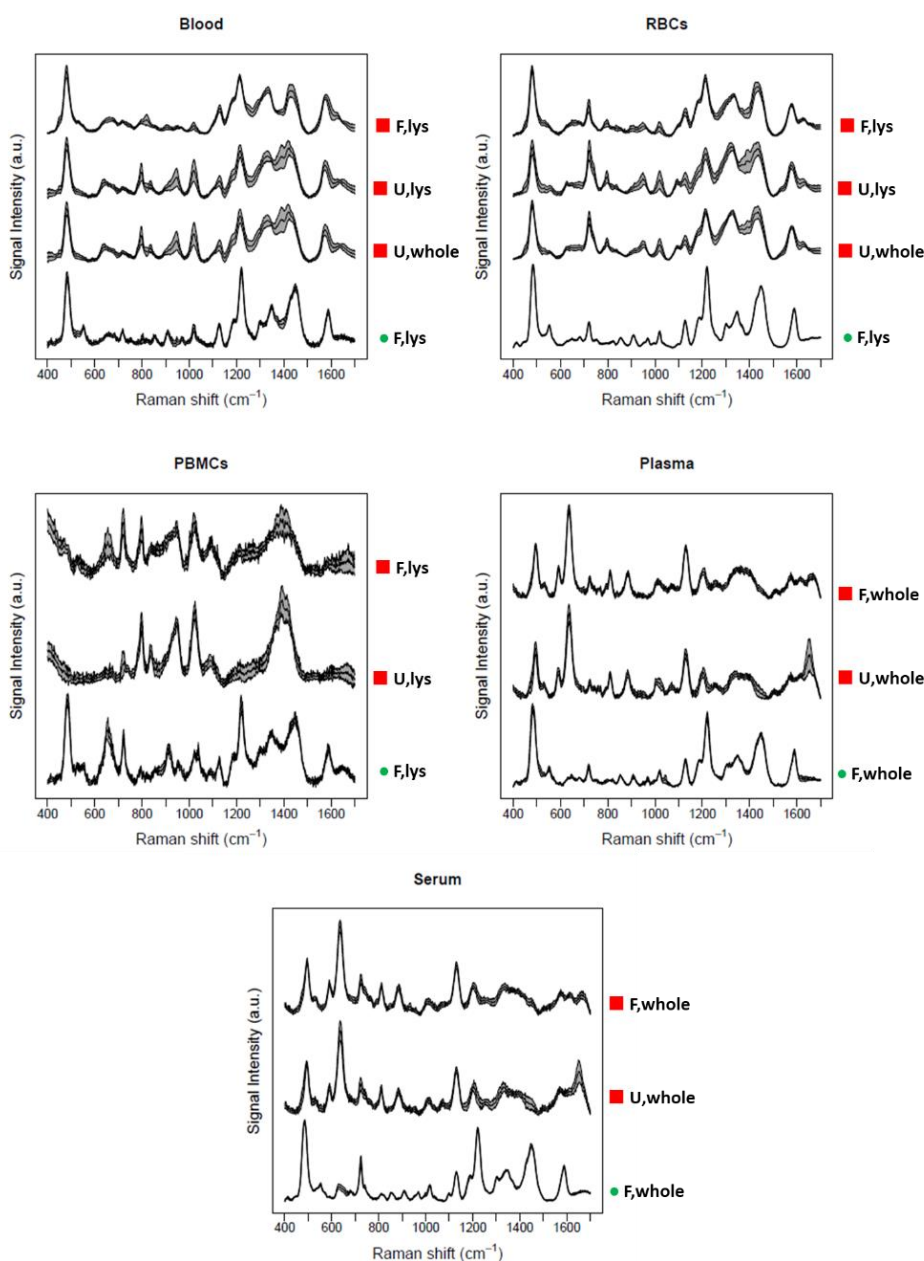


Figure A.3.1 Effect of lysis and filtration.

■ = paper-based cAg substrate; ● = cAg colloid; U = unfiltered; F = filtered; lys = lysed; whole = not lysed. Measurements have been acquired with the 785 nm laser; data are vector normalized and reported as mean \pm 1 standard deviation (shaded area) of several independent replica. For the sake of comparison, only the 1:1Ag ratio filtered biofluids-to-colloids mixture are reported (except for PBMC, in 3:2Ag ratio), without prejudice to the considerations set in Par. 4.2.8.

As a note, several spectra report a strong signature of the citrate ions belonging to the cAg background which are not of our interest; however, this reveals an incomplete saturation of the metal surface with the analytes under exam. In particular, unfiltered blood, RBCs and PBMCs show citrate bands at 796 cm^{-1} , 836 cm^{-1} , 940 cm^{-1} and 1020 cm^{-1} (citrate spectrum reported below)

PBMCs, again, show a peculiar behavior: their initial concentration is four times lower than all the other cases and this is reflected in less intense spectra visible through a poor signal-to-noise ratio and the predominance of the citrate bands, in particular for the unfiltered PBMCs when lysed (and further diluted) and on cAg-paper. In this case, PBMCs do not feature the 485 cm^{-1} band so far discussed and not even the uric acid bands. Filtration apparently increases the concentration of these two species, which appear in both the cAg-paper and, mostly, in the cAg-colloids cases.

Plasma and serum show very similar profiles in all the conditions and lysis seems to not alter the overall SERS profile with cAg-paper. The differences with the cAg-colloids case mainly regard the uric acid peaks, almost absent in the cAg-colloids case: the behavior reflects and strictly depends on what has already been seen in the previous paragraph in terms of sample-to-NPs ratio, here 5:5 in volume. The reader is addressed back to Par. 4.2.8 in this regard.

Surprisingly, the behavior of the whole blood spectra, irrespective of sample processing, mainly follows that of the RBCs, and the plasma or serum metabolites do not play any significant role in this respect. Nevertheless, the sample concentration requires to be adjusted in order to avoid any interferences due to the SERS substrates background (i.e., sodium citrate). However, whole blood and intact RBCs revealed to be not perfectly suitable for SERS analysis on our solid paper-based substrates: they require additional washing steps before the measurements to remove the heme fraction, otherwise the red 785 nm laser would photodamage the sample also with low source power.

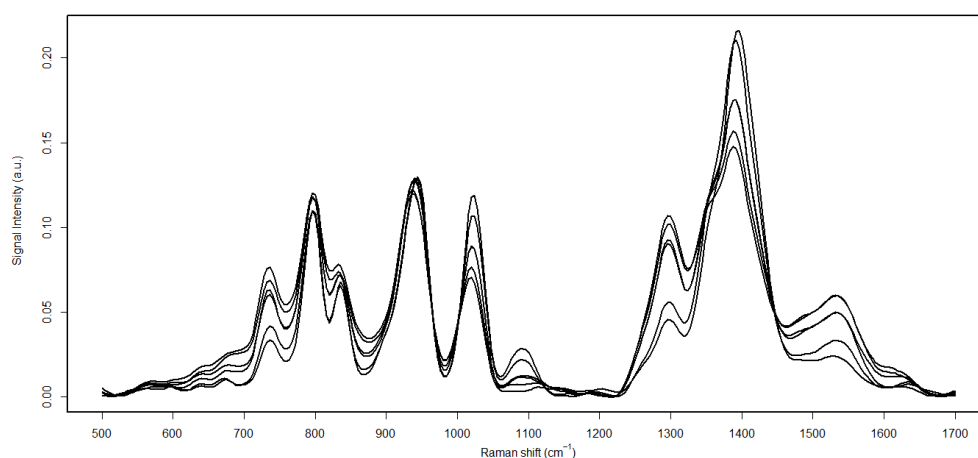
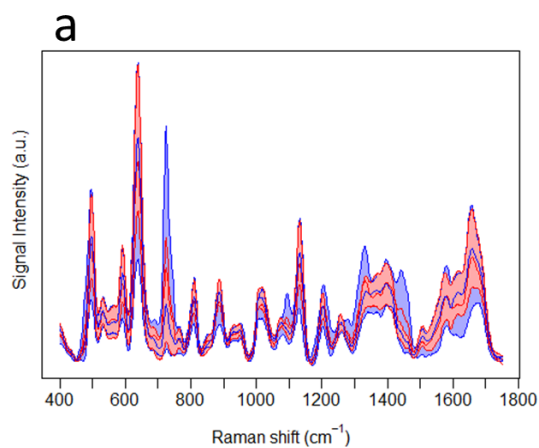


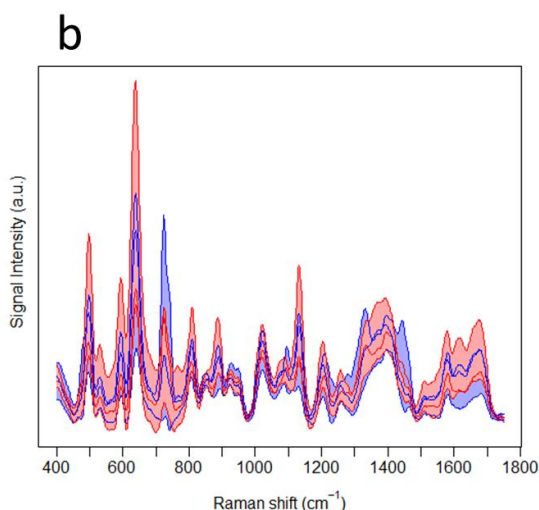
Figure A.3.2 Citrate on paper-based cAg substrate. Six normalized spectra.

Appendix 4



Confusion Matrix			
		Actual	
		Gr. A	Gr. B
Predicted	Gr. A	7	3
	Gr. B	10	18

Figures of merit	
Accuracy	65.8%
Sensitivity	41.1%
Specificity	85.0%



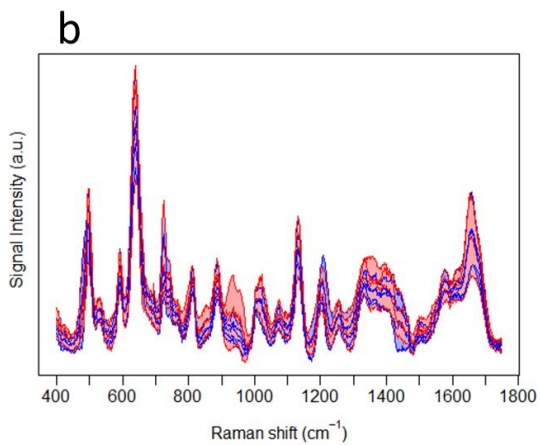
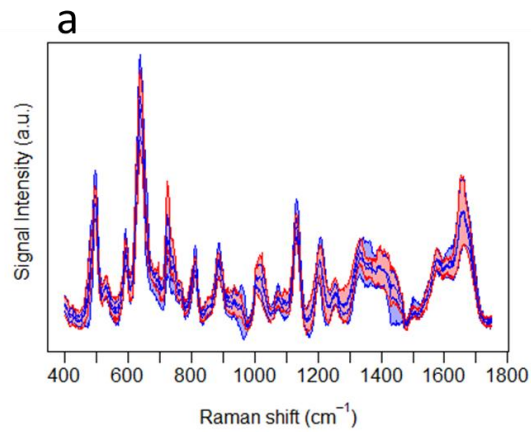
Confusion Matrix			
		Actual	
		Gr. A	Gr. B
Predicted	Gr. A	10	1
	Gr. B	7	20

Figures of merit	
Accuracy	78.9%
Sensitivity	58.8%
Specificity	95.2%

Figure A.4.1 SERS on plasma @ cAg-paper: non-alcoholic fatty liver diseases.

(Left) average spectra for the (a) unfiltered plasma@cAg-paper and (b) filtered plasma@cAg-paper, and (right) correspondent confusion matrices and figures of merit. All the protocols suffer of low sensitivity but show promising results in terms of accuracy and specificity. The paper-based SERS substrates are interesting starting points towards the Point of Care development.

Appendix 5



Confusion Matrix			
		Actual	
		Ctrl	Cirrh.
Predicted	C	15	5
	Cirrh.	6	21

Figures of merit	
Accuracy	76.6%
Sensitivity	71.4%
Specificity	80.8%

Confusion Matrix			
		Actual	
		Ctrl.	HCC
Predicted	Ctrl.	19	7
	HCC	5	22

Figures of merit	
Accuracy	77.4%
Sensitivity	79.1%
Specificity	75.8%

Figure A.5.1 Female samples: Cirrhosis and Hepatocellular Carcinoma, serum@cAg-paper. (Left) average spectra for the unfiltered serum@cAg-paper (a) “control vs cirrhosis” and (b) “controls vs HCC” and (right) correspondent confusion matrices and figures of merit.

References

- [1] Ahmed M U, Saaem I, Wu P C and Brown A S 2014 Personalized diagnostics and biosensors: a review of the biology and technology needed for personalized medicine *Crit. Rev. Biotechnol.* **34** 180–96
- [2] Dietel M and Sers C 2006 Personalized medicine and development of targeted therapies: The upcoming challenge for diagnostic molecular pathology. A review *Virchows Arch.* **448** 744–55
- [3] Kalia M 2013 Personalized oncology: Recent advances and future challenges *Metabolism* **62** S11–4
- [4] Myers F B and Lee L P 2008 Innovations in optical microfluidic technologies for point-of-care diagnostics *Lab Chip* **8** 2015–31
- [5] Gubala V, Harris L F, Ricco A J, Tan M X and Williams D E 2012 Point of Care Diagnostics: Status and Future *Analytical Chemistry* **84** 487–515
- [6] Tokel O, Inci F and Demirci U 2014 Advances in Plasmonic Technologies for Point of Care Applications *Chemical Reviews* **114** 5728–52
- [7] Van Heertum R L, Scarimbolo R, Ford R, Berdough E and O’Neal M 2015 Companion diagnostics and molecular imaging-enhanced approaches for oncology clinical trials *Drug Des Devel Ther* **9** 5215–23
- [8] Chin C D, Linder V and Sia S K 2012 Commercialization of microfluidic point-of-care diagnostic devices *Lab Chip* **12** 2118–34
- [9] Weigl B H, Gaydos C A, Kost G, Beyette F R, Sabourin S, Rompalo A, de los Santos T, McMullan J T and Haller J 2012 The Value of Clinical Needs Assessments for Point-of-Care Diagnostics: *Point of Care: The Journal of Near-Patient Testing & Technology* **11** 108–13
- [10] Alvarez-Puebla R A and Liz-Marzán L M 2010 SERS-Based Diagnosis and Biodetection *Small* **6** 604–10
- [11] Sha M Y, Xu H, Penn S G and Cromer R 2007 SERS nanoparticles: a new optical detection modality for cancer diagnosis *Nanomedicine (Lond)* **2** 725–34
- [12] Wang X-P, Walkenfort B, König M, König L, Kasimir-Bauer S and Schlücker S 2017 Fast and reproducible iSERS microscopy of single HER2-positive breast cancer cells using gold nanostars as SERS nanotags *Faraday Discuss.* **205** 377–86
- [13] Lane L A, Qian X and Nie S 2015 SERS Nanoparticles in Medicine: From Label-Free Detection to Spectroscopic Tagging *Chem. Rev.* **115** 10489–529
- [14] Schlücker S 2014 Surface-Enhanced Raman Spectroscopy: Concepts and Chemical Applications *Angewandte Chemie International Edition* **53** 4756–95

- [15] Sharma B, Frontiera R R, Henry A-I, Ringe E and Van Duyne R P 2012 SERS: Materials, applications, and the future *Materials Today* **15** 16–25
- [16] Granger J H, Granger M C, Firpo M A, Mulvihill S J and Porter M D 2013 Toward development of a surface-enhanced Raman scattering (SERS)-based cancer diagnostic immunoassay panel *The Analyst* **138** 410–6
- [17] Lee S, Chon H, Lee J, Ko J, Chung B H, Lim D W and Choo J 2014 Rapid and sensitive phenotypic marker detection on breast cancer cells using surface-enhanced Raman scattering (SERS) imaging *Biosens Bioelectron* **51** 238–43
- [18] Lee S, Kim S, Choo J, Shin S Y, Lee Y H, Choi H Y, Ha S, Kang K and Oh C H 2007 Biological imaging of HEK293 cells expressing PLCgamma1 using surface-enhanced Raman microscopy *Anal. Chem.* **79** 916–22
- [19] Stefanacu A, Moisoiu V, Couti R, Andras I, Rahota R, Crisan D, Pavel I E, Socaciu C, Leopold N and Crisan N 2018 Combining SERS analysis of serum with PSA levels for improving the detection of prostate cancer *Nanomedicine* **13** 2455–67
- [20] Wang B, Chen D, Chen Y, Hu Z, Cao M, Xie Q, Chen Y, Xu J, Zheng S and Li L 2012 Metabonomic profiles discriminate hepatocellular carcinoma from liver cirrhosis by ultraperformance liquid chromatography-mass spectrometry *J. Proteome Res.* **11** 1217–27
- [21] Crawford B M, Wang H-N, Fales A M, Bowie M L, Seewaldt V L and Vo-Dinh T 2017 SERS-based inverse molecular sentinel (iMS) nanoprobe for multiplexed detection of microRNA cancer biomarkers in biological samples Society of Photo-Optical Instrumentation Engineers (SPIE) Conference Series vol 0080 p 1008008
- [22] Haldavnekar R, Venkatakrishnan K and Tan B 2018 Non plasmonic semiconductor quantum SERS probe as a pathway for in vitro cancer detection *Nature Communications* **9** 3065
- [23] Kneipp K, Kneipp H, Kartha V B, Manoharan R, Deinum G, Itzkan I, Dasari R R and Feld M S 1998 Detection and identification of a single DNA base molecule using surface-enhanced Raman scattering (SERS) *Physical Review E* **57** R6281–4
- [24] Bell S E J and Sirimuthu N M S 2006 Surface-enhanced Raman spectroscopy (SERS) for sub-micromolar detection of DNA/RNA mononucleotides *J. Am. Chem. Soc.* **128** 15580–1
- [25] Kang T, Yoo S M, Yoon I, Lee S Y and Kim B 2010 Patterned Multiplex Pathogen DNA Detection by Au Particle-on-Wire SERS Sensor *Nano Letters* **10** 1189–93
- [26] Cao Y C, Jin R and Mirkin C A 2002 Nanoparticles with Raman spectroscopic fingerprints for DNA and RNA detection *Science* **297** 1536–40
- [27] Driskell J D and Tripp R A 2010 Label-free SERS detection of microRNA based on affinity for an unmodified silver nanorod array substrate *Chemical Communications* **46** 3298

- [28] Guerrini L, Krpetić Ž, van Lierop D, Alvarez-Puebla R A and Graham D 2015 Direct Surface-Enhanced Raman Scattering Analysis of DNA Duplexes *Angewandte Chemie International Edition* **54** 1144–8
- [29] Piunno P A E and Krull U J 2005 Trends in the development of nucleic acid biosensors for medical diagnostics *Analytical and Bioanalytical Chemistry* **381** 1004–11
- [30] Bonifacio A, Dalla Marta S, Spizzo R, Cervo S, Steffan A, Colombatti A and Sergo V 2014 Surface-enhanced Raman spectroscopy of blood plasma and serum using Ag and Au nanoparticles: a systematic study *Anal Bioanal Chem* **406** 2355–65
- [31] Cervo S, Mansutti E, Del Mistro G, Spizzo R, Colombatti A, Steffan A, Sergo V and Bonifacio A 2015 SERS analysis of serum for detection of early and locally advanced breast cancer *Anal Bioanal Chem* **407** 7503–9
- [32] Premasiri W R, Clarke R H and Womble M E 2001 Urine analysis by laser Raman spectroscopy *Lasers Surg Med* **28** 330–4
- [33] Premasiri W R, Lee J C and Ziegler L D 2012 Surface-Enhanced Raman Scattering of Whole Human Blood, Blood Plasma, and Red Blood Cells: Cellular Processes and Bioanalytical Sensing *The Journal of Physical Chemistry B* **116** 9376–86
- [34] Jarvis R M and Goodacre R 2008 Characterisation and identification of bacteria using SERS *Chem Soc Rev* **37** 931–6
- [35] Lin D, Feng S, Huang H, Chen W, Shi H, Liu N, Chen L, Chen W, Yu Y and Chen R 2014 Label-Free Detection of Blood Plasma Using Silver Nanoparticle Based Surface-Enhanced Raman Spectroscopy for Esophageal Cancer Screening *Journal of Biomedical Nanotechnology* **10** 478–84
- [36] Bonifacio A, Cervo S and Sergo V 2015 Label-free surface-enhanced Raman spectroscopy of biofluids: Fundamental aspects and diagnostic applications *Analytical and bioanalytical chemistry* **407** 8265–77
- [37] Tran C D 1984 Subnanogram detection of dyes on filter paper by surface-enhanced Raman scattering spectrometry *Analytical Chemistry* **56** 824–6
- [38] Peng F, Su Y, Zhong Y, Fan C, Lee S-T and He Y 2014 Silicon nanomaterials platform for bioimaging, biosensing, and cancer therapy *Acc. Chem. Res.* **47** 612–23
- [39] Song J, Duan B, Wang C, Zhou J, Pu L, Fang Z, Wang P, Lim T T and Duan H 2014 SERS-encoded nanogapped plasmonic nanoparticles: growth of metallic nanoshell by templating redox-active polymer brushes *J. Am. Chem. Soc.* **136** 6838–41
- [40] Ouyang L, Hu Y, Zhu L, Cheng G J and Irudayaraj J 2017 A reusable laser wrapped graphene-Ag array based SERS sensor for trace detection of genomic DNA methylation *Biosens Bioelectron* **92** 755–62

- [41] Reza K K, Dey S, Wuethrich A, Sina A A I, Korbie D, Wang Y and Trau M 2018 Parallel profiling of cancer cells and proteins using a graphene oxide functionalized ac-EHD SERS immunoassay *Nanoscale* **10** 18482–91
- [42] Lin D, Qin T, Wang Y, Sun X and Chen L 2014 Graphene oxide wrapped SERS tags: multifunctional platforms toward optical labeling, photothermal ablation of bacteria, and the monitoring of killing effect *ACS Appl Mater Interfaces* **6** 1320–9
- [43] Ren W, Fang Y and Wang E 2011 A binary functional substrate for enrichment and ultrasensitive SERS spectroscopic detection of folic acid using graphene oxide/Ag nanoparticle hybrids *ACS Nano* **5** 6425–33
- [44] Xin W, Yang J-M, Li C, Goorsky M S, Carlson L and De Rosa I M 2017 Novel Strategy for One-Pot Synthesis of Gold Nanoplates on Carbon Nanotube Sheet As an Effective Flexible SERS Substrate *ACS Applied Materials & Interfaces* **9** 6246–54
- [45] Zhou Q, Zheng J, Qing Z, Zheng M, Yang J, Yang S, Ying L and Yang R 2016 Detection of Circulating Tumor DNA in Human Blood via DNA-Mediated Surface-Enhanced Raman Spectroscopy of Single-Walled Carbon Nanotubes *Anal. Chem.* **88** 4759–65
- [46] Jones S, Pramanik A, Kanchanapally R, Viraka Nellore B P, Begum S, Sweet C and Ray P C 2017 Multifunctional Three-Dimensional Chitosan/Gold Nanoparticle/Graphene Oxide Architecture for Separation, Label-Free SERS Identification of Pharmaceutical Contaminants, and Effective Killing of Superbugs *ACS Sustainable Chemistry & Engineering* **5** 7175–87
- [47] Boca S C, Potara M, Gabudean A-M, Juhem A, Baldeck P L and Astilean S 2011 Chitosan-coated triangular silver nanoparticles as a novel class of biocompatible, highly effective photothermal transducers for in vitro cancer cell therapy *Cancer Lett.* **311** 131–40
- [48] Boca-Farcau S, Potara M, Simon T, Juhem A, Baldeck P and Astilean S 2014 Folic acid-conjugated, SERS-labeled silver nanotriangles for multimodal detection and targeted photothermal treatment on human ovarian cancer cells *Mol. Pharm.* **11** 391–9
- [49] Kurokawa Y and Imai Y 1991 Surface-enhanced Raman scattering (SERS) using polymer (cellulose acetate and Nafion) membranes impregnated with fine silver particles *Journal of Membrane Science* **55** 227–33
- [50] Maiti K K, Dinish U S, Fu C Y, Lee J-J, Soh K-S, Yun S-W, Bhuvaneshwari R, Olivo M and Chang Y-T 2010 Development of biocompatible SERS nanotag with increased stability by chemisorption of reporter molecule for in vivo cancer detection *Biosens Bioelectron* **26** 398–403
- [51] Dalla Marta S, Novara C, Giorgis F, Bonifacio A and Sergio V 2017 Optimization and Characterization of Paper-Made Surface Enhanced Raman Scattering (SERS) Substrates with Au and Ag NPs for Quantitative Analysis *Materials* **10** 1365

- [52] Smith E and Dent G 2004 *Modern Raman Spectroscopy - A Practical Approach: Smith/Modern Raman Spectroscopy - A Practical Approach* (Chichester, UK: John Wiley & Sons, Ltd)
- [53] Raman C V and Krishnan K S 1928 A New Type of Secondary Radiation *Nature* **121** 501–2
- [54] Smekal A 1923 Zur Quantentheorie der Dispersion *Naturwissenschaften* **11** 873–5
- [55] Venables W N and Ripley B D 2002 *Modern Applied Statistics with S* (New York, USA)
- [56] Smith W E 2008 Practical understanding and use of surface enhanced Raman scattering/surface enhanced resonance Raman scattering in chemical and biological analysis *Chem. Soc. Rev.* **37** 955–64
- [57] Cialla D, März A, Böhme R, Theil F, Weber K, Schmitt M and Popp J 2012 Surface-enhanced Raman spectroscopy (SERS): progress and trends *Anal Bioanal Chem* **403** 27–54
- [58] Matousek P, Towrie M, Stanley A and Parker A W 1999 Efficient Rejection of Fluorescence from Raman Spectra Using Picosecond Kerr Gating *Appl. Spectrosc., AS* **53** 1485–9
- [59] Le Ru E C, Blackie E, Meyer M and Etchegoin P G 2007 Surface Enhanced Raman Scattering Enhancement Factors: A Comprehensive Study *The Journal of Physical Chemistry C* **111** 13794–803
- [60] Campion A and Kambhampati P 1998 Surface-enhanced Raman scattering *Chem. Soc. Rev.* **27** 241–50
- [61] Fleischmann M, Hendra P J and McQuillan A J 1974 Raman spectra of pyridine adsorbed at a silver electrode *Chemical Physics Letters* **26** 163–6
- [62] Bantz K C, Meyer A F, Wittenberg N J, Im H, Kurtuluş Ö, Lee S H, Lindquist N C, Oh S-H and Haynes C L 2011 Recent progress in SERS biosensing *Physical Chemistry Chemical Physics* **13** 11551
- [63] Jeanmaire D L and Van Duyne R P 1977 Surface raman spectroelectrochemistry: Part I. Heterocyclic, aromatic, and aliphatic amines adsorbed on the anodized silver electrode *Journal of Electroanalytical Chemistry and Interfacial Electrochemistry* **84** 1–20
- [64] Albrecht M G and Creighton J A 1977 Anomalously intense Raman spectra of pyridine at a silver electrode *Journal of the American Chemical Society* **99** 5215–7
- [65] Ritchie R H 1957 Plasma Losses by Fast Electrons in Thin Films *Phys. Rev.* **106** 874–81

- [66] Stiles P L, Dieringer J A, Shah N C and Van Duyne R P 2008 Surface-Enhanced Raman Spectroscopy *Annual Review of Analytical Chemistry* **1** 601–26
- [67] Willets K A and Van Duyne R P 2007 Localized Surface Plasmon Resonance Spectroscopy and Sensing *Annual Review of Physical Chemistry* **58** 267–97
- [68] Mayer K M and Hafner J H 2011 Localized Surface Plasmon Resonance Sensors *Chemical Reviews* **111** 3828–57
- [69] Schlücker S 2014 Surface-Enhanced Raman Spectroscopy: Concepts and Chemical Applications *Angewandte Chemie International Edition* **53** 4756–95
- [70] Eustis S and El-Sayed M A 2006 Why gold nanoparticles are more precious than pretty gold: Noble metal surface plasmon resonance and its enhancement of the radiative and nonradiative properties of nanocrystals of different shapes *Chem. Soc. Rev.* **35** 209–17
- [71] Huang W, Jiang J-Z, Chen L, Zhang B-Q, Deng S-F, Sun J J and Chen W-K 2015 Density functional theory and surface enhanced Raman spectroscopy studies of tautomeric hypoxanthine and its adsorption behaviors in electrochemical processes *Electrochimica Acta* **164** 132–8
- [72] Freeman R G, Grabar K C, Allison K J, Bright R M, Davis J A, Guthrie A P, Hommer M B, Jackson M A, Smith P C, Walter D G and Natan M J 1995 Self-Assembled Metal Colloid Monolayers: An Approach to SERS Substrates *Science* **267** 1629–32
- [73] Brazhe N A, Parshina E Y, Khabatova V V, Semenova A A, Brazhe A R, Yusipovich A I, Sarycheva A S, Churin A A, Goodilin E A, Maksimov G V and Sosnovtseva O V 2013 Tuning SERS for living erythrocytes: Focus on nanoparticle size and plasmon resonance position: Tuning SERS for living erythrocytes *Journal of Raman Spectroscopy* **44** 686–94
- [74] Aroca R 2006 *Surface-Enhanced Vibrational Spectroscopy* (John Wiley & Sons)
- [75] Horvath H 2009 Gustav Mie and the scattering and absorption of light by particles: Historic developments and basics *Journal of Quantitative Spectroscopy and Radiative Transfer* **110** 787–99
- [76] Kneipp K, Kneipp H and Bohr H G 2006 Single-Molecule SERS Spectroscopy *Surface-Enhanced Raman Scattering: Physics and Applications* Topics in Applied Physics ed K Kneipp, M Moskovits and H Kneipp (Berlin, Heidelberg: Springer Berlin Heidelberg) pp 261–77
- [77] Moskovits M 1982 Surface selection rules *J. Chem. Phys.* **77** 4408–16
- [78] Koh A L, Bao K, Khan I, Smith W E, Kothleitner G, Nordlander P, Maier S A and McComb D W 2009 Electron Energy-Loss Spectroscopy (EELS) of Surface Plasmons in Single Silver Nanoparticles and Dimers: Influence of Beam Damage and Mapping of Dark Modes *ACS Nano* **3** 3015–22

- [79] Leopold N and Lendl B 2003 A New Method for Fast Preparation of Highly Surface-Enhanced Raman Scattering (SERS) Active Silver Colloids at Room Temperature by Reduction of Silver Nitrate with Hydroxylamine Hydrochloride *The Journal of Physical Chemistry B* **107** 5723–7
- [80] Amendola V and Meneghetti M 2009 Laser ablation synthesis in solution and size manipulation of noble metal nanoparticles *Phys Chem Chem Phys* **11** 3805–21
- [81] Amendola V and Meneghetti M 2013 What controls the composition and the structure of nanomaterials generated by laser ablation in liquid solution? *Phys. Chem. Chem. Phys.* **15** 3027–46
- [82] Neddersen J, Chumanov G and Cotton T M 1993 Laser Ablation of Metals: A New Method for Preparing SERS Active Colloids *Appl. Spectrosc., AS* **47** 1959–64
- [83] Tolaymat T M, El Badawy A M, Genaidy A, Scheckel K G, Luxton T P and Suidan M 2010 An evidence-based environmental perspective of manufactured silver nanoparticle in syntheses and applications: A systematic review and critical appraisal of peer-reviewed scientific papers *Science of The Total Environment* **408** 999–1006
- [84] Tejamaya M, Römer I, Merrifield R C and Lead J R 2012 Stability of Citrate, PVP, and PEG Coated Silver Nanoparticles in Ecotoxicology Media *Environmental Science & Technology* **46** 7011–7
- [85] Alvarez-Puebla R A and Liz-Marzán L M 2010 SERS-Based Diagnosis and Biodetection *Small* **6** 604–10
- [86] Jaworska A, Fornasaro S, Sergio V and Bonifacio A 2016 Potential of Surface Enhanced Raman Spectroscopy (SERS) in Therapeutic Drug Monitoring (TDM). A Critical Review *Biosensors* **6** 47
- [87] Gutés A, Carraro C and Maboudian R 2010 Silver Dendrites from Galvanic Displacement on Commercial Aluminum Foil As an Effective SERS Substrate *Journal of the American Chemical Society* **132** 1476–7
- [88] Luo S-C, Sivashanmugan K, Liao J-D, Yao C-K and Peng H-C 2014 Nanofabricated SERS-active substrates for single-molecule to virus detection in vitro: A review *Biosensors and Bioelectronics* **61** 232–40
- [89] Polavarapu L and Liz-Marzán L M 2013 Towards low-cost flexible substrates for nanoplasmonic sensing *Physical Chemistry Chemical Physics* **15** 5288
- [90] Gurian E, Bellich B and Cesàro A 2016 Polysaccharide solutions and gels: Isothermal dehydration study by dynamic calorimetric experiments with DSC *Food Hydrocolloids* **61** 163–71
- [91] Yu W W and White I M 2013 Inkjet-printed paper-based SERS dipsticks and swabs for trace chemical detection *Analyst* **138** 1020–5

- [92] Hasi W-L-J, Lin X, Lou X-T, Lin S, Yang F, Lin D-Y and Lu Z-W 2015 Chloride ion-assisted self-assembly of silver nanoparticles on filter paper as SERS substrate *Appl. Phys. A* **118** 799–807
- [93] Camposeo A, Spadaro D, Magrì D, Moffa M, Gucciardi P G, Persano L, Maragò O M and Pisignano D 2016 Surface-enhanced Raman spectroscopy in 3D electrospun nanofiber mats coated with gold nanorods *Analytical and Bioanalytical Chemistry* **408** 1357–64
- [94] He Y Q, Liu S P, Kong L and Liu Z F 2005 A study on the sizes and concentrations of gold nanoparticles by spectra of absorption, resonance Rayleigh scattering and resonance non-linear scattering *Spectrochimica Acta Part A: Molecular and Biomolecular Spectroscopy* **61** 2861–6
- [95] Zhang Y, Lai X, Zeng Q, Li L, Lin L, Li S, Liu Z, Su C, Minni Qi and Guo Z 2018 Classifying low-grade and high-grade bladder cancer using label-free serum surface-enhanced Raman spectroscopy and support vector machine *Laser Phys.* **28** 035603
- [96] Park M, Kang B-H and Jeong K-H 2018 Paper-Based Biochip Assays and Recent Developments: A Review *BioChip Journal* **12** 1–10
- [97] Anon Global Cancer Observatory
- [98] Wang Y, Yan B and Chen L 2013 SERS Tags: Novel Optical Nanoprobes for Bioanalysis *Chemical Reviews* **113** 1391–428
- [99] Liu R, Xiong Y, Guo Y, Si M and Tang W 2018 Label-free and non-invasive BS-SERS detection of liver cancer based on the solid device of silver nanofilm *Journal of Raman Spectroscopy* **49** 1426–34
- [100] Dasary S S R, Singh A K, Senapati D, Yu H and Ray P C 2009 Gold Nanoparticle Based Label-Free SERS Probe for Ultrasensitive and Selective Detection of Trinitrotoluene *Journal of the American Chemical Society* **131** 13806–12
- [101] Kumar N, Bansal A, Sarma G S and Rawal R K 2014 Chemometrics tools used in analytical chemistry: An overview *Talanta* **123** 186–99
- [102] Beleites C, Neugebauer U, Bocklitz T, Krafft C and Popp J 2013 Sample size planning for classification models *Anal. Chim. Acta* **760** 25–33
- [103] Otto M 2016 *Chemometrics: Statistics and Computer Application in Analytical Chemistry* (Weinheim, Germany: Wiley-VCH Verlag GmbH & Co. KGaA)
- [104] Brereton R G 2003 *Chemometrics* (Chichester, UK: John Wiley & Sons, Ltd)
- [105] Dubinin M M 1960 The Potential Theory of Adsorption of Gases and Vapors for Adsorbents with Energetically Nonuniform Surfaces. *Chem. Rev.* **60** 235–41
- [106] Foo K Y and Hameed B H 2010 Insights into the modeling of adsorption isotherm systems *Chemical Engineering Journal* **156** 2–10

- [107] Liu S 2015 Cooperative adsorption on solid surfaces *Journal of Colloid and Interface Science* **450** 224–38
- [108] Ringot D, Lerzy B, Chaplain K, Bonhoure J-P, Auclair E and Larondelle Y 2007 In vitro biosorption of ochratoxin A on the yeast industry by-products: comparison of isotherm models *Bioresour. Technol.* **98** 1812–21
- [109] Gesztelyi R, Zsuga J, Kemeny-Beke A, Varga B, Juhasz B and Tosaki A 2012 The Hill equation and the origin of quantitative pharmacology *Arch. Hist. Exact Sci.* **66** 427–38
- [110] Pucetaite M, Velicka M, Pilipavicius J, Beganskiene A, Ceponkus J and Sablinskas V 2016 Uric acid detection by means of SERS spectroscopy on dried Ag colloidal drops: Uric acid detection by means of SERS spectroscopy *Journal of Raman Spectroscopy* **47** 681–6
- [111] Lee P C and Meisel D 1982 Adsorption and surface-enhanced Raman of dyes on silver and gold sols *The Journal of Physical Chemistry* **86** 3391–5
- [112] Pillai Z S and Kamat P V 2004 What Factors Control the Size and Shape of Silver Nanoparticles in the Citrate Ion Reduction Method? *J. Phys. Chem. B* **108** 945–51
- [113] Ngo Y H, Li D, Simon G P and Garnier G 2012 Gold Nanoparticle–Paper as a Three-Dimensional Surface Enhanced Raman Scattering Substrate *Langmuir* **28** 8782–90
- [114] Drescher D, Büchner T, McNaughton D and Kneipp J 2013 SERS reveals the specific interaction of silver and gold nanoparticles with hemoglobin and red blood cell components *Physical Chemistry Chemical Physics* **15** 5364
- [115] Premasiri W R, Lee J C and Ziegler L D 2012 Surface Enhanced Raman Scattering of Whole Human Blood, Blood Plasma and Red Blood Cells: Cellular Processes and Bioanalytical Sensing *J Phys Chem B* **116** 9376–86
- [116] Abe M, Kitagawa T and Kyogoku Y 1978 Resonance Raman spectra of octaethylporphyrinato-Ni(II) and *m e s o*-deuterated and ¹⁵N substituted derivatives. II. A normal coordinate analysis *The Journal of Chemical Physics* **69** 4526–34
- [117] Rusciano G, De Luca A C, Pesce G and Sasso A 2008 Raman Tweezers as a Diagnostic Tool of Hemoglobin-Related Blood Disorders *Sensors (Basel)* **8** 7818–32
- [118] Spiro T G and Czernuszewicz R S 1995 Resonance Raman spectroscopy of metalloproteins *Meth. Enzymol.* **246** 416–60
- [119] Genova E, Pelin M, Decorti G, Stocco G, Sergio V, Ventura A and Bonifacio A 2018 SERS of cells: What can we learn from cell lysates? *Analytica Chimica Acta* **1005** 93–100

- [120] Brazhe N A, Abdali S, Brazhe A R, Luneva O G, Bryzgalova N Y, Parshina E Y, Sosnovtseva O V and Maksimov G V 2009 New insight into erythrocyte through in vivo surface-enhanced Raman spectroscopy *Biophys. J.* **97** 3206–14
- [121] R Core Team 2018 *R: A Language and Environment for Statistical Computing* (Vienna, Austria)
- [122] Beleites C and Sergo V 2018 *hyperSpec: a package to handle hyperspectral data sets in R*
- [123] Hovde Liland K and Mevik B-H 2015 *baseline: Baseline Correction of Spectra*
- [124] Gibb S and Strimmer K 2012 MALDIquant: a versatile R package for the analysis of mass spectrometry data *Bioinformatics* **28** 2270–1
- [125] Brazhe N A, Abdali S, Brazhe A R, Luneva O G, Bryzgalova N Y, Parshina E Y, Sosnovtseva O V and Maksimov G V 2009 New Insight into Erythrocyte through In Vivo Surface-Enhanced Raman Spectroscopy *Biophysical Journal* **97** 3206–14
- [126] Casella M, Lucotti A, Tommasini M, Bedoni M, Forvi E, Gramatica F and Zerbi G 2011 Raman and SERS recognition of β -carotene and haemoglobin fingerprints in human whole blood *Spectrochim Acta A Mol Biomol Spectrosc* **79** 915–9
- [127] Wood B R, Caspers P, Puppels G J, Pandiancherri S and McNaughton D 2007 Resonance Raman spectroscopy of red blood cells using near-infrared laser excitation *Anal Bioanal Chem* **387** 1691–703
- [128] Sánchez-Cortés S and García-Ramos J V 1998 Anomalous Raman bands appearing in surface-enhanced Raman spectra *Journal of Raman Spectroscopy* **29** 365–71
- [129] Premasiri W R, Lee J C and Ziegler L D 2012 Surface-Enhanced Raman Scattering of Whole Human Blood, Blood Plasma, and Red Blood Cells: Cellular Processes and Bioanalytical Sensing *J. Phys. Chem. B* **116** 9376–86
- [130] Westley C, Xu Y, Thilaganathan B, Carnell A J, Turner N J and Goodacre R 2017 Absolute Quantification of Uric Acid in Human Urine Using Surface Enhanced Raman Scattering with the Standard Addition Method *Anal. Chem.* **89** 2472–7
- [131] Drescher D, Büchner T, McNaughton D and Kneipp J 2013 SERS reveals the specific interaction of silver and gold nanoparticles with hemoglobin and red blood cell components *Phys. Chem. Chem. Phys.* **15** 5364–73
- [132] Vilanova O, Mittag J J, Kelly P M, Milani S, Dawson K A, Rädler J O and Franzese G 2016 Understanding the Kinetics of Protein–Nanoparticle Corona Formation *ACS Nano* **10** 10842–50
- [133] Pino P del, Pelaz B, Zhang Q, Maffre P, Nienhaus G U and Parak W J 2014 Protein corona formation around nanoparticles – from the past to the future *Mater. Horiz.* **1** 301–13

- [134] McNay G, Eustace D, Smith W E, Faulds K and Graham D 2011 Surface-enhanced Raman scattering (SERS) and surface-enhanced resonance Raman scattering (SERRS): a review of applications *Appl Spectrosc* **65** 825–37
- [135] Anon Human Metabolome Database
- [136] Sing T, Sander O, Beerenwinkel N and Lengauer T 2005 *ROCR: visualizing classifier performance in R*
- [137] Chowdhury J, Mukherjee K M and Misra T N 2000 A pH dependent surface-enhanced Raman scattering study of hypoxanthine *Journal of Raman Spectroscopy* **31** 427–31
- [138] Huang W, Jiang J-Z, Chen L, Zhang B-Q, Deng S-F, Sun J J and Chen W-K 2015 Density functional theory and surface enhanced Raman spectroscopy studies of tautomeric hypoxanthine and its adsorption behaviors in electrochemical processes *Electrochimica Acta* **164** 132–8
- [139] Westley C, Xu Y, Thilaganathan B, Carnell A J, Turner N J and Goodacre R 2017 Absolute Quantification of Uric Acid in Human Urine Using Surface Enhanced Raman Scattering with the Standard Addition Method *Anal. Chem.* **89** 2472–7
- [140] Giese B and McNaughton D 2002 Surface-Enhanced Raman Spectroscopic and Density Functional Theory Study of Adenine Adsorption to Silver Surfaces *J. Phys. Chem. B* **106** 101–12
- [141] Pagliai M, Caporali S, Muniz-Miranda M, Pratesi G and Schettino V 2012 SERS, XPS, and DFT Study of Adenine Adsorption on Silver and Gold Surfaces *The Journal of Physical Chemistry Letters* **3** 242–5
- [142] Goodall B L, Robinson A M and Brosseau C L 2013 Electrochemical-surface enhanced Raman spectroscopy (E-SERS) of uric acid: a potential rapid diagnostic method for early preeclampsia detection *Phys. Chem. Chem. Phys.* **15** 1382–8
- [143] Chowdhury J, Mukherjee K M and Misra T N 2000 A pH dependent surface-enhanced Raman scattering study of hypoxanthine *Journal of Raman Spectroscopy* **31** 427–31
- [144] Prieto F, Alvarez-Malmagro J and Rueda M 2017 Electrochemical Impedance Spectroscopy study of the adsorption of adenine on Au(111) electrodes as a function of the pH *Journal of Electroanalytical Chemistry* **793** 209–17
- [145] Tavagnacco L, Fonzo S D, D'Amico F, Masciovecchio C, Brady J W and Cesàro A 2016 Stacking of purines in water: the role of dipolar interactions in caffeine *Phys. Chem. Chem. Phys.* **18** 13478–86
- [146] Tavagnacco L, Schnupf U, Mason P E, Saboungi M-L, Cesàro A and Brady J W 2011 Molecular Dynamics Simulation Studies of Caffeine Aggregation in Aqueous Solution *J Phys Chem B* **115** 10957–66

- [147] Pucetaite M, Velicka M, Pilipavicius J, Beganskiene A, Ceponkus J and Sablinskas V 2016 Uric acid detection by means of SERS spectroscopy on dried Ag colloidal drops: Uric acid detection by means of SERS spectroscopy *Journal of Raman Spectroscopy* **47** 681–6
- [148] Lin V J C and Koenig J L 1976 Raman studies of bovine serum albumin *Biopolymers* **15** 203–18
- [149] Hamidreza Arabi S, Aghelnejad B, Schwieger C, Meister A, Kerth A and Hinderberger D 2018 Serum albumin hydrogels in broad pH and temperature ranges: characterization of their self-assembled structures and nanoscopic and macroscopic properties *Biomaterials Science* **6** 478–92
- [150] Joseph M M, Narayanan N, Nair J B, Karunakaran V, Ramya A N, Sujai P T, Saranya G, Arya J S, Vijayan V M and Maiti K K 2018 Exploring the margins of SERS in practical domain: An emerging diagnostic modality for modern biomedical applications *Biomaterials* **181** 140–81
- [151] Stefancu A, Moisoiu V, Couti R, Andras I, Rahota R, Crisan D, Pavel I E, Socaciu C, Leopold N and Crisan N 2018 Combining SERS analysis of serum with PSA levels for improving the detection of prostate cancer *Nanomedicine* **13** 2455–67
- [152] Li S, Zhang Y, Xu J, Li L, Zeng Q, Lin L, Guo Z, Liu Z, Xiong H and Liu S 2014 Noninvasive prostate cancer screening based on serum surface-enhanced Raman spectroscopy and support vector machine *Applied Physics Letters* **105** 091104
- [153] Del Mistro G, Cervo S, Mansutti E, Spizzo R, Colombatti A, Belmonte P, Zucconelli R, Steffan A, Sergio V and Bonifacio A 2015 Surface-enhanced Raman spectroscopy of urine for prostate cancer detection: a preliminary study *Analytical and Bioanalytical Chemistry* **407** 3271–5
- [154] Wang J, Koo K M, Wee E J H, Wang Y and Trau M 2017 A nanoplasmonic label-free surface-enhanced Raman scattering strategy for non-invasive cancer genetic subtyping in patient samples *Nanoscale* **9** 3496–503
- [155] Park J, Hwang M, Choi B, Jeong H, Jung J-H, Kim H K, Hong S, Park J-H and Choi Y 2017 Exosome Classification by Pattern Analysis of Surface-Enhanced Raman Spectroscopy Data for Lung Cancer Diagnosis *Anal. Chem.* **89** 6695–701
- [156] Li X 2012 Spectral analysis of human saliva for detection of lung cancer using surface-enhanced Raman spectroscopy *Journal of Biomedical Optics* **17** 037003
- [157] Yang T, Guo X, Wu Y, Wang H, Fu S, Wen Y and Yang H 2014 Facile and Label-Free Detection of Lung Cancer Biomarker in Urine by Magnetically Assisted Surface-Enhanced Raman Scattering *ACS Applied Materials & Interfaces* **6** 20985–93
- [158] Lin D, Feng S, Pan J, Chen Y, Lin J, Chen G, Xie S, Zeng H and Chen R 2011 Colorectal cancer detection by gold nanoparticle based surface-enhanced Raman spectroscopy of blood serum and statistical analysis *Opt Express* **19** 13565–77

- [159] Lin D, Pan J, Huang H, Chen G, Qiu S, Shi H, Chen W, Yu Y, Feng S and Chen R 2015 Label-free blood plasma test based on surface-enhanced Raman scattering for tumor stages detection in nasopharyngeal cancer *Scientific Reports* **4**
- [160] Feng S, Chen R, Lin J, Pan J, Chen G, Li Y, Cheng M, Huang Z, Chen J and Zeng H 2010 Nasopharyngeal cancer detection based on blood plasma surface-enhanced Raman spectroscopy and multivariate analysis *Biosensors and Bioelectronics* **25** 2414–9
- [161] Li S X, Zhang Y J, Zeng Q Y, Li L F, Guo Z Y, Liu Z M, Xiong H L and Liu S H 2014 Potential of cancer screening with serum surface-enhanced Raman spectroscopy and a support vector machine *Laser Phys. Lett.* **11** 065603
- [162] Huang S, Wang L, Chen W, Feng S, Lin J, Huang Z, Chen G, Li B and Chen R 2014 Potential of non-invasive esophagus cancer detection based on urine surface-enhanced Raman spectroscopy *Laser Physics Letters* **11** 115604
- [163] Feng S, Lin D, Lin J, Li B, Huang Z, Chen G, Zhang W, Wang L, Pan J, Chen R and Zeng H 2013 Blood plasma surface-enhanced Raman spectroscopy for non-invasive optical detection of cervical cancer *The Analyst* **138** 3967
- [164] Kah J C Y, Kho K W, Lee C G L, James C, Sheppard R, Shen Z X, Soo K C and Olivo M C 2007 Early diagnosis of oral cancer based on the surface plasmon resonance of gold nanoparticles *Int J Nanomedicine* **2** 785–98
- [165] Feng S, Chen R, Lin J, Pan J, Wu Y, Li Y, Chen J and Zeng H 2011 Gastric cancer detection based on blood plasma surface-enhanced Raman spectroscopy excited by polarized laser light *Biosensors and Bioelectronics* **26** 3167–74
- [166] Xiao R, Zhang X, Rong Z, Xiu B, Yang X, Wang C, Hao W, Zhang Q, Liu Z, Duan C, Zhao K, Guo X, Fan Y, Zhao Y, Johnson H, Huang Y, Feng X, Xu X, Zhang H and Wang S 2016 Non-invasive detection of hepatocellular carcinoma serum metabolic profile through surface-enhanced Raman spectroscopy *Nanomedicine* **12** 2475–84
- [167] Lu Y, Lin Y, Zheng Z, Tang X, Lin J, Liu X, Liu M, Chen G, Qiu S, Zhou T, Lin Y and Feng S 2018 Label free hepatitis B detection based on serum derivative surface enhanced Raman spectroscopy combined with multivariate analysis *Biomed. Opt. Express, BOE* **9** 4755–66
- [168] Guo J, Rong Z, Li Y, Wang S, Zhang W and Xiao R 2018 Diagnosis of chronic kidney diseases based on surface-enhanced Raman spectroscopy and multivariate analysis *Laser Phys.* **28** 075603
- [169] Tien N, Chen H-C, Gau S-L, Lin T-H, Lin H-S, You B-J, Tsai P-C, Chen I-R, Tsai M-F, Wang I-K, Chen C-J and Chang C-T 2016 Diagnosis of bacterial pathogens in the dialysate of peritoneal dialysis patients with peritonitis using surface-enhanced Raman spectroscopy *Clinica Chimica Acta* **461** 69–75
- [170] Kamińska A, Witkowska E, Kowalska A, Skoczyńska A, Gawryszewska I, Guziewicz E, Snigurenko D and Waluk J 2016 Highly efficient SERS-based

detection of cerebrospinal fluid neopterin as a diagnostic marker of bacterial infection *Analytical and Bioanalytical Chemistry* **408** 4319–27

- [171] Chae E-J, Lee J-H, Oh B-K and Choi J-W 2013 Label-free nanobiosensor to detect infectious bacteria based on SERS *Journal of Biomedical Nanotechnology* **9** 659–63
- [172] Boardman A K, Wong W S, Premasiri W R, Ziegler L D, Lee J C, Miljkovic M, Klapperich C M, Sharon A and Sauer-Budge A F 2016 Rapid detection of bacteria from blood with surface-enhanced Raman spectroscopy *Analytical Chemistry* **88** 8026–35
- [173] Key T J, Verkasalo P K and Banks E 2001 Epidemiology of breast cancer *Lancet Oncol.* **2** 133–40
- [174] Parkin D M, Bray F I and Devesa S S 2001 Cancer burden in the year 2000. The global picture *Eur. J. Cancer* **37 Suppl 8** S4-66
- [175] Allemani C, Minicozzi P, Berrino F, Bastiaannet E, Gavin A, Galceran J, Ameijide A, Siesling S, Mangone L, Ardanaz E, Hédelin G, Mateos A, Micheli A, Sant M and the EUROCARE Working Group 2013 Predictions of survival up to 10 years after diagnosis for European women with breast cancer in 2000-2002 *International Journal of Cancer* **132** 2404–12
- [176] Guida 2017 I numeri del cancro in Italia 2017. *I numeri del cancro in Italia 2017.* 245
- [177] Autier P, Boniol M, LaVecchia C, Vatten L, Gavin A, Héry C and Heanue M 2010 Disparities in breast cancer mortality trends between 30 European countries: retrospective trend analysis of WHO mortality database *BMJ* **341** c3620
- [178] Le M T, Mothersill C E, Seymour C B and McNeill F E Is the false-positive rate in mammography in North America too high? *Br J Radiol* **89**
- [179] Bleyer A and Welch H G 2012 Effect of Three Decades of Screening Mammography on Breast-Cancer Incidence *New England Journal of Medicine* **367** 1998–2005
- [180] Reddy J K and Rao M S 2006 Lipid metabolism and liver inflammation. II. Fatty liver disease and fatty acid oxidation *Am. J. Physiol. Gastrointest. Liver Physiol.* **290** G852-858
- [181] Yasutake K, Nakamuta M, Shima Y, Ohyama A, Masuda K, Haruta N, Fujino T, Aoyagi Y, Fukuizumi K, Yoshimoto T, Takemoto R, Miyahara T, Harada N, Hayata F, Nakashima M and Enjoji M 2009 Nutritional investigation of non-obese patients with non-alcoholic fatty liver disease: the significance of dietary cholesterol *Scand. J. Gastroenterol.* **44** 471–7
- [182] Angulo P 2002 Nonalcoholic Fatty Liver Disease *New England Journal of Medicine* **346** 1221–31

- [183] Barbero-Becerra V J, Rosso N, Chavez-Tapia N C and Tiribelli C 2012 T-51 NAFLD to NASH: an experimental study on the early events of fibrosis *Digestive and Liver Disease* **44** S31
- [184] Chavez-Tapia N C, Rosso N and Tiribelli C 2012 Effect of intracellular lipid accumulation in a new model of non-alcoholic fatty liver disease *BMC Gastroenterol* **12** 20
- [185] Clark J M, Brancati F L and Diehl A M 2002 Nonalcoholic fatty liver disease *Gastroenterology* **122** 1649–57
- [186] Dam-Larsen S, Franzmann M, Andersen I B, Christoffersen P, Jensen L B, Sørensen T I A, Becker U and Bendtsen F 2004 Long term prognosis of fatty liver: risk of chronic liver disease and death *Gut* **53** 750–5
- [187] Matteoni C A, Younossi Z M, Gramlich T, Boparai N, Liu Y C and McCullough A J 1999 Nonalcoholic fatty liver disease: a spectrum of clinical and pathological severity *Gastroenterology* **116** 1413–9
- [188] Rockey D C, Caldwell S H, Goodman Z D, Nelson R C, Smith A D and American Association for the Study of Liver Diseases 2009 Liver biopsy *Hepatology* **49** 1017–44
- [189] Buzzetti E, Pinzani M and Tsochatzis E A 2016 The multiple-hit pathogenesis of non-alcoholic fatty liver disease (NAFLD) *Metabolism* **65** 1038–48
- [190] Pinter M, Trauner M, Peck-Radosavljevic M and Sieghart W 2016 Cancer and liver cirrhosis: implications on prognosis and management *ESMO Open* **1** e000042
- [191] Mazzaferro V, Regalia E, Doci R, Andreola S, Pulvirenti A, Bozzetti F, Montalto F, Ammatuna M, Morabito A and Gennari L 1996 Liver transplantation for the treatment of small hepatocellular carcinomas in patients with cirrhosis *N. Engl. J. Med.* **334** 693–9
- [192] Mazzanti R, Arena U and Tassi R 2016 Hepatocellular carcinoma: Where are we? *World J Exp Med* **6** 21–36
- [193] European Association for the Study of the Liver. Electronic address: easloffice@easloffice.eu and European Association for the Study of the Liver 2018 EASL Clinical Practice Guidelines: Management of hepatocellular carcinoma *J. Hepatol.* **69** 182–236
- [194] Sanyal A J, Yoon S K and Lencioni R 2010 The etiology of hepatocellular carcinoma and consequences for treatment *Oncologist* **15** Suppl 4 14–22
- [195] Xie J, Zhang A and Wang X 2017 Metabolomic applications in hepatocellular carcinoma: toward the exploration of therapeutics and diagnosis through small molecules *RSC Adv.* **7** 17217–26

- [196] Soga T, Sugimoto M, Honma M, Mori M, Igarashi K, Kashikura K, Ikeda S, Hirayama A, Yamamoto T, Yoshida H, Otsuka M, Tsuji S, Yatomi Y, Sakuragawa T, Watanabe H, Nihei K, Saito T, Kawata S, Suzuki H, Tomita M and Suematsu M 2011 Serum metabolomics reveals γ -glutamyl dipeptides as biomarkers for discrimination among different forms of liver disease *J. Hepatol.* **55** 896–905
- [197] Cervo S, De Paoli P, Perin T, Canzonieri V and Steffan A 2015 Cost-Effective Organization of an Institutional Human Cancer Biobank in a Clinical Setting: CRO-Biobank Experience Toward Harmonization *The International Journal of Biological Markers* **30** 243–51
- [198] Cervo S, Mansutti E, Del Mistro G, Spizzo R, Colombatti A, Steffan A, Sergo V and Bonifacio A 2015 SERS analysis of serum for detection of early and locally advanced breast cancer *Anal Bioanal Chem* **407** 7503–9
- [199] Alberts D S and Hess L M 2008 *Fundamentals of cancer prevention* (Berlin; [London: Springer-Verlag)
- [200] Sirota J C, McFann K, Targher G, Johnson R J, Chonchol M and Jalal D I 2013 Elevated serum uric acid levels are associated with non-alcoholic fatty liver disease independently of metabolic syndrome features in the United States: Liver ultrasound data from the National Health and Nutrition Examination Survey *Metab. Clin. Exp.* **62** 392–9
- [201] Li Y, Xu C, Yu C, Xu L and Miao M 2009 Association of serum uric acid level with non-alcoholic fatty liver disease: A cross-sectional study *Journal of Hepatology* **50** 1029–34
- [202] Lawton K A, Berger A, Mitchell M, Milgram K E, Evans A M, Guo L, Hanson R W, Kalhan S C, Ryals J A and Milburn M V 2008 Analysis of the adult human plasma metabolome *Pharmacogenomics* **9** 383–97
- [203] Liu R, Xiong Y, Guo Y, Si M and Tang W 2018 Label-free and non-invasive BS-SERS detection of liver cancer based on the solid device of silver nanofilm *Journal of Raman Spectroscopy* **49** 1426–34